Prétraitement optimal des images radar et modélisation des dérives de nappes d'hydrocarbures pour l'aide à la photo-interprétation en exploration pétrolière et surveillance environnementale

Zhour Najoui

UNIVERSITÉ PARIS-EST

THESE DE DOCTORAT

Ecole Doctorale : MSTIC

par

Zhour NAJOUI

pour obtenir le grade de

Docteur de l'Université Paris Est

Spécialité: Sciences et technologies de l'Information Géographique

Directeur de la thèse : **Benoît Deffontaines**

Sujet de la thèse :

Prétraitement optimal des images radar et modélisation des dérives de nappes d'hydrocarbures pour l'aide à la photo-interprétation en exploration pétrolière et surveillance environnementale

Soutenu publiquement le 30 /06/2017 devant la commission d'examen composée de :

Benoît Deffontaines	HDR	Université Paris Est	Directeur de Thèse
Damien Dhont	Ingénieur	Total	Examinateur
Eric Monjoux	Ingénieur	ESA	Invité
Jean Chorowicz	Thèse d'Etat	Université Paris 6/UPMC	Examinateur
Jean-Marie Nicolas	HDR	ENST	Rapporteur
Jean-Paul Xavier	HDR	Université UPPA Pau	Invité
Mina Amharref	HDR	Université Abdelmalek Saadi Tanger-Maroc	Rapporteur
Serge Riazanoff	PAST	Université Paris Est	Examinateur

Ce travail de thèse a été réalisé dans le cadre d'un contrat CIFRE en collaboration avec :

L'université Paris-Est (UPE)

5 Bd Descartes

77454 Marne-la-Vallée, Cedex 2

France

&

Le Laboratoire de REcherches en Géodésie (LAREG)

Service de la Recherche IGN

73 avenue de Paris

94160 Saint Mandé

France

&

La société VisioTerra

14 rue Albert Einstein

77420 Champs-sur-Marne

France

Résumé

Ce travail de thèse traite de l'optimisation des analyses et des prétraitements des images radar pour la détection des nappes d'huile en domaine océanique (communément appelés "*oil slicks*" en anglais) ainsi que la localisation des sources de suintements d'huiles d'origine naturelle ("*oil seeps*") sur le plancher océanique. Moyens, méthodes et difficultés des divers traitements y sont exposés. Cette thèse se compose des trois axes de recherche distincts expliqués et détaillés ci-dessous :

1. Une approche stochastique pour le prétraitement et l'amélioration des images radar en bande C afin de détecter automatiquement les nappes d'huile.

2. Une approche stochastique utilisant une grande quantité d'images radar pour évaluer l'influence de la vitesse du vent et les différents modes de l'instrument (SAR) pour l'optimisation de la détection des nappes d'hydrocarbures.

3. La localisation précise de la source des émissions d'hydrocarbures marins à l'aide d'un nouveau modèle de dérive verticale, appliqué au Golfe du Mexique (USA).

En premier, nous nous sommes intéressés à l'optimisation des prétraitements et l'amélioration des images radar en bande C par des méthodes stochastiques. Le but est de proposer une nouvelle méthodologie pour la détection automatique des nappes d'huile en domaine océanique à partir d'images radar. La méthodologie proposée comprend trois niveaux de traitement: prétraitement, seuillage et nettoyage binaire. Le premier niveau s'attèle à corriger l'hétérogénéité de la luminosité dans les images radar due à la réflexion non lambertienne du signal radar sur la surface de la mer. Le deuxième niveau consiste en une étape de seuillage qui vise à produire des objets noirs aussi proches que possible de l'ensemble de données d'apprentissage manuellement élaborées. Le troisième niveau, quant à lui, vise à nettoyer les images binaires de sortie des résidus de bruit. Plusieurs méthodes de prétraitement et de nettoyage ont été testées et évaluées par un moteur de qualification qui compare les objets détectés automatiquement avec les zones des objets noirs détectées manuellement. En conséquence, la « meilleure » méthode de prétraitement qui homogénéise la luminosité des scènes radar en bande C et optimise la détection automatique des huiles repose sur une adaptation au modèle de rétrodiffusion en bande C (CMOD5). En ce qui concerne le processus de nettoyage, les méthodes morphologiques testées montrent qu'une ouverture par zone ("*Small Object Removal*", SOR) suivie d'une fermeture morphologique optimise la détection automatique des nappes d'huile marines.

Par la suite, nous nous sommes penchés sur l'évaluation de l'influence de la vitesse du vent et des modes de l'instrument sur la détection des nappes d'hydrocarbures sur les images radar en utilisant une approche stochastique ; c.à.d. en utilisant un très grand nombre de données pour qualifier nos modèles.

Cette étude a été dictée par le besoin de définir les conditions météorologiques à même de permettre une détection optimale des nappes d'huiles, à partir des images radar. En effet, l'opération de la détection des nappes avec ce moyen est considérablement entravée par les conditions environnementales. L'un des facteurs les plus déterminants est, sans conteste, la vitesse du vent, à laquelle la moitié de cette partie se consacre. L'objectif a été de déterminer l'intervalle de vitesse du vent qui optimise la détection des nappes d'huiles dans toutes les images radar utilisant du BigData et une approche stochastique. Les études précédentes ont donné des gammes de vitesses de vent pour la détectabilité des nappes d'huile par des approches empiriques. De manière plus systématique, nous nous basons sur une approche stochastique en impliquant un ensemble de 1333 images et un échantillon de presque 4000 nappes d'huiles de différentes natures et origines. Ces nappes ont été systématiquement analysées de manière exhaustive. Suite à ces analyses l'intervalle optimal pour la détectabilité des nappes d'huile en surface de la mer de toutes sortes d'huiles a été arrêté entre les valeurs 2,09 et 8,33 m/s. Le résultat innovant est la haute corrélation linéaire (r=+0,953) mesurée dans cet intervalle entre la détectabilité des nappes et la vitesse du vent.

Ce travail a également été une occasion de nous intéresser aux propriétés des modes d'acquisition radar employés dans la détection des nappes d'huile. Ainsi, un ordre de performance de 5 modes est établi (IW, APP, PRI, IMP et WSM) et montre que le mode IW (Sentinel-1), avec la meilleure résolution spatiale (supérieure à 5x20m), est le plus approprié pour détecter une nappe d'huile à forte vitesse du vent.

Enfin, nous nous sommes focalisés sur l'estimation de la localisation des sources de pétrole naturel marin à l'aide d'un nouveau modèle de dérive verticale. Ainsi, nous avons élaboré une nouvelle méthode de détection des sources des suintements d'huile d'origine naturelle sur le plancher océanique selon le modèle de la dérive verticale. Les manifestations de suintements d'hydrocarbures sur la surface de la mer sont généralement décalées de leur source sur les fonds marins de plusieurs centaines de mètres ou même de kilomètres. Ce décalage est fonction de la vitesse ascensionnelle et des courants marins le long de la colonne d'eau. Cette vitesse ascensionnelle dépend pour une grande part de la taille du diamètre des gouttes d'huile. Dans cette étude, le diamètre des gouttelettes ne nous est pas connu à priori. Pour combler ce manque d'information, on a appliqué une nouvelle méthode appelée « chemin des sources » qui calcule la position des sources de suintement sur le plancher en fonction de différents diamètres de gouttelettes et du modèle vertical le long de la colonne d'eau jusqu'à leur point d'éclosion en surface.

Si ces trois études peuvent êtres prises chacune indépendamment des autres, elles sont fortement interconnectées et complémentaires. Elles forment une sorte de séquence de traitements (tube) allant de l'optimisation de la détection d'une nappe (les moyens et les outils les plus adéquats pour une meilleure détection) jusqu'à la localisation de sa source sur le plancher océanique.

Abstract

This thesis deals with the preprocessing of radar images and their optimization for the analyzes in order to detect natural marine oil slicks (Sea surface Outbreak/SSO) as well as better determine their source location at the Sea Floor Source (SFS). We explained herein means, methods and difficulties encountered. This thesis consists of the following three distinct research axes represented by three submitted papers :

1- A stochastic approach for pre-processing and improvement of C-band radar images to automatically detect oil slicks;

2- A stochastic approach using a large quantity of radar images to evaluate the influence of wind speed and the different modes of the instrument (SAR) on the delectability of marine oil slicks ;

3- Accurate location of the Sea Floor Source of marine hydrocarbon emissions using a new vertical drift model within the water column, applied to the northern Gulf of Mexico (southern USA).

So first, we focused on the optimization of pre-processing and the improvement of C-band radar images by stochastic methods to automatically detect oil slicks. The aim is to propose a new methodology for the pretreatment and improvement of radar images for the automatic detection of oceanic oil slicks. The proposed methodology includes three processing levels : preprocessing, thresholding, and binary cleaning. The first level consists of correcting the heterogeneity of the luminosity in the radar images resulting from the non-Lambertian reflection of the radar signal on the sea surface. The second level consists of a thresholding step which aims to produce dark objects as close as possible to the manually developed training data set. The third level consists of cleaning the output binary images from the noise residuals. Several preprocessing and cleaning methods have been tested and evaluated by a qualification engine that compares the objects automatically detected with the manual detection. As a result, the "best" pre-processing method that homogenizes the brightness of C-band radar scenes and optimizes automatic oil detection is based on an adaptation to the C-band backscatter model (CMOD5). With regard to the cleaning process, the morphological methods tested show that the Small Objects Removal (SOR) followed by a morphological closing optimizes the automatic detection of marine oil slicks.

Then, we focus in a second chapter in the evaluation of the influence of wind speed and instrument modes on the detection of oil slicks from radar images by using a stochastic approach, i.e. by using a huge number of samples to qualify our models. This study was dictated by the need to define the meteorological conditions capable for an optimal detection of oil slicks, from the radar images. Indeed, the detection of the oil slicks with this means is considerably hampered by the environmental

conditions. One of the most decisive factors is, unquestionably, the wind speed, to which this part is devoted. The objective was to determine the wind speed range which optimizes the detection of oil slicks in all radar images using BigData and a stochastic approach. Previous studies have already given ranges of wind speeds for the detection of oil slicks but they proceeded by empirical approaches. In contrast herein, we rely on a stochastic approach as we studied a set of 1333 images and a sample of almost 4000 oil slicks (of different natures and origins) that were analyzed, which gives as results a completeness character. Following these analyzes, the optimum range for the detectability of the oceanic surface slicks of all kinds of oils are now defined herein precisely in between the values of 2.09 and 8.33 m/s. The innovative result is the high linear correlation (r=+0.953) between the slicks detectability and the wind speed measured in this range.

This work was also an opportunity to investigate the properties of the radar acquisition modes used in the detection of oil slicks. Thus, the performances of the five acquisition modes (IW, APP, PRI, IMP and WSM) have been assessed showing that the IW (Sentinel-1) mode, with the best spatial resolution (greater than 5x20m) detects oil slicks at high wind speed.

Finally, we focused on estimating the location of marine natural oil seeps sources using a new vertical drift model, applied in the Gulf of Mexico. Thus, we have developed a new method for detecting the source of oil seeps from natural sources on the seafloor according to the vertical drift model. Occurrences of oil seeps on the sea surface are generally offset from their sources on the seabed by several hundred meters or even kilometers. This deflection is dependent on the upward velocity of the oil and marine currents along the water column. This upward velocity strongly depends on the oil droplet diameter. In this study, the diameter of the droplets is not known to us a priori. To fill this gap, a new method called the "sources path" was applied herein that calculate the location of the Sea Floor Source taking into account the droplet size and the vertical drift within the water column before their Sea surface Outbreak (SSO).

If these three studies can be taken independently of each other, they are firmly interconnected and complementary. These three parts are sequentially set along a processing sequence (pipe) going from the optimization of the detection of an oil slick (the most appropriate means and tools for better detection) to the location of its source on the seafloor.

Table des Matières

Introduction

Les indices d'huile affleurant à la surface des mers, de par leur l'intérêt, ont fait l'objet de nombreuses études et publications scientifiques (Gade et Alpers, 1998; Espedal, 1999; Gade et Alpers, 1999; Fiscella et al.,2000; Frate et al., 2000; Gade et Viebahn, 2000; Gasull et al., 2002; Fortuny-Guasch, 2003; Kanaa et al., 2003; Alpers et al., 2004; Jackson et Alpers, 2004; Brekke et Solberg, 2005; Angiuli et al., 2006; Chang et al., 2008; Garcia-Pineda et al., 2008; Garcia-Pineda et al., 2009; Frate et al., 2013; Fingas et Brown, 2014; Bayramov et al., 2015). Quelles que soient leurs origines et leurs caractéristiques, elles peuvent représenter aussi bien un danger pour les écosystèmes marins qu'une source de précieuses informations au service de l'activité pétrolière. Leur intérêt est, de ce fait, double tant sur le plan environnemental qu'économique.

Prenons-en pour exemple les pollutions causées par les navires (déballastage improprement appelés « dégazage ») et/ou les plates-formes pétrolières (incidents/accidents) qui justifient amplement l'intérêt environnemental. En effet, selon un rapport publié par le Groupe mixte d'Experts sur les Aspects Scientifiques de la Protection de l'environnement Marin (GESAMP, 2007), le rejet annuel moyen mondial de pétrole de toutes les sources connues dans la mer a été estimé à 1,2452 Million de tonnes par an. Ces grandes quantités de polluants ont un impact très négatif sur les écosystèmes marins, les pêches et la faune sauvage. De ce fait, les progrès dans la détection, localisation, caractérisation, quantification, et évolution des indices d'huile à la surface des étendues d'eau deviennent un préalable pour toute action visant la sauvegarde des écosystèmes marins.

L'intérêt économique –pétrolier– est important puisque dans les mers et les océans nous puisons une grande partie des hydrocarbures nécessaires à la production d'énergie de notre civilisation. En fait, l'offshore a fourni près de 70% des principales découvertes de pétrole et de gaz dans le monde au cours de la dernière décennie (Sandrea et Sandrea, 2010), ce qui est considérable. Et les nappes d'huile d'origine naturelle parvenant à la surface de la mer, en raison de toutes les informations qui peuvent en être tirées, jouent un rôle majeur dans l'exploration et la production de pétrole.

Que les nappes soient d'origine naturelle ou anthropique, l'un des meilleurs outils servant à leur détection reste l'imagerie radar. En effet, cette technique a plusieurs avantages évoqués ci-dessous : 1) sa capacité à couvrir de larges surfaces, 2) son indépendance quant aux conditions météorologiques (tous temps, nuages, brouillard, précipitations...), ainsi que 3) son indépendance à l'illumination solaire (images jour/nuit). De ce fait, elle fournit un outil puissant, efficace, et opérationnel pour la détection des nappes de pétrole en surface de la mer (Jackson et Apel, 2004). Le premier satellite à avoir été utilisé pour la surveillance des nappes d'huile est le satellite SEASAT de la NASA, qui a été lancé en 1978. Dans les années 1990, une deuxième génération de capteurs RSO (Radar à Synthèse

d'Ouverture) a été lancée à bord des satellites tels que ALMAZ, ERS-1 (European Remote-Sensing Satellite), ERS-2, JERS (Japan Earth Resources Satellite), RADARSAT-1 et plus tard, Envisat, ALOS (Advanced Land Observation Satellite), RADARSAT-2, Cosmo-SkyMed et TerraSAR-X. Aujourd'hui, avec le lancement de Sentinel-1, les images radar sont devenues un outil essentiel pour la détection et la surveillance des nappes d'huile en surface de la mer. Sentinel-1 fonctionne avec la bande C (5,405 GHz) pour fournir des images RSO de résolution spatiale moyenne (distance d'échantillonnage au sol des produits IW à 10 mètres). Sa large fauchée (240 km en mode IW) offre une couverture mondiale rapide. Le Cosmo-SkyMed et TerraSAR-X fonctionnent avec la bande X et fournissent des images à haute résolution. RADARSAT-2 et Sentinel-1A fonctionnent tous les deux avec la bande C. Leurs successeurs, respectivement RCM (RADARSAT Constellation Mission) et Sentinel-1B augmenteront la capacité de revisite des deux programmes. Ces capteurs sont caractérisés par des bandes spectrales et des résolutions spatiales différentes et fonctionnent dans différentes polarisations.

Les nappes d'huiles sont visibles sur les images radar grâce à l'effet d' « amortissement » que l'huile produit sur les ondes capillaires et les petites ondes de gravité appelées vagues de Bragg. En effet, le signal radar rétrodiffusé de la surface de la mer est essentiellement contrôlé par les ondes de Bragg (Jackson et Apel, 2004; Mercier et Girard-Ardhuin, 2006; Shu et al., 2010; Xu et al., 2015). Une nappe d'huile réduit le signal radar rétrodiffusé parce que l'huile a une tension superficielle plus élevée que l'eau, induisant un amortissement des ondes capillaires de surface et résultant en une surface plus lisse qu'une «surface de mer sans huile» (Mercier et Girard-Ardhuin, 2006). En conséquence, les nappes de pétrole apparaissent sous la forme de «taches sombres» avec une rétrodiffusion faible dans les images radar alors que la surface marine non polluée environnante reste relativement brillante en raison de la rétrodiffusion élevée (Alpers et Huhnerfuss). En plus des nappes d'huile, de nombreux phénomènes océaniques produisent une faible rétrodiffusion et apparaissent également comme des objets sombres dans les images radar. Les objets sombres non pétroliers sont appelés « sosies de nappes d'huile » (communément appelés « *oil slicks lookalikes* » en anglais) et regroupent les régions de faibles vents, upwelling, trombes de pluie, ondes internes, courants…

Le double enjeu environnemental et économique étant évident, la détection des nappes d'huile à partir d'images radar engendre des difficultés techniques et opérationnelles pas toujours faciles à surmonter. En effet, la capacité d'un capteur radar à détecter les nappes marines dépend de plusieurs paramètres. C'est une interaction multivariée complexe qui fait intervenir les caractéristiques de l'instrument (longueur d'onde, polarisation, résolution spatiale…), les conditions d'acquisition (angles d'incidence, fauchée, mode d'acquisition…), le contexte environnemental (types de cibles, état de la mer, rugosité, conditions météorologiques…) et les propriétés des nappes d'huile (origine, épaisseur, âge…).

Comment, avec quels moyens et sous quelles conditions, pouvons-nous parvenir à une meilleure détection des nappes d'huile situées à la surface de la mer ? Peut-on faire en sorte pour que les images

radar soient plus faciles à être photo-interprétées soit manuellement soit traitées automatiquement pour une reconnaissance automatique des nappes d'huile ? Dans le cas où les nappes détectées sont d'origine naturelle, comment connaître précisément la localisation de leurs sources sur le plancher marin ? Ce sont, entre autres, les questions auxquelles cette thèse, composée de trois parties distinctes, et complémentaires, va tenter de répondre.

Ce travail se focalise, en effet, non seulement sur la détection (moyens optimaux ainsi que les difficultés s'y rattachant) des nappes d'huile, mais propose également des méthodes pour un meilleur prétraitement des images radar ainsi que d'autres techniques pour détecter la localisation des sources sur le plancher marin des suintements naturels de pétrole, quand l'origine n'est bien évidemment pas anthropique. C'est ce processus, allant de la détection des nappes d'huiles à la localisation des sources sur le fond marin (quand les nappes sont d'origine naturelle), que ce document tente de clarifier et de rendre plus maitrisable.

Le premier chapitre de cette thèse retrace l'état de l'art en matière de détection des nappes d'huile à l'aide de l'imagerie radar. Il se compose des cinq sections suivantes: -principe d'acquisition radar, -les nappes d'huile vue par le radar, -leur typologie, -les éléments influençant leur détection, et -les méthodes existantes pour leur détection.

Le deuxième chapitre évoque le prétraitement des images radar.

Le flux élevé des données RSO et le besoin d'une très haute réactivité rendent nécessaire l'automatisation de certaines tâches, notamment le prétraitement et la segmentation des images, en vue notamment d'une détection automatique des nappes d'huiles. Généralement dans la littérature le prétraitement des images radar est limité au filtrage du speckle. Malheureusement, des hétérogénéités de luminosité subsistent dans les images radar après un tel prétraitement classique ce qui entrave la «robustesse» de la segmentation et des méthodes de classification, surtout lorsque l'on travaille sur de grandes surfaces à l'échelle régionale/nationale, voir continentale. Ces hétérogénéités sont observées sur les surfaces marines (offshore) car les produits images distribués par les agences spatiales sont corrigés de plusieurs effets (forme de l'antenne, angles d'incidence ou distance au nadir) calibrés sur les surfaces continentales (onshore). L'hétérogénéité de la luminosité de l'image radar observée sur les zones offshore peut être justifiée par trois raisons physiques : 1) Distance du nadir : lorsque la cible est proche du nadir, la rétrodiffusion est plus forte, ce qui produit une texture claire qui contraste avec une cible éloignée du nadir où la rétrodiffusion est faible, ce qui produit une texture plus foncée; 2) Interaction entre la direction du vent et celle du radar: lorsque la direction du vent et la "ligne de vue" (*sightline* ou *pulse axis*) du radar sont colinéaires, les vaguelettes de surface induites par le vent sont perpendiculaires au pulse radar ce qui crée des sortes de «micro-miroirs» alignés, alors que lorsque le vent est perpendiculaire à la direction du "pulse" radar, les vaguelettes sont sous-parallèles à la direction du pulse radar et la majorité du signal est renvoyée sous une forme spéculaire loin du radar;

3) Mode d'acquisition ScanSAR qui de par son mode imageur en une série de sous-bandes, présente des discontinuités radiométriques au niveau des jonctions entre les sous-bandes (Grandin, 2015).

Quelles sont les méthodes optimales pour le prétraitement et la segmentation des images radar et quelles sont les difficultés s'y rattachant ? C'est à ces questions majeures que le Chapitre 2 tente de répondre.

Le troisième chapitre vise, à travers une approche stochastique, à évaluer l'influence de la vitesse du vent et les modes de l'instrument radar pour la détection des nappes d'hydrocarbures.

La capacité d'un capteur radar à détecter les nappes d'huile en surface de la mer dépend de plusieurs paramètres : -conditions météorologiques, -propriétés du capteur, -propriétés de l'huile, -saisonnalité, -température de l'eau, -salinité, etc. Le Chapitre 3 de cette thèse se penche sur deux de ces paramètres, à savoir la vitesse du vent et les propriétés du capteur, qui influencent fortement la détectabilité des nappes d'huile à partir d'imagerie radar. A la différence des approches empiriques citées dans la littérature, la présente étude se base sur une approche stochastique en tirant profit du Big Data.

Enfin le dernier chapitre traite de la localisation précise des sources des nappes sur le plancher océanique. En s'appuyant sur un nouveau modèle de la "dérive verticale", elle se veut une présentation d'une méthode nouvelle permettant de localiser les points sources indépendamment des informations (pas forcément à la disposition de l'explorateur) de la taille des gouttelettes d'huile remontant des fonds marins vers la surface de la mer.

Enfin une discussion, conclusion et perspective permettront de faire le point sur l'avancement des travaux sur les thématiques techniques d'analyses et d'interprétation auxquelles nous avons été confrontés lors de ce travail.

Chapitre 1 Détection des nappes d'huile en utilisant l'imagerie radar: état de l'art

Résumé du chapitre

Le présent chapitre présente l'état de l'art de la détection des nappes d'huile en surface de la mer en utilisant les images radar à synthèse d'ouverture. Principe d'acquisition radar, les nappes d'huile vue par le radar, leur typologie, les éléments influençant leur détection, et les méthodes existantes pour leur détection y sont exposés.

Les nappes d'huile flottantes en surface de la mer sont visibles sur les images radar parce que l'huile supprime (ou réduit) la rugosité de la surface marine. Il en résulte ainsi un contraste entre la forte rétrodiffusion produite par les vagues de Bragg et la faible (voire nulle) rétrodiffusion provoquée par la surface marine lissée par l'huile. La notion de l'amortissement des vagues de Bragg en présence de l'huile est relative au vent. En effet, les vagues de Bragg sont produites par le vent. Sous des vitesses de vent fortes l'huile perd sa capacité à lisser la surface de la mer. Ainsi, la vitesse du vent est un facteur déterminant dans la détection des nappes d'huile à partir des images radar. En plus de la vitesse du vent, divers facteurs affectent la rétrodiffusion radar et peuvent compromettre la détection des nappes d'huile marines sur les images RSO. Parmi ces facteurs, on peut citer la longueur d'onde du radar, la polarisation radar, l'angle d'incidence du radar, les propriétés diélectriques et la nature de la nappe d'huile, l'interaction entre la direction du vent et le plan de l'onde radar incidente.

Les nappes d'huile présentes sur la surface de la mer peuvent être d'origine minérale naturelle ("*oil seeps*"), d'origine minérale anthropique ("*oil spills*") ou d'origine naturelle biogénique ("*biogenic oils*"). Mais, en plus des nappes d'huile quelques soient leurs origines, d'autres phénomènes présentent les mêmes signatures sombres sur les images radar. Les objets sombres non-huile sont appelés "sosies" et comprennent les upwellings, les ondes internes, les trombes de pluie, les abrivents, et les courants marins. Les méthodes existantes pour la détection des nappes d'huile et leur différenciation de leurs sosies sont de trois types: manuelles, semi-automatiques, et automatiques.

1.1 Principe d'acquisition radar

Le système radar est un système de télédétection actif, qui peut être embarqué sur une plate-forme spatiale ou aéroportée, il fonctionne en émettant périodiquement un faisceau de microondes dans un plan perpendiculaire à la trajectoire. Si l'antenne sert à la fois d'émetteur et de récepteur, alors le système est dit monostatique et l'énergie reçue est la composante rétrodiffusée par le sol. L'intérêt d'un tel système est qu'il n'est pas soumis aux conditions de luminosité et peut donc acquérir des images de jour comme de nuit. De plus, la gamme de fréquence des ondes utilisées n'est pas affectée par les conditions atmosphériques, telle que la couverture nuageuse. Le système peut donc acquérir des images dans n'importe quelles conditions et en continu, fut-il en zone tropicale, tant que la capacité de traitement et de stockage le permettent.

Les ondes centimétriques présentent une stabilité de phase suffisante pour que la surface imagée puisse être échantillonnée en fonction de la distance des points à l'antenne par corrélation entre les impulsions émises et les échos reçus. L'onde est alors qualifiée de "cohérente".

Cette cohérence rend possible les applications interférométriques, cependant elle est aussi responsable du phénomène de speckle, bruit qui rend difficile la lecture et l'interprétation des images.

Dans d'acquisition radar, l'image est acquise en deux dimensions dont la nature diffère: 1/ la dimension longitudinale (le long de la trajectoire du satellite) qui est créée par des impulsions successives et le déplacement du satellite. 2/ la dimension transversale (perpendiculaire à la trajectoire du satellite) qui correspond donc à une distance en temps, c'est dans cette direction que l'image est distordue.

La géométrie d'imagerie RSO est représentée par la Figure 1. Le radar envoie une impulsion d'énergie à la cible et mesure la force de l'écho retourné - appelé aussi rétrodiffusion -, créant ainsi une image 2D de la zone cible. Une série d'impulsions de fréquence micro-ondes est transmise vers la Terre dans une direction perpendiculaire à la trajectoire au sol de la plate-forme. Les impulsions illuminent une empreinte elliptique sur la surface de la Terre en raison des propriétés directionnelles de l'antenne.

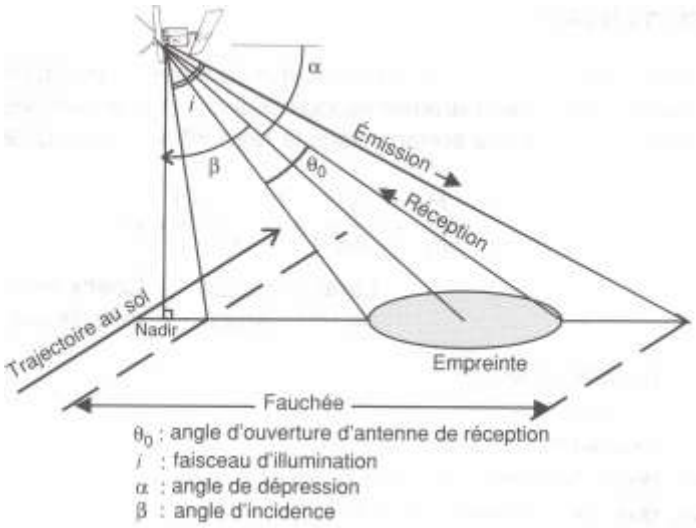

Figure 1. Schéma représentant le faisceau de balayage d'un satellite et les paramètres associés (Derrode, 2013).

1.2 Les nappes d'huile vues par les images RSO

Le RSO est le capteur satellite le plus efficace et le plus performant pour détecter les nappes d'hydrocarbures car il permet de travailler de jour comme de nuit, par temps de brouillard et même en présence de couverture nuageuse. L'intensité du signal radar dépend en grande partie de la rugosité de la surface imagée ainsi que des propriétés physiques de la cible (constante diélectrique) et les conditions d'acquisition de l'image radar. Une surface rugueuse et peu absorbante renverra un signal plus intense, par réflexion diffusive, alors qu'une surface lisse ne renverra pas de signal, car la réflexion est spéculaire dans ce cas.

Selon la théorie de Bragg, les vagues de Bragg sont responsables de la rétrodiffusion radar dans le milieu marin. En effet, les vagues de Bragg sont induites par le vent et ont des longueurs d'ondes spécifiques permettant la réflexion diffuse du signal radar. Dans de telles conditions le signal rétrodiffusé est très important car il s'agit d'une résonance. La taille de ces vagues ne permet pas de les imager individuellement, les régions où elles sont présentes montrent une luminosité constante s'il on fait abstraction des interactions possibles avec d'autres éléments.

Les nappes d'huile sont vues par le RSO comme des zones à faible rétrodiffusion. Ceci peut être justifié par le fait que les propriétés viscoélastiques des nappes de pétrole amortissent efficacement le domaine des ondes courtes (à l'échelle de Bragg) à la fois par la suppression de la croissance des vagues et l'augmentation de leur dissipation (Figure 2).

Il est important de connaître les propriétés géométriques et texturales des nappes d'huile afin d'éviter des confusions avec d'autres phénomènes qui provoquent les mêmes signatures que 'huile au niveau de

l'imagerie radar. La section suivante dresse une typologie quasi-exhaustive des nappes d'huile de leurs "sosies".

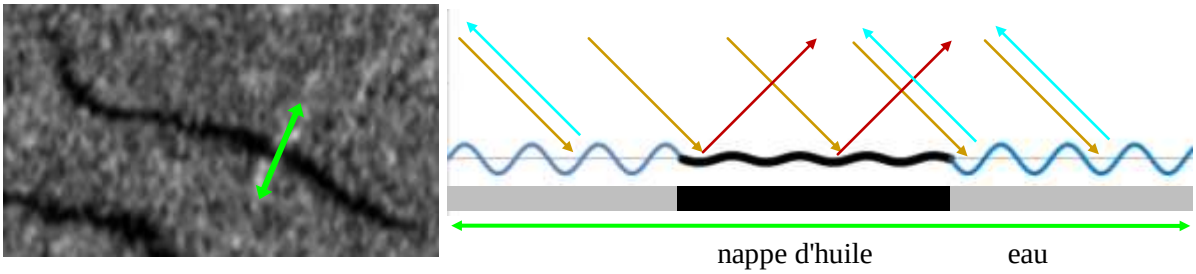

Figure 2. Rétrodiffusion du signal radar en présence et en absence de l'huile (section transversale, flèche verte). L'huile flottante sur la mer (signature noire sur l'image radar et lignes noires sur la section transversale) devient visible sur les images RSO car elle amortit les ondes de gravité capillaire courtes (ondes de Bragg en bleu). Cet effet d'amortissement provoque une rétrodiffusion spéculaire (flèches rouges) du signal radar incident (flèches jaunes) résultant ainsi en des taches sombres sur les images radar contrairement à la rétrodiffusion produite par les vagues de Bragg sans huile (flèche cyan).

1.3 Typologie des nappes d'huile et leurs sosies

Les nappes de pétrole sont visibles sur les images RSO en raison de l'effet amortisseur que le pétrole a sur les ondes de Bragg résultant en la réduction de la rétrodiffusion du signal micro-ondes radar, et donc provoquer des signatures noires. Malheureusement, les signatures noires peuvent également se produire dans les images radar en raison d'autres phénomènes météorologiques ou océanographiques. Les principaux objets sombres souvent observés à la surface de la mer à l'aide d'images RSO sont donnés par la Figure 3 et décrits ci-dessous.

Les nappes d'huile (*oil slicks*) sont divisées en deux grandes catégories: biogénique ou minéral. Les nappes d'huile biogènes sont produites par les planctons et les poissons. Les huiles minérales sont subdivisées en celles des suintements naturels (*oil seeps*) en provenance de réservoirs pétroliers sous-marins et celles des déversements d'hydrocarbures anthropiques provenant de navires, raffineries, terminaux pétroliers, installations industrielles, plates-formes pétrolières et pipelines (Espedal et Johannessen, 2000).

Les objets sombres non-huile (**sosies de nappes d'huile**, ***oil slicks lookalikes***) présents en surface de la mer sont principalement dus aux conditions météorologiques. Ils comprennent les upwellings, les ondes internes, les trombes de pluie, les abrivents, et les courants marins.

L'upwelling (*upwelling*) est le mouvement ascendant de l'eau des couches souterraines à la surface de la mer (Smith, 1968). Il se produit généralement près des côtes où l'influence du vent terrestre

repousse l'eau de surface de la mer. Ce mouvement ascendant apporte l'eau profonde, froide, riche en nutriments, faible en teneur en oxygène et dans la plupart des cas à faible salinité (Jackson et Apel, 2004). Sur l'imagerie radar, la baisse de température est habituellement suivie d'une réduction de la rugosité de la surface mer qui apparaît comme une tache sombre. De plus, l'apport en nutriments rend la surface de la mer un milieu riche et favorable pour la croissance des organismes (plancton et phytoplancton) et développe donc des films biogéniques qui apparaissent aussi comme une tache sombre sur les images radar.

Les ondes internes (*internal waves*) sont causées par une structure stratifiée de deux densités de fluides différents. Elles se produisent parce que l'eau profonde est froide, dense et salée, tandis que l'eau de surface est plus chaude, et plus légère et toute excitation ou perturbation de la pycnocline aura tendance à s'étaler au delà de la région de génération sous forme d'ondes (Apel, 1987). Par exemple, lorsque les marées traînent l'océan sur une barrière peu profonde telle qu'une crête sur le fond de l'océan, cela crée des vagues dans la couche d'eau plus basse et plus dense. Les ondes internes se propagent sous forme de paquets espacés de 10 km à 100 km (Jackson et Apel, 2004), chaque paquet se compose d'une succession de bandes foncées/claires de formes linéaires ou curvilignes. Ces signatures foncées et claires sont le résultat de variations de la rugosité de la surface de la mer (Alpers, 1985).

Les trombes de pluie (*rain cells*) se produisent quand il ya une forte pluie convective. Les gouttes de pluie qui frappent la surface de la mer engendrent des ondes annulaires qui augmentent la rugosité de la surface de la mer et apparaissent aussi brillantes sur les images RSO (Moore et al., 1979; Bliven et al., 1997; Craeye et al., 1997) et génèrent également des turbulences dans la couche supérieure de l'eau qui atténuent les ondes de Bragg et apparaissent sombres (Nystuen , 1990; Tsimplis, 1992). Les trombes de pluie ont généralement un diamètre entre 5 et 10 km, et peuvent se produire isolément ou en clusters (Jackson et Apel, 2004).

Les abrivents (*winds shadow*) provoqués par la topographie côtière ou les obstacles artificiels sont également couramment imagés par le RSO et ont une signature sombre. Ils se caractérisent par une surface lisse de la mer sans aucune vague due à l'absence/faible vent apparaissant ainsi comme des objets sombres.

Les courants marins (*currents*) sont généralement associés à la circulation de masses d'eau de différentes températures. Ils sont souvent accompagnés de changements de rugosité de la surface marine qui peuvent être associés à l'accumulation d'huiles biogéniques qui se produisent dans des régions de courants de surface convergents et apparaissent ainsi sombres (Ochadlick et al., 1992; Gower, 1994).

La discrimination entre les nappes d'hydrocarbures et leurs sosies est généralement basée sur plusieurs caractéristiques telles que la géométrie, la forme, la texture et d'autres informations contextuelles liées

à l'environnement. Le traitement et la caractérisation des sosies est important pour la détection automatique des nappes d'huile car ils aident à réduire les fausses alarmes.

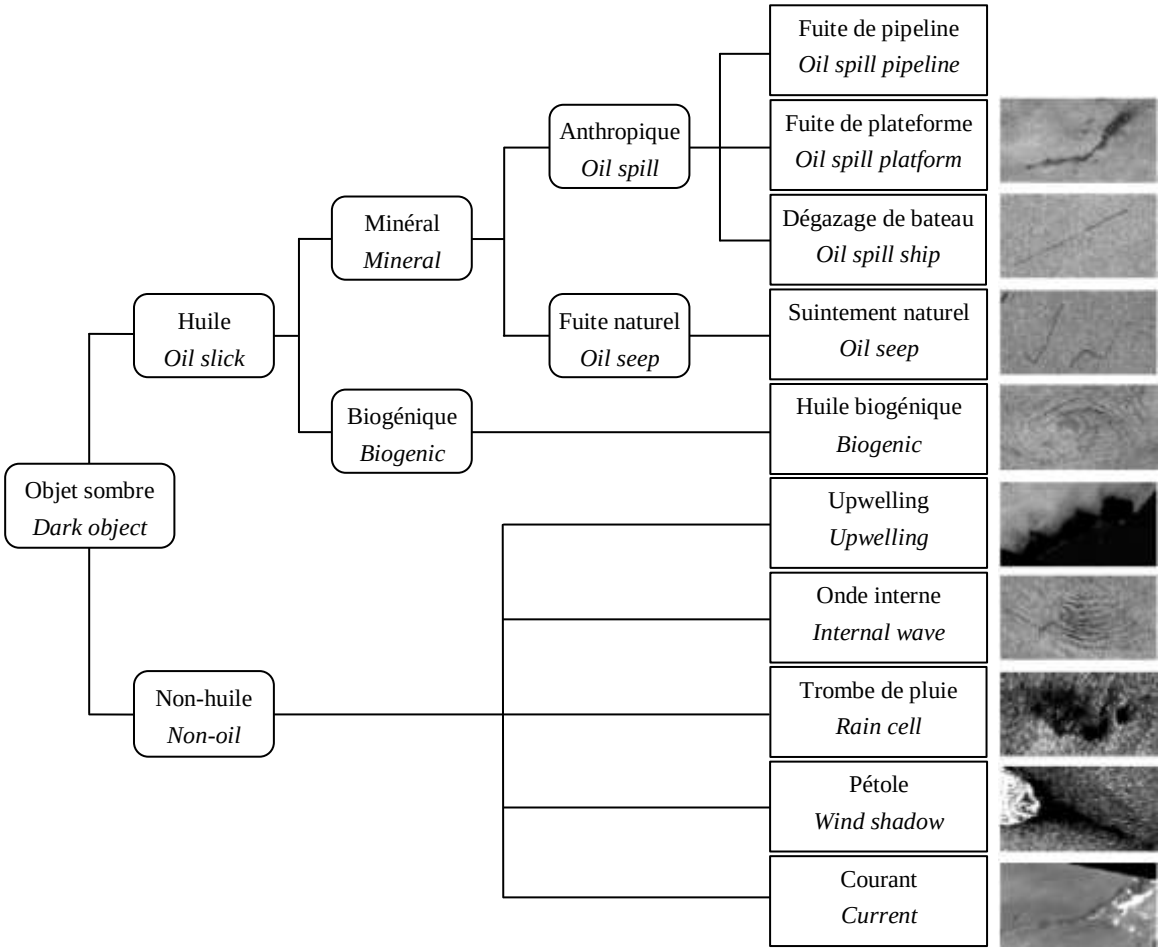

Figure 3. Les principaux objets sombres souvent observés à la surface de la mer en utilisant les images RSO.

1.4 Eléments influençant la détection des nappes d'huile

1.4.1 Effet de la vitesse du vent

Les nappes d'huile ne sont pas visibles sur les surfaces océaniques si le contraste entre la nappe et l'eau environnante n'est pas suffisamment élevé (par exemple à faible vitesse du vent). De plus, à des vitesses de vent élevées, les nappes d'huile ont tendance à se diviser en petits morceaux, ce qui empêche leur détection par les capteurs RSO (Garcia-Pineda, 2009). Diverses études ont été réalisées sur la plage de vitesse du vent qui optimise la détection des nappes d'huile sur les images RSO. La vitesse du vent requise pour la détection des nappes d'hydrocarbures a été estimée être de 3 à 7-10 m/s (Brekke et Solberg, 2005), de 3,5 à 7 m/s (Garcia-Pineda et al., 2009), de 1,5 à 10 m/s (Fingas et

Brown, 2014), et 1 à 7° m/s (Marghany, 2014a). Najoui et al. (2017 submitted) affirme, à partir d'une étude étendue basée sur une approche stochastique, que l'intervalle optimal pour la détection des nappes d'huile est entre 2,09 et 8,33 m/s où la détectabilité augmente avec l'augmentation de la vitesse du vent.

1.4.2 Effet de longueur d'onde radar

Selon la théorie de Bragg, l'effet d'amortissement des ondes de Bragg par l'huile est plus efficace à une longueur d'onde plus courte et par conséquent la bande X- (3-5 cm) et C (5-7 cm) sont plus efficaces pour détecter les nappes de pétrole que L- (19- 77 cm) et bande P (77-133 cm) (Jackson et Apel, 2004). Plusieurs études multifréquences ont révélé que la longueur d'onde de la bande C semble être la longueur d'onde la plus appropriée pour la détection des nappes d'hydrocarbures car elle permet le contraste maximum jusqu'à des vitesses de vent de 13 m/ (Girard-Ardhuin , 2003).

1.4.3 Effet de polarisation radar

De nombreuses études ont exploré le potentiel de la polarisation des capteurs pour la détection des nappes d'hydrocarbures (Elachi, 1988; Robinson, 1994; Fortuny-Guasch, 2003; Jackson et Apel, 2004; Najoui et al., 2017) et soulignent que la polarisation croisée (VH, HV) est considérablement moins efficace que la co-polarisation (VV, HH).

1.4.4 Effet de l'angle d'incidence radar

Les angles d'incidence entre 20 ° et 45 ° ont été considérés comme les angles d'incidence les plus appropriés pour la détection des nappes d'hydrocarbures (Espedal, 1999; De Beukelaer et al., 2003; Girard-Ardhuin et al., 2003; Pellon et al., 2004). La puissance du signal reçu par le radar dépend également de la distance entre le satellite et la cible (Johannessen et al., 2007). Lorsque la cible est proche du nadir, la rétrodiffusion est plus forte, ce qui contraste avec une cible éloignée du nadir, où la rétrodiffusion est plus faible.

1.4.5 L'effet des propriétés diélectriques et la nature des nappes d'huile

La détection des nappes d'huile sur les images RSO est également fonction des propriétés diélectriques et de la nature de la nappe: la conductivité électrique de l'eau de mer reste sensiblement supérieure à celle de l'huile dans l'eau (Charbonneau, 2006). Lorsqu'il ya une émulsion huile-dans-eau, cela augmente la conductivité électrique par rapport à l'huile pure (Jackson et Apel, 2004). Wismann (1993) rapporte que l'amortissement des vagues est plus important pour les nappes d'huile d'origine anthropique que pour les suintements d'huile naturelle dans les bandes C, X et Ku, alors que les suintements d'huile naturelle provoquent un amortissement plus fort avec la bande L à de faibles vitesses de vent (Wismann, 1993).

1.4.6 Interaction entre la direction du vent et la direction de l'onde radar incidente

Il a été observé que l'interaction entre la direction du vent et le plan de l'onde radar incidente affecte également la rétrodiffusion radar (Alpers et Huhnerfuss, 1988). Lorsque la direction du vent et le sens de la distance sont colinéaires (*upwind* ou *downwind*), les vagues du vent induites sont perpendiculaires à l'onde radar incidente ce qui renvoient une fraction importante du signal. Lorsque le vent est perpendiculaire à la direction du pulse radar, les ondes de surface de la mer sont parallèles à l'onde radar incidente et la majorité du signal est renvoyée sous une forme spéculaire loin du radar.

1.4.7 Large fauchée / mode ScanSAR

Pour obtenir une couverture étendue, plusieurs satellites sont construits avec ce qu'on appelle le mode ScanSAR (également appelé «mode rafale»). Ce mode consiste à commuter périodiquement l'antenne pointant dans plusieurs "sous-fauchées" (Moore et al., 1981; Currie et Brown, 1992). Sur les images radar acquises en mode ScanSAR, certains effets de luminosité peuvent apparaître entre les sous-fauchées. Ils sont causés par le gain d'antenne différent pour les sous-fauchées voisines. Ces problèmes de luminosité peuvent entraver la détection des nappes marines.

1.5 Algorithmes de la détection des nappes d'huile

Il ya eu de nombreuses études visant la détection des nappes d'hydrocarbures en utilisant des images RSO. D'un point de vue méthodologique, trois approches existent pour la détection des nappes d'huile dans les images RSO: **une approche manuelle** menée par des opérateurs humains formés qui analysent les images pour détecter les nappes d'hydrocarbures, **l'approche semi-automatique** où un ordinateur détecte tous les objets noirs dans l'image radar en utilisant différentes techniques de segmentation après quoi un opérateur humain expérimenté classifie ces objets comme nappes d'huile ou sosies, et enfin le **système automatique** qui utilise des techniques compliquées de traitement d'image et de programmation pour effectuer à la fois la segmentation et la classification.

Si nous n'avons pas trouvé d'exemples de détection manuelle dans la bibliographie, la segmentation et les classifications semi-automatiques et automatiques sont largement illustrées ci-dessous. Certaines techniques de segmentation utilisées sont le seuillage adaptatif (Solberg et al., 1999), le seuil d'hystérésis (Kanaa et al., 2003), la détection des arêtes à l'aide de Laplace de gaussiennes ou la différence de gaussiennes (Chang et al., 2008) , Les ondelettes (Liu et al., 1997) et la morphologie mathématique (Gasull et al., 2002). Les techniques de segmentation basées sur le réseau de neurones ont été démontrées dans Angiuli et al. (2006), Garcia-Pineda et al. (2009), et Del Frate et al. (2013). Certains algorithmes automatiques de détection des nappes d'huile sont des «classificateurs» utilisant une fonction de densité gaussienne basée sur une approche par modèle statistique (Solberg et al., 1999), un classificateur de Mahalanobis (Fiscella et al., 2000), des réseaux de neurones (Del Frate et

al, (Marghany, 2001), l'algorithme génétique (Marghany, 2014 et Marghany, 2015), l'algorithme d'évolution de l'entropie multi-objectifs (Marghany, 2014) et l'estimateur automatique d'emplacement des nappes d'huile naturelles (Suresh et al., 2015).

Chapitre 2 Prétraitement des images radar

Résumé du chapitre

Le but de cet article est de proposer une nouvelle méthodologie pour le prétraitement et l'amélioration des images radar en bande C (RSO) pour la détection automatique des nappes d'huile. La méthodologie proposée comprend trois niveaux de traitement: prétraitement, seuillage et nettoyage binaire. Le premier niveau consiste à corriger l'hétérogénéité de la luminosité dans les images causée par la réflexion non lambertienne du signal radar sur la surface de la mer. Cette hétérogénéité peut se justifier par: la distance par rapport au nadir (effet d'angle d'incidence), l'interaction entre la direction du vent et le signal radar incident, et le mode d'acquisition ScanSAR. Le deuxième niveau consiste en une étape de seuillage. Le troisième niveau consiste à nettoyer les images de sortie binaires des résidus de bruit. Plusieurs méthodes de prétraitement et de nettoyage ont été testées et évaluées par un moteur de qualification qui compare les objets sombres détectés automatiquement avec un jeu de données d'apprentissage détectés manuellement. L'ensemble d'apprentissage comprend les nappes d'huile et leurs sosies.

Il en est sorti de cette étude que la «meilleure» méthode de prétraitement qui homogénéise la luminosité des images radar en bande C et optimise la détection automatique des nappes d'huile repose sur une adaptation au modèle de rétrodiffusion en bande C (CMOD). En ce qui concerne le processus de nettoyage, les méthodes morphologiques testées montrent qu'une ouverture par zone suivi d'une fermeture morphologique optimise la détection automatique des nappes d'huile marines.

2.1 Introduction du chapitre

Les nappes d'huile représentent à la fois un enjeu environnemental et économique majeur. Le radar à synthèse d'ouverture, en raison de sa grande couverture et sa répétitivité, s'est avéré être un outil puissant pour leur détection. Cependant, le flux élevé de données RSO et le besoin d'une très haute réactivité rendent nécessaire l'automatisation de certaines tâches, notamment le prétraitement ainsi que le nettoyage des images, et ce en vue d'une segmentation automatique des nappes d'huile. Quelles en sont les méthodes optimales et les difficultés s'y rattachant ? C'est à cette question majeure que l'article qui fait l'objet du présent chapitre tente de répondre.

La détection des nappes d'huile marines comprend quatre étapes fondamentales: le prétraitement des images, la segmentation des objets sombres, l'extraction des caractéristiques et la classification (Solberg et al., 1999; Brekke and Solberg, 2005; Topouzelis and Konstantinos, 2008). Généralement dans la littérature, le prétraitement de l'image (première étape) est limité au filtrage du speckle. Malheureusement ce traitement seul ne permet pas de corriger tous les problèmes d'hétérogénéités dans les images radar. En raison 1/ des dépendances des angles d'incidence (les images radar ont tendance à devenir plus sombre quand on s'éloigne du nadir), 2/ les effets de la direction du vent par rapport au signal radar incident (*upwind/downwind* ou *crosswind*), et 3/ le mode d'acquisition ScanSAR, des variations de luminosité peuvent apparaître dans les images radar et donc compromettre leur traitement. Une variété de méthodes de segmentation ont été trouvées dans la littérature et sont énumérées ci-dessous: seuillage adaptatif (Solberg et al., 1999), seuil par hystérésis (Kanaa et al., 2003), détection des arêtes à l'aide de Laplace de Gaussiennes ou Différence de gaussiennes (Chang et al., 2008), ondelettes (Liu et al., 1997), morphologie mathématique (Gasull et al., 2002), le réseau de neurons (Garcia-Pineda et al., 2009; Angiuli et al., 2006; Del Frate et al.,2013), etc. Malgré la diversité des méthodes proposées, les plus fréquemment utilisées sont basées sur une analyse locale pour surmonter les problèmes dus aux variations de luminosité des images radar.

Le but de cette étude est de prétraiter les images radar afin de faciliter la détection manuelle, d'aider à la segmentation des objets sombres et de rendre plus fiable une reconnaissance automatique des nappes d'huile marines. Le traitement proposé dans cet article se compose de trois étapes principales: 1/ prétraitement capable de corriger les problèmes d'hétérogénéité de luminosité (dus aux conditions de vent et aux propriétés du capteur) résultant en une "image plate" qui diminue la complexité de la distribution de luminosité dans les images radar ; 2/ l'application d'un seuillage; Et 3/ nettoyage binaire pour éliminer le bruit résiduel dans l'image binaire obtenue après le seuillage. Pour sélectionner les meilleurs paramètres de prétraitement et d'amélioration optimisant la correction d'hétérogénéité radiométrique, le seuillage automatique et le nettoyage des images radar, un «moteur de qualification» a été réalisé. Le moteur de qualification utilise un ensemble d'apprentissage contenant 120 parcelles

d'entrainement détectées manuellement et une fonction de coût pour évaluer la distance entre le jeu de données d'apprentissage et le jeu de données traité automatiquement. La meilleure méthode est celle qui minimise la distance entre les deux ensembles de données.

2.2 Manuscrit 1: A statistical approach to preprocess and enhance C-Band SAR images in order to detect automatically marine oil slicks

Zhour Najoui [a,b], Serge Riazanoff [b,c], Benoit Deffontaines [a], Jean-Paul Xavier [b]

[a]Laboratoire de REcherche en Géodésie, LAREG, Université Paris-Est Marne-La-Vallée (UPEM), et Institut Géographique National, France, zhour.najoui@univ-paris-est.fr, benoit.deffontaines@univ-mlv.fr

[b]VisioTerra, Champs-sur-Marne, France, zhour.najoui@visioterra.fr, serge.riazanoff@visioterra.fr, jean-paul.xavier@visioterra.fr

[c]*Université Paris-Est Marne-La-Vallée UPEM - Institut Gaspard Monge, serge.riazanoff@univ-mlv.fr*

ABSTRACT

The aim of this paper is to propose a new methodology for preprocessing and enhancing C-band Synthetic Aperture Radar (SAR) images for the automatic detection of marine oil slicks. The proposed methodology includes three processing levels: preprocessing, thresholding, and binary cleaning. The first level is to correct the heterogeneity of brightness in SAR images caused by the non-Lambertian reflection of the radar signal on the sea surface. This heterogeneity can be justified by: - the distance from the nadir (incidence angle effect), - the interaction between wind direction and radar pulse, and - the width swath mode. The second level consists on a thresholding step. The third level is to clean the binary output images from noise residues. Several preprocessing and cleaning methods have been tested and evaluated by a qualification engine that compares the automatically detected patches with a training dataset of dark patches manually detected. The training dataset includes oil slicks and lookalikes. As a result, the "best" preprocessing method that homogenizes the brightness of C-band SAR scenes and optimizes the automatic detection of marine oil slicks is based on an adaptation to C-band backscattering model (CMOD). As for cleaning process, the tested morphological methods show that Small Object Removal (SOR) followed by a morphological closing optimizes the automatic detection of marine oil slicks.

Keywords

Preprocessing, SAR, Oil slick, CMOD, Local stretching, Segmentation, West Africa, Santa Barbara, Caspian Sea.

I. Introduction

Dealing with the terminology there are two major types of "marine oil slicks", -"mineral oil" and -"biogenic oil" (also known as surfactants) issued from biological process (Jackson and Apel, 2004; Jones et al., 2011). Mineral oil slicks on the sea surface have two main sources: -"oil spills" released from ships, oil platforms (rigs), pipelines, etc. (Espedal and Johannessen, 2000), and -"oil seepages" (also called natural or crude "oil seeps") naturally leaked from sea bottom petroleum reservoirs. Consequently, we call herein "oil slicks": -"oil spills" those which have anthropic origin and - "oil seeps" which have a natural origin (natural oil reservoir leaks), and - biogenic oil. Synthetic Aperture Radar (SAR) images have seen to be a powerful tool for oil slicks detection and monitoring. There are many technical and economical advantages to use radar images: -extended coverage (large swath, high repeatability regardless weather conditions or sun-light illuminations, dual missions, etc), -extensive data availability (increasing number of missions, emerging free data policy, archives of heritage data, large dissemination infrastructures, etc). Marine oil slicks represent both an environmental and economical concern. Opportune and accurate detection of oil slicks can help identification and management of polluted areas and assessment of oil slicks drift in order to protect the coasts. In addition to the environmental application, the detection of oil slicks and especially natural oil seeps is a good indicator to assess the presence and the maturity of an oil reservoir. Such oil seeps detection is therefore a major stake in oil exploration/production.

From the physical point of view, the sea surface backscattered radar signal is essentially controlled by the wind-induced capillary and small gravity waves, also called Bragg waves (Jackson and Apel, 2004; Mercier and Girard-Ardhuin, 2006; Shu et al., 2010; Xu et al., 2015). An oil slick reduces the backscattered radar signal because oil has higher surface tension than water, inducing dampening of the surface capillary waves, and resulting in a smoother sea surface than a "oil-free sea surface" (Mercier and Girard-Ardhuin, 2006; Hu et al., 2011). As a consequence, oil slicks appear as "dark patches" with weak backscattering in SAR images while the surrounding oil-free sea surface remains relatively bright due to the high backscattering (Alpers and Huhnerfuss, 1988). In addition to oil slicks, many ocean phenomena produce weak backscatter and appear also as dark patches in SAR images. Non-oil dark patches are termed "oil slick lookalikes" (Espedal, 1999; Brekke and Solberg, 2005; Xu and Brenning, 2014) and include weak wind regions (wind shadow), upwelling, rain cell, internal waves, current, etc. (see section A). The capability of a SAR sensor to detect marine oil slicks is a multivariate issue: it depends on the wind speed and direction, sensor properties (wavelength, polarization, incidence angle, swath width/ScanSAR, etc.), oil properties, etc. (see section II).

From the methodological point of view, the detection of marine oil slicks includes four basic steps: -images preprocessing, -dark patches segmentation, -features extraction and -oil slicks classification (Solberg et al., 1999; Brekke and Solberg, 2005; Topouzelis and Konstantinos, 2008). Generally in the literature, the image preprocessing (first step) is limited to speckle filtering on standard detected products. Unfortunately, so many heterogeneities remain in the radar images after such classical preprocessing hindering the "robustness" of the segmentation and the classification methods especially when working on large areas. The work of this paper focuses on image preprocessing and dark patches segmentation. Due to the incidence angle dependencies (SAR images tend to become darker with increasing range), upwind/downwind or crosswind, and swath width effects, brightness variations may occur in the SAR images and hence compromise the processing of SAR images. A variety of segmentation methods have been proposed and are listed below: adaptive thresholding (Solberg et al., 1999), hysteresis thresholding (Kanaa et al., 2003), edge detection using Laplace of Gaussians or Difference of Gaussians (Chang et al., 2008), wavelets (Liu et al., 1997), mathematical morphology (Gasull et al., 2002), neural network (Garcia-Pineda et al., 2009; Angiuli et al., 2006; Del Frate et al.,2013), etc., etc. Even though a variety of segmentation methods have been applied, the most frequently used are based on a local analysis to overcome the brightness variations in the SAR images.

The aim of this work is to preprocess SAR images in order to facilitate the manual detection, assist the segmentation of dark patches, and make more reliable further automatic recognition of marine oil slicks. The processing proposed in this paper consists of three main steps: 1) preprocessing able to correct the problems of brightness heterogeneity (due to wind conditions and sensor properties) resulting in a "flat image" that decreases the complexity of the brightness distribution in radar images; 2) applying a thresholding; and 3) binary cleaning to denoise the binary image obtained after thresholding. To select the best preprocessing and enhancing parameters optimizing the radiometric heterogeneity correction, the automatic thresholding and cleaning of the radar images, a "qualification engine" has been performed. The qualification engine uses a training dataset containing 120 training parcels manually detected and a cost function to assess the distance between the training dataset and the automatically processed dataset. The best preprocessing method minimize the distance between the two datasets.

In this paper, we first focus on the parameters that influence/jeopardize the oil slicks detection in SAR images (lookalikes, wind speed/direction, sensor properties, and oil properties). If the section 3 presents the SAR data used and the study areas, the section 4 provides a detailed description of the methodology that we settled and developed including in one hand, the training dataset manually detected, and in the other hand, the automatic processing which include the preprocessing methods (local stretching and adaptation to a backscattering model), the thresholding and the cleaning methods (small objects removal and morphological closing). Finally, the results are given in section 5.

II. Oil slicks detection on SAR images

Various factors affect the radar backscattering and may make challenged the detection of marine oil slicks on SAR images. These factors include oil slicks lookalikes, wind speed, radar wavelength, radar polarization, radar incidence angle, dielectric properties and the nature of oil slick, interaction between wind direction and the plane of the incident radar wave, and ScanSAR mode. These factors are presented below.

A. Oil slicks and lookalikes

Oil slicks are visible on SAR images because of the dampening effect that oil has on the gravity-capillary waves resulting in decreasing of the backscatter of the radar microwave radiation, and hence causing dark parches. Unfortunately, dark patches may also occur in radar images due to other meteorological or oceanographic phenomena. The main dark patches often observed at sea surface using SAR images are given by Figure 4 and described below.

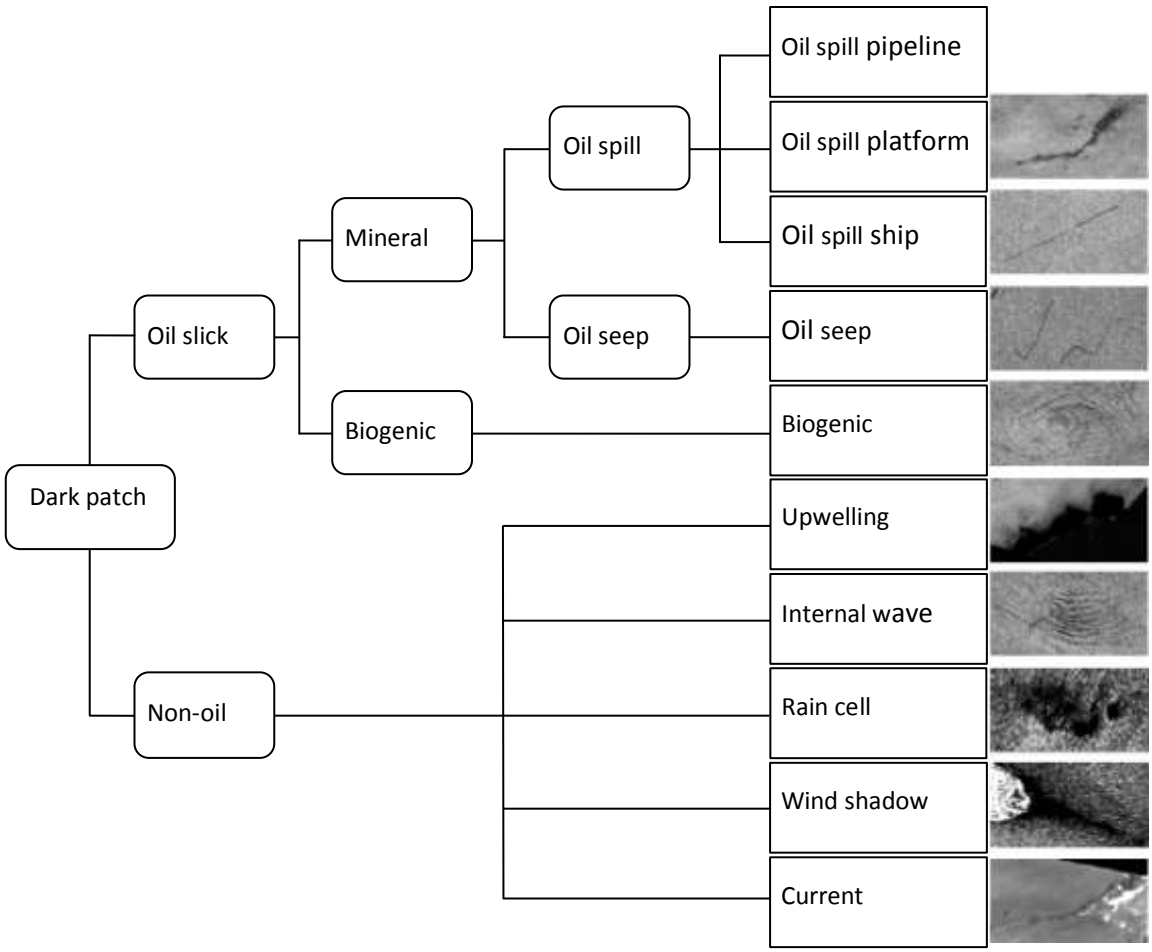

Figure 4. Main offshore dark patches seen in SAR images.

Oil slicks are divided into two major categories: biogenic or mineral. Biogenic oil slicks are produced by plankton and fish substances normally released into the environment. The mineral oils are subdivided into those of natural seeps from the sea bottom or anthropogenic oil spills that originate from ships, refineries, oil terminals, industrial plants, oil platforms, and pipelines (Espedal and Johannessen, 2000).

The mean **non-oil features** (oil slicks lookalikes) present on the sea surface are mostly due to meteorological conditions. They include upwelling, internal wave, rain cell, wind shadow, and sea currents.

Upwelling is the ascending motion of water from subsurface layers to the surface (Smith, 1968). It commonly occurs near coastlines where the influence of the onshore-wind pushes the sea surface water away. This upward movement brings deep, low temperature, high nutrients, low oxygen and in most cases low salinity water (Jackson and Apel, 2004). On radar imaging, the drop in temperature is usually followed by a reduction in sea roughness which appears as dark patch. Moreover, the nutrients intake "fertilize" and makes a favourable rich surface water content for the growth of organisms (plankton and phytoplankton) and therefore develop biogenic films that appear also as dark patch on radar images.

Internal waves are caused by a laminated structure of two different fluid densities. It happen because deep water is cold, dense, and salty, while shallower water is warmer, lighter, and fresher and any excitation or disturbance of the pycnocline will tend to spread out the generation region in the form of waves (Apel, 1987). For example, when tides drag the ocean over a shallow barrier such as a ridge on the ocean floor, it creates waves in the lower, denser layer of water. The internal waves propagate in the form of packets spaced 10 km to 100 km (Jackson and Apel, 2004), each packet consists on a succession of dark/white bands with a linear or curvilinear shapes. These dark and white signatures are the result of variations in sea surface roughness (Alpers, 1985).

Rain cells occur when there is high convective rain. Raindrops impinging on the sea surface generate ring waves which enhance the sea surface roughness appearing as bright on the SAR images (Moore et al., 1979; Bliven et al., 1997; Craeye et al., 1997) and also generate turbulence in the upper water layer which attenuates the Bragg waves and appear as dark (Nystuen, 1990; Tsimplis, 1992). Rain cells typically have diameter between 5 and 10 km, and can occur singly or in clusters (Jackson and Apel, 2004).

Wind shadowing by coastal topography or man-made obstacles is also commonly imaged by SAR and has dark signature. It is characterized by a smooth sea surface with no waves due to absence/weak wind appearing as dark patches.

Sea Currents are usually associated with water masses circulation of different temperature. They are often accompanied by changes in surface roughness which may be associated with the accumulation of

occurring biogenic oils in regions of converging surface currents which appear as dark (Ochadlick et al., 1992; Gower, 1994).

The discrimination between oil slicks and lookalikes is usually based on different characteristics such as geometry, shape, texture, and other contextual information related to the surroundings. The treatment and characterization of lookalikes is important for oil slicks automatic detection since it helps to reduce false alarms.

B. Wind speed effect

Oil slicks are not visible on the ocean surfaces if the contrast between the slick and the surrounding water is not sufficiently high (*e.g.* at low wind speeds). Moreover, at high wind speeds, the oil slicks tend to break up into smaller parts thus hindering detectability from SAR sensors (Garcia-Pineda et al., 2009). Wind speed requirement for oil slicks detection has been reported to be 2.09 to 8.33 m/s (Najoui et al., 2017 submitted) where the detectability increases with the increase of the wind speed.

C. Radar wavelength effect

According to Bragg theory, the dampening effect of Bragg waves is more efficient at shorter wavelength and hence X- (3-5 cm) and C-band (5-7 cm) are more efficient in detecting oil slicks than L- (19-77 cm) and P-band (77-133 cm) (Jackson and Apel, 2004). Several multifrequency studies revealed that C-band wavelength seems to be the most suitable wavelength for oil slicks detection as it allows the maximum contrast until wind speeds of 13 m/s (Girard-Ardhuin et al., 2003).

D. Radar polarization effect

Many studies discuss the potential of sensor polarization for oil slicks detection (Elachi, 1988; Robinson, 1994; Fortuny-Guasch, 2003; Jackson and Apel, 2004; Najoui et al., 2017) and they highlight that the cross- polarized (VH, HV) ocean backscattering is considerably less efficient than the co-polarized backscattering (VV, HH).

E. Radar incidence angle effect

Incidence angles between 20°- 45° was seen to be the most suitable incidence angles for oil slicks detection (Espedal, 1999; De Beukelaer et al., 2003; Girard-Ardhuin et al., 2003; Miranda, et al., 2004). The radar received signal strength also depends on the distance between the satellite and the target (slant range) (Johannessen et al., 2006). When the target is close to the nadir (near range),

backscatter is stronger which contrast with a far target from the nadir (far range), where backscatter is lower.

F. Dielectric properties and the nature of oil slick effect

The oil slick detection in SAR images is also a function of the dielectric properties and the nature of oil slick: the electrical conductivity of the sea water still substantially higher than oil-in-water (Charbonneau, 2006). When there is an oil-in-water emulsion, this increases the electrical conductivity compared to pure oil (Alpers & Espedal 2004). Wismann (1993) reports that wave damping is more important for oil spills than for natural oil seeps in the C-, X-, and Ku-bands, whereas natural oil seeps cause stronger damping with the L-band at low speed.

G. Interaction between wind direction and the plane of the incident radar wave effect

It has been observed that the interaction between wind direction and the plane of the incident radar wave also affects the radar backscattering (Alpers and Huhnerfuss, 1988). When wind direction and the range direction are collinear (upwind or downwind), the wind sea waves induced are perpendicular to the incident radar wave which return a much larger fraction of the signal. When the wind blowing is perpendicular to the range direction, the sea surface waves are sub-parallel to the incident radar wave and the majority of the signal is returned in a specular form away from the radar.

H. Swath width/ ScanSAR mode

To achieve a large coverage, various satellites are built with what is called ScanSAR mode (also called "burst mode" or "Wide Swath mode"). This mode consists of periodically switching the antenna pointing in several range “subswaths” (Moore et al., 1981; Currie and Brown, 1992). On the radar images acquired in ScanSAR mode some brightness effects may appear between subswaths. They are caused by different antenna gain for neighboring subswaths. These brightness problems may hinder the detection of marine oil slicks.

III. SAR dataset and areas of interest

In this study we used SAR images from Envisat ASAR (Advanced Synthetic Aperture Radar) in between 2002-2012. Envisat ASAR operates in C-Band (4.20 – 5.75 GHz) in a variety of modes including WSM (Wide Swath Medium-resolution). The WSM mode gives a 400 km by 400 km wide

swath image. Its spatial resolution is approximately 150 m by 150 m with pixel spacing of 75 m by 75 m. The spatial resolution is a measure of the system's ability to distinguish between adjacent targets. Pixel spacing is the distance between adjacent pixels in an image, measured in meters. ASAR WSM operates according to the ScanSAR principle, using five predetermined overlapping antenna beams which cover the wide swath (Figure 5).

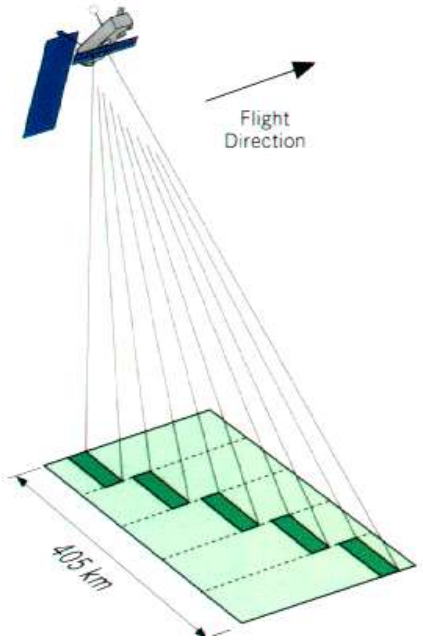

Figure 5. Mode ASAR Wide Swath using ScanSAR technique. The ScanSAR principle consist on achieving swath widening by the use of an antenna beam which is electronically steerable in elevation (European Space Agency, 2016).

For the purpose to be representative we apply the herein developed methodology to different study areas with different geographical, meteorological, and geological contexts (with regard to natural oil seeps). Three areas of interest (AOI) have been chosen: West Africa, Santa Barbara (Southern California), and the Caspian Sea (Figure 6). The 583 WSM scenes used in this study are kindly provided by the European Space Agency (ESA), in digital numbers (Table 1). All images have been georeferenced in the geographic coordinate reference system over the WGS84 ellipsoid, datum WGS84. An accurate land-sea mask has been applied. Thereafter, the images have been radiometrically corrected to ensure uniformity on offshore area by applying a linear stretching. After several tests, a local stretching with a mean of 140 and a standard deviation of 60 appeared the best choice to overcome the problem of brightness heterogeneity due to the distance from nadir (radar incidence angle). For manual detection, this preprocessing was quite sufficient (see example section IV-B-a).

Figure 6. Location maps of the study areas (AOI) from left to right: West Africa (Congo-Angola), Santa Barbara, and Caspian Sea. These three areas represent different geographical and meteorological contexts (Quadrangle and extracts from Google Earth).

Table 1 Number Envisat ASAR WSM scenes per AOI.

AOI	Number of WSM scenes
Congo/Angola	244 scenes
Caspian Sea	180 scenes
Santa Barbara	159 scenes

IV. Methodology

The optimization of the automatic detection of marine oil slicks on sea surface using SAR images requires appropriate preprocessing, thresholding, and cleaning methods. **Preprocessing methods should homogenize the brightness and contrast across the whole image. In order to do that homogenization, two methods have been tested (see section IV-B): the local stretching and the adaptation to a backscattering model (CMOD). The cleaning methods (see section IV-D) aim to denoise binary SAR images after preprocessing and thresholding. In this study, two morphological operators are used: Small Object Removal (SOR) and morphological closing.**

As given by Figure 7, to evaluate the proposed methods and choose the best processing, a training dataset (see section A) and a qualification engine have been performed. The training dataset is a set of 120 dark patches manually detected and comprises the main classes of dark patches often seen in SAR images (oil seep, oil spill fro m ship, oil spill from platform, biogenic oil, upwelling, internal wave, rain cell, and wind shadow). The qualification engine (see section IV-E) calls upon a cost function that calculates the minimal distance between the training dataset manually detected and the dataset

automatically processed, effectively the best method produces a binary image the closest possible to the manual detection. The chosen methods depend on some parameters, for example, local stretching requires the definition of a statistic window size, the SOR requires the definition of the connectivity, and the morphological closing requires the definition of a structuring element. The selection of the best parameter for each method is made using the qualification engine.

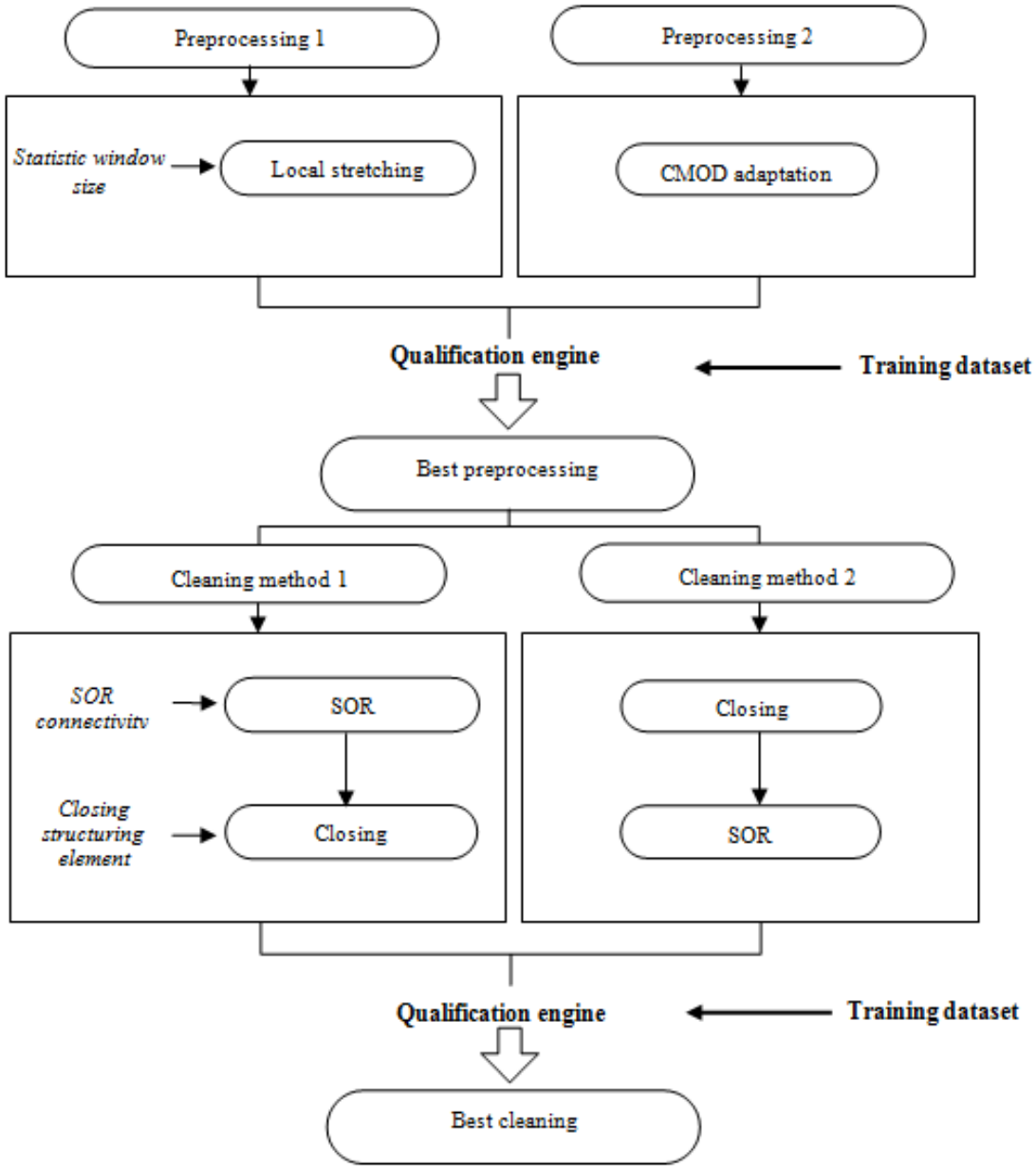

Figure 7. Methodological scheme. See text for explanations.

A. Training dataset

The training dataset has been performed from the manual detection over the three areas of interest. Only dark patches with a high confidence have been retained. The dataset comprises oil seep, oil spill

from ship, oil spill from platform, biogenic oil, upwelling, internal wave, rain cell, and wind shadow dark patches classes. The manual detection is based on the "Synthetic Aperture Radar marine user's manual" (NOAA, 2004). Each of the 583 SAR images has been manually interpreted independently from the others. Each dark patch has been categorized depending on the interpretation based on morphological and textural criteria. Thereafter, a multi-date analysis has been performed. We use all the interpretation at different dates in order to assess the manual interpretation. To perform and validate our analysis, the manual detection output has been integrated into a GIS with several data (geological data, marine traffic, oil platforms, oil and gas fields, wind fields, bathymetry, etc.). This work let to the constitution of a dataset of 120 dark patches defined with high confidence (Table 2).

Each of the eight dark patches classes is composed of one or more training parcels. An example of training parcel (oil seep) is given by Figure 8. The training parcels are as thumbnail images. The width and the height of the thumbnail images correspond respectively to 125% of the width and the height of the bounding box of the dark patches manually detected (Figure 8). The training parcels are land-masked.

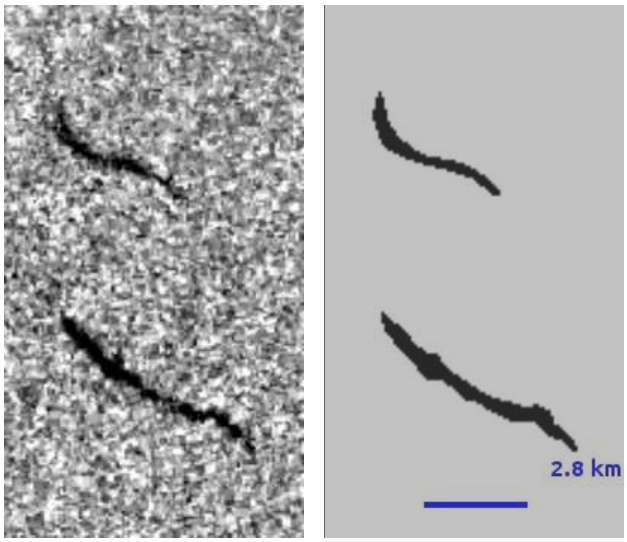

Figure 8. Example of a manual detection representing the SAR image of two oil seeps (left) and their manual detection (right).

Table 2 Number of training parcels per class.

classes	Oil seep	Spill ship	Spill platform	biogenic	Upwelling	Internal wave	Rain cell	Wind shadow
Number of parcels	20	20	20	12	12	12	12	12

B. Preprocessing methods

a. *Local stretching*

As explain previously, the signal received at the radar from a given pixel is a function of the distance from the nadir line (green arrow in Figure 9). The far range is darker, whereas, the near range is clearer. The local stretching of an image consists of defining a square neighborhood *S* (also called statistic window) and moving the center of this window from pixel to pixel. At each location *(i,j)*, the mean $\mu_{(i,j)}$ and the standard deviation $\sigma_{(i,j)}$ of the neighborhood $S_{(i,j)}$, are measured. The local values $\mu_{(i,j)}$ and $\sigma_{(i,j)}$ are used as the basis for making changes on the brightness and the contrast of the output image by imposing a new mean μ_0 and new standard deviation σ_0 given by the user. Based on so many empirical tests and previous experiments, a mean=140 and a standard deviation=60 appeared the best choice (Riazanoff and Gross, 2013). This transformation is given by the equation below:

$$r'_{(i,j)} = \frac{\sigma_0}{\sigma_{(i,j)}} \times r_{(i,j)} + \left[\mu_0 - \frac{\sigma_0}{\sigma_{(i,j)}} \times \mu_{(i,j)} \right] \qquad \text{(eq. 1)}$$

Where:

$r_{(i,j)}$ is the observed radiometric value of the location (i,j),

$r'_{(i,j)}$ is the new value of the location (i,j) after the transformation,

$\mu_{(i,j)}$ is the observed mean value of the statistic window $S_{(i,j)}$ centered at (i,j),

$\sigma_{(i,j)}$ is the observed standard deviation value of the neighborhood *S* of the location (i,j),

μ_0 is the imposed mean value given by the user,

σ_0 is the imposed standard deviation value given by the user.

Figure 9 shows an example of Envisat ASAR WSM (8bits) before and after local stretching with imposed mean=140, standard deviation=60 and statistical window=301 pixels. One sees that even if oil slicks appear clearly, the limits between the sub-swaths in the right part of the output image remain visible (blue arrows).

b. *Adaptation to a backscattering model*

Figure 10 shows an ENVISAT ASAR WSM image and its mean observed radar cross-section per column. One sees that there are 4 visible junctions between five sub-swaths in the raw image (Figure

10: right image and left cross section). In particular, the observed mean per column of the two junctions of the far range columns (junctions j3 and j4) show greater discontinuities.

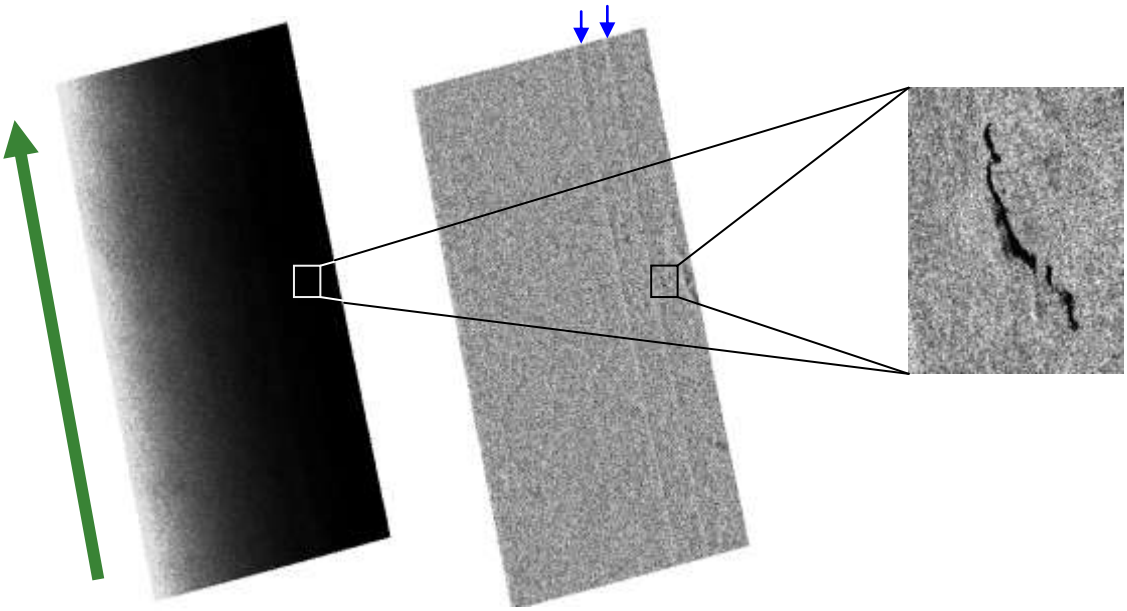

Figure 9. ASAR WSM scene before and after local stretching with imposed mean=140, standard deviation=60 and statistical window=301. On the stretched image, dark patches appear clearly but the junctions between WSM swaths remain visible (blue arrows). One concludes that the local stretching highlight oil slicks but does not correct de sub-swaths junctions.

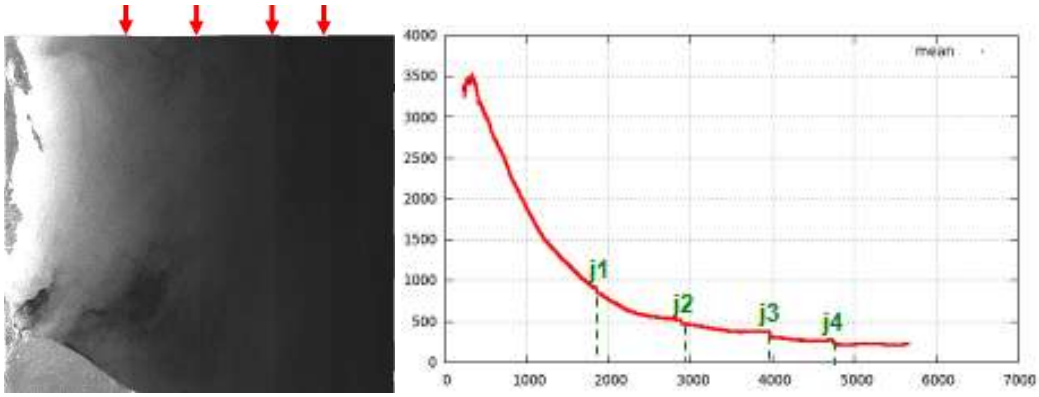

Figure 10. Example of artifacts due to the junctions between sub-swaths in the ScanSAR mode visible in ENVISAT ASAR WSM SAR image (left) and its corresponding mean observed Normalized Radar Cross-Sections (NRCS) per column.

The adaptation to a backscattering model method aims at correct the observed Normalized Radar Cross-Sections using a Geophysical Model Function (GMF). For C-Band, Multiple GMFs with the common name CMOD (C-band MODel) have been developed. CMOD5, have been successfully used in (Riazanoff and Gross, 2013) to correct WSM images. CMOD5 equation is given below (Hersbach, 2002):

$$\sigma^0{}_{CMOD5}(V,\phi,\theta) = b_0\left(1 + b_1\cos\phi + b_2\cos 2\phi\right)^{1.6} \qquad \text{(eq. 2)}$$

Where:

σ^0_{CMOD5} is the backscatter value of the model CMOD5,

V is the wind speed (m/s),

ϕ is the relative direction between the radar look direction and the wind direction,

θ is the angle of incidence,

bi (i = 0, 1, 2, 3) are the parameters of the model. They depend on the radar incidence angle and wind speed.

The CMOD5 allow estimating the radar backscattering on a scene, as a function of a surface wind speed (v), the angle between wind and radar pulse directions (φ) and the angle of incidence (θ). The method of adaptation to a CMOD consist on: 1) look for the best triple (v, φ, θ) that minimize the mean squared error between the observed NRCS and the model, 2) divide the mean (by column) of the observed NRCS by the best fit backscatter value of the model CMOD5 (v, φ, θ), 3) apply a semi-linear model to linearly adjust the values on the junction while leaving unchanged the column located at the centre of the sub-swath, and 4) apply a local stretching to correct the angle incidence effect. An example of a Envisat ASAR WSM image before and after adaptation to CMOD5 is given by Figure 11.

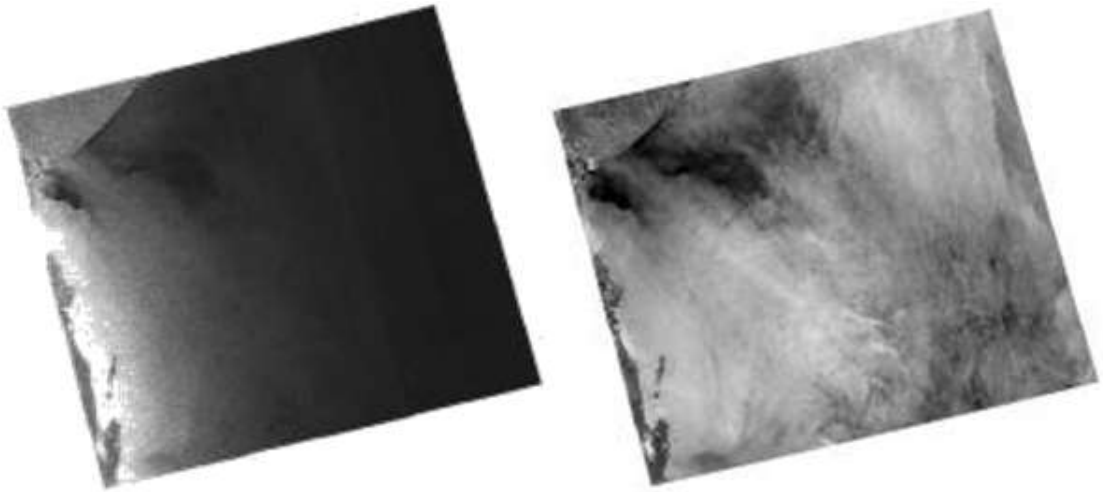

Figure 11. ASAR WSM scene before (left) and after (right) the semi-linear correction around the sub-swath junction.

C. Automatic converging thresholding

In this study, we opt for segmentation by simple thresholding. The principle of this method is to use a threshold value *T* from which the pixels whose gray level is below *T* become black, and those above become white. The output of the thresholding segmentation is a binary image. The difficulty of this technique lies in the choice of the best threshold. The best threshold varies from one oil slick class to another one. The best thresholds with the best signal/noise for an oil spill ship is low and fits for classes with the most marked signatures such as anthropogenic oil slicks, upwelling areas and wind shadow. The classes with the least marked signatures such as natural oil seeps and internal waves require higher thresholds. In our study, we proceed to a dichotomic search to look for the threshold value that minimize that gives the closest result to a manual detection by an expert. The threshold value ranges between 0 and 65535 (16bits image). In fact, each automatic detected training parcel is associated to a best threshold value and its related error. The dispersion of the best threshold and the error within the same class judge the quality of the preprocessing methods and allow selecting the best one.

D. Cleaning methods

a. Morphological closing

Closing is an important operator of mathematical morphology. Like its dual operator opening, it is derived from the fundamental operations of erosion and dilation. The closing is defined as a combination of a dilation followed by erosion using the same structuring element for both operations. It has the effect of eliminating small holes. The choice of the structuring element is important; it defines the shape of the object that we would get. Figure 12 illustrates the structuring elements using in this study.

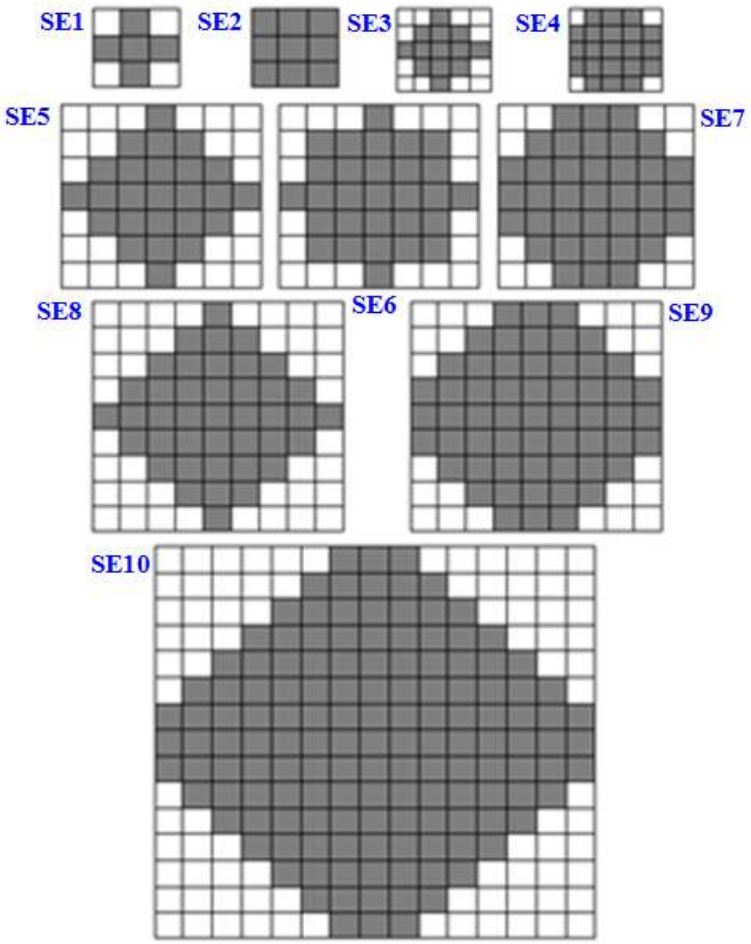

Figure 12. Structuring elements (SE) used in this study.

b. Small Object Removal (SOR)

The output of the thresholding step is a binary image which contains noise in addition to the dark patches. It needs cleaning before being exploited. The cleaning objective is to simplify the image keeping only what is important to us. In this study, we opt for a connected filtering process, i.e. a morphological opening area. This process consists of removing connected components having at least a given number of pixels. Its result depends on two parameters: the neighborhood and the size of the Smallest Component Cleaning (SCC). The neighborhood is defined from a mesh.

The mesh is the geometric structure that defines the relationship between pixels in an image. It determines from each image element *P*, the neighboring elements *V (P)*. There are different meshes that have their own properties, the main ones being the square, hexagonal and triangular meshes. The square mesh is the most common to represent images because it is compatible with the current structure of sensors and structure of raster data commonly used. For this reason, only this type of mesh will be considered here. From the square mesh, we can define two types of neighborhood, the 4-neighbors and the 8-neighbors following if we consider edges or vertices common to define the

neighboring element (Figure 13). Figure 14 shows an example of a binary image after applying an opening area respectively of a SCC of 3 pixels 4-connected and a SCC of 7 pixels 4-connected.

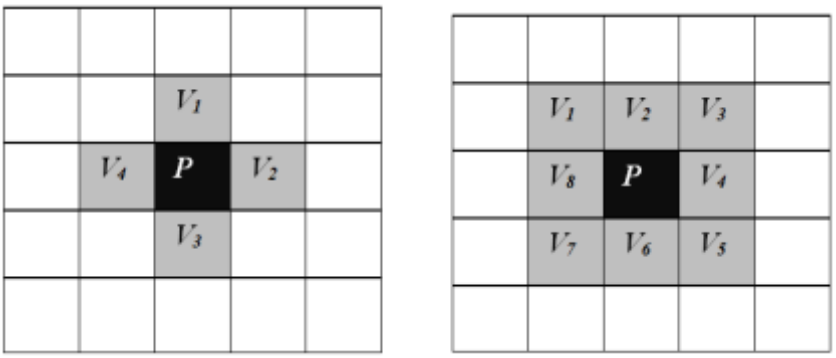

Figure 13. Types neighbourhood of square mesh: 4-neighbors (left) and 8-neighbors (right).

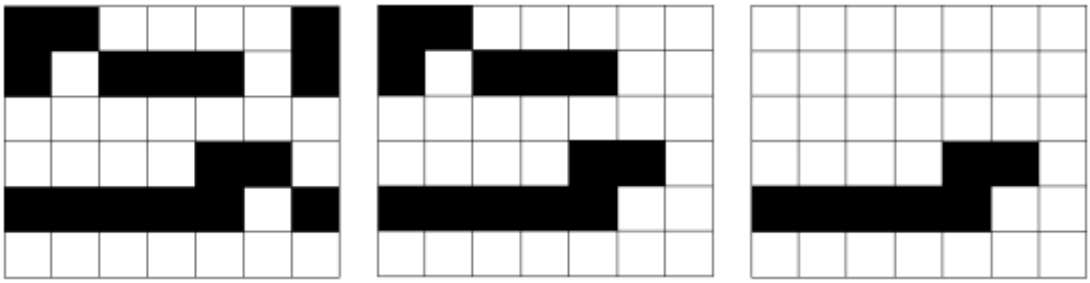

Figure 14. From left to right: the input image, the output image after the application of an opening area with a SCC of 3 pixels 4-connected, the output image after application of an opening area with a SCC of 7 pixels 4-connected.

E. Qualification engine

a. Cost function

In the literature, several methods of cost calculation are cited. In image processing, the Hamming distance is often used. It's a mathematical concept defined by Richard Hamming, and used in computers, signal processing and telecommunications to quantify the difference between two sequences of symbols. The Hamming distance between two binary images is equal to the number of positions (pixels) for which the corresponding values in the two images are different. Hamming distance in the segmentation framework gives a first indication of the quality of thresholding. Indeed, calculating the Hamming distance between an automatic thresholding and the result of the manual detection serves as a control, used to count the number of differences between the two binary images (Figure 15). The optimal threshold value is that minimizes the Hamming distance. However, the Hamming distance quantifies the difference but it gives no idea about the alteration of forms. For example, it does not allow clearly quantifying the omitted pixels and those added to the form after

thresholding. Furthermore, the Hamming distance does not nominate an optimum threshold that minimizes the error due to thresholding. These problems make the Hamming distance an unsuitable method in this context, hence the introduction of an innovative new method of calculation of the normalized omission and commission is developed herein (see below). This new method is considered as an improvement in the Hamming distance.

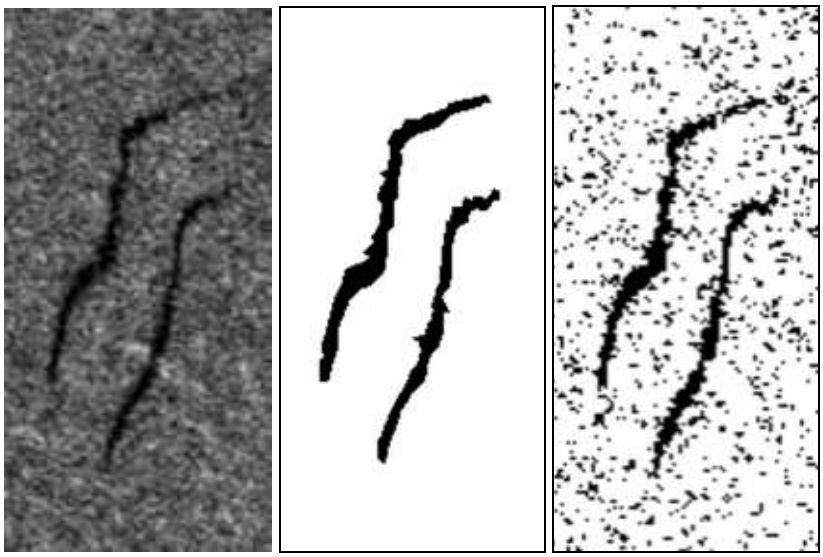

Figure 15. Manual detection Vs automatic thresholding. From left to right observed radar image, the manual detection and the automatic thresholding. One may note that it is needed to clean the left image (last step of our methodology).

The commission is the number of pixels considered as background on the image by the manual detection (training set) that are detected as dark patches by the segmentation algorithm. The omission meanwhile, represents the number of pixels that have been identified by the expert as dark patches but were identified as background by the segmentation algorithm.

Omission and commission are defined by the following formulas:

$$O_{k,T} = Card\{(i,j) \quad such \quad as \quad = \begin{cases} Tr_k(i,j) = 0 \\ Th_{k,T}(i,j) = 1 \end{cases} \qquad \text{(eq. 3)}$$

And

$$C_{k,T} = Card\{(i,j) \quad such \quad as \quad = \begin{cases} Tr_k(i,j) = 1 \\ Th_{k,T}(i,j) = 0 \end{cases} \qquad \text{(eq. 4)}$$

Where:

$Tr_k(i,j)$ is the numerical value of the pixel (i, j) in the k^{th} image manually detected,

$Th_{k,T}(i,j)$ is the numerical value of the pixel (i, j) in the k^{th} image produced by the threshold value T with the automatic thresholding algorithm,

$O_{k,T}$ is the omission of the k^{th} image produced by the threshold value T,

$C_{k,T}$ is the commission of the kth image produced by the threshold value T,

0 is the value representing the presence of dark patch,

1 is the value corresponding to the background.

The omission and commission were normalized as:

$$O'_{k,T} = \frac{O_{k,T}}{a} \quad \text{(eq. 5)}$$

$$C'_{k,T} = \frac{C_{k,T}}{A - a} \quad \text{(eq. 6)}$$

Where:

$O_{k,T}$ is the omission of the kth image produced by the threshold value T,

$C_{k,T}$ is the commission of the kth image produced by the threshold value T,

$O'_{k,T}$ is the normalised omission of the kth image produced by the threshold value T,

$C'_{k,T}$ is the normalised commission of the kth image produced by the threshold value T,

A is the number of pixels of the image,

a is the number of pixels identified as background by the expert.

Therefore, the error between the manual and the automatic detection is given by the sum of the normalized omission and commission as follows:

$$E_{k,T} = O'_{k,T} + C'_{k,T} \quad \text{(eq. 7)}$$

b. Converging thresholding and SCC

The goal here is to retain, for each SAR training parcel, the threshold value that gives a binary image as close as possible to the related training parcel manually detected. Each automatic detected training parcel is associated to a best threshold value and its related error. The dispersion of the best threshold and the error within the same class judge the quality of the preprocessing methods and allow selecting the best one. Finding the best SCC for the SOR is done in the same way. These processes are done automatically via a homemade algorithm programmed with python.

c. Parameters selection

The parameters selection and the selection of the best processing are based on three values:

Error: is the sum of the normalized commission and omission. Smaller the error is, better the processing is;

Dispersion of the best thresholds: this value is the standard deviation of the k training parcel within the same class. It assesses the quality and the sustainability of the preprocessing methods. Smaller the dispersion is, better the preprocessing is

Dispersion of the best SCC: this value is dedicated to the cleaning parameters and methods. It is calculated for the k training parcel within the same class. Smaller the dispersion is, better the processing and parameter are.

V. Results and analysis

A. Preprocessing parameters and methods selection

a. Local stretching statistic window size

Figure 16 shows the dispersion of the best thresholds and the associated mean error per class for eight statistic window sizes. One may see that the statistic window size that minimizes the dispersion of the best thresholds and the error for the mineral oil slicks is 401 pixels for Envisat ASAR WSM which corresponds to 30km.

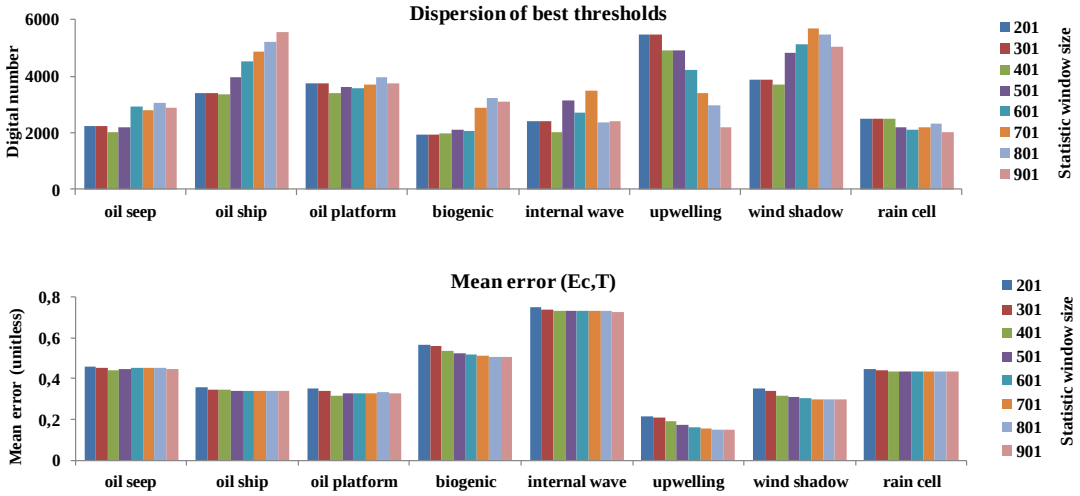

Figure 16. Local stretching statistic window size qualification. Upper panel: the dispersion of the best thresholds per class. Lower panel: the mean error per class. One may see that a statistical window with a size of 401 pixels(30km) minimize the dispersion of the best thresholds and mean error for the three classes of mineral oil slick , and hence is the better statistic window when applying a local stretching.

b. CMOD adaptation Vs local stretching

Figure 17 shows the dispersion of the best thresholds and the associated mean error per class for two preprocessing methods: local stretching and adaptation to CMOD. One can see that the preprocessing method that minimizes the dispersion of the best thresholds and the error for the mineral oil is the CMOD adaptation method.

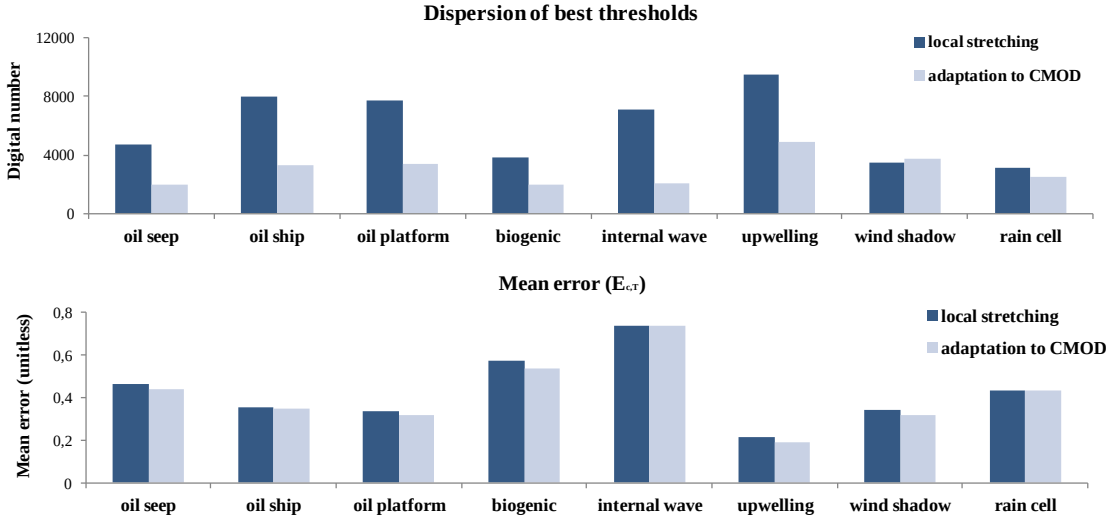

Figure 17. Preprocessing methods comparison. Upper panel: the dispersion of the best thresholds per class. Lower panel: the mean error per class. One may note that CMOD gives a much lower dispersion of the best thresholds for the same class so a better preprocessing; in contrast the 2 methods have similar Mean error.

B. Cleaning parameters and methods selection

a. Closing structuring element

Figure 18 shows the mean error per class for a maximum ten closing structuring elements. One can see that the closing structuring element that minimizes the error for the mineral oil is the structuring element ES5.

a. SOR 4-connectivity Vs SOR 8-connectivity

Figure 19 shows the dispersion of the best SCC and the associated mean error per class for two types of SOR connectivity: 4-connex and 8-connex. One can see that the connectivity that minimizes the dispersion of the best SCC and the error for the mineral oil is the 4-connectivity.

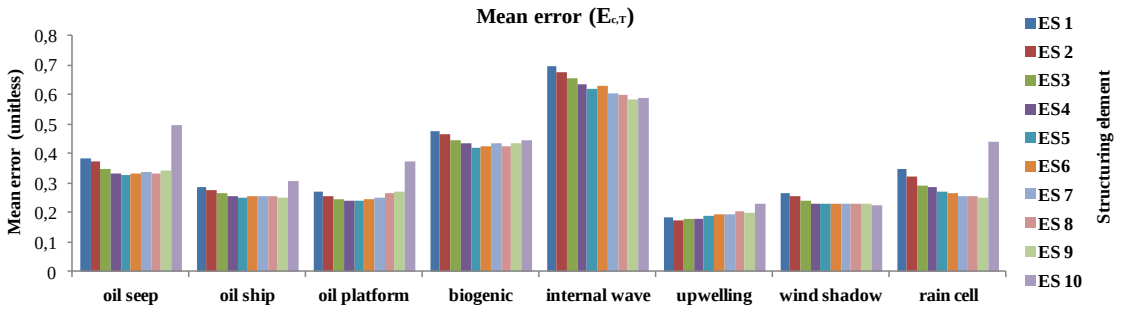

Figure 18. Mean error per closing structuring element per class. One may see that the structuring element 5 (ES5) is the best one because it minimizes the mean error for the three classes of mineral oil slicks.

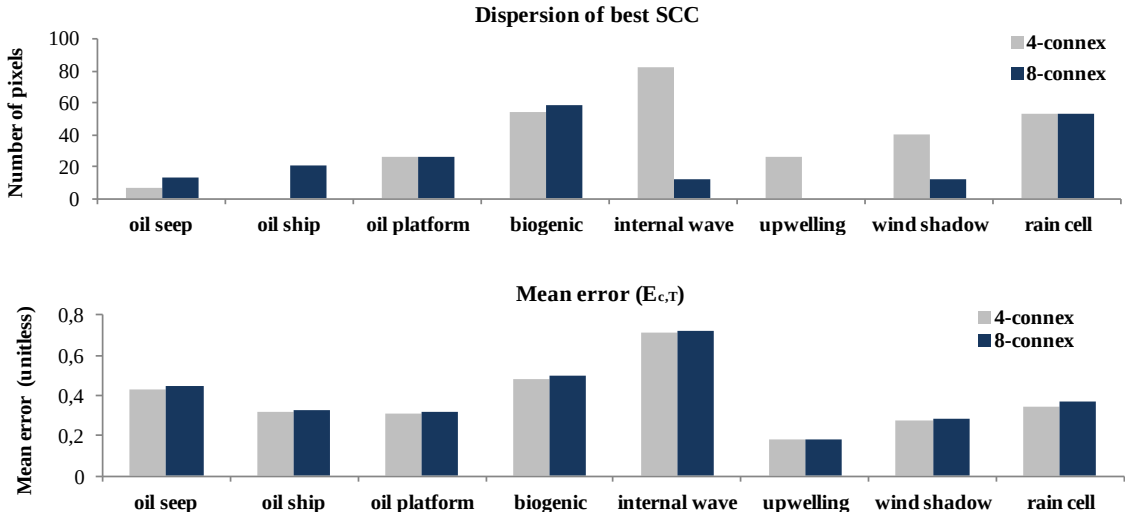

Figure 19. SOR connectivity qualification. Upper panel: the dispersion of the best SCC per class. Lower panel: the mean error per class. One may see that 4-connectivity minimizes the dispersion of the best SCC and relatively the mean error for the three classes of oil slicks and hence is the better connectivity for oil slicks detection when using à Small Object Removal (SOR).

b. SOR followed by closing Vs closing followed by SOR

Figure 20 shows the mean error per class for two cleaning methods: SOR followed by closing and closing followed by SOR. One can see that the cleaning method that minimizes the error for the mineral oil is SOR followed by closing.

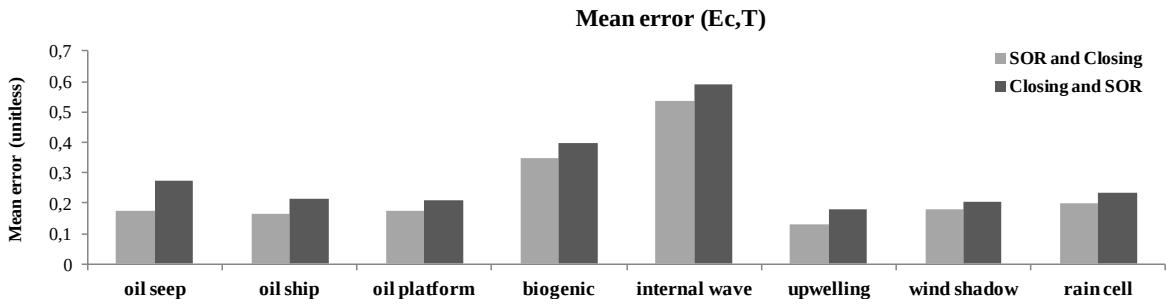

Figure 20. Mean error per cleaning method per class. One may see that a SOR followed by a morphological closing gives a better results since it minimizes the mean error for the three classes of mineral oil slicks.

VI. Conclusion and Perspectives

SAR sensors are commonly used by oil spill monitoring systems due to their well demonstrated capability of detection. The emergence of new satellites that are more efficient with larger volumes of data and better resolution makes oil slicks automatic detection a must. However, previous processing methods show some limitations regarding the heterogeneity of the SAR image which jeopardize the accuracy of the oil slicks detection. This paper proposes new preprocessing and enhancing methods that optimize the automatic detection of marine oil slicks using C-band SAR images. A training dataset of 120 training parcels have been manually performed, then used to compare and evaluate the performance of the methods herein proposed. The comparison between the preprocessing methods: local stretching and CMOD adaptation reveals that the latter was much more interesting than the local stretching in terms of homogenization of SAR radiometry and hence a better detection of mineral oil slicks. Consequently, we prove herein that an adaptation to CMOD is highly suitable to preprocess ScanSAR images. Nevertheless, local stretching can be an alternative, if there are no problems due to the acquisition mode ScanSAR. In that case, one may note that a statistic window scale of 30 km appear to be the more appropriate to enhance marine oil slicks and optimize their detection. Regarding the cleaning method, a small object removal 4-connex followed by morphological closing using the structuring element ES5 gives the best results. After the extraction of the dark patches and the elimination of some mineral oil slicks lookalikes such as internal waves and biogenic oils, a perspective should be to make an automatic classification using discriminant parameters (*e.g.* textural, morphometric, and contextual).

Acknowledgments

This work is performed as a part of a PhD research program funded by VisioTerra/UPE (Université Paris-Est) and ANRT/CIFRE. The authors would like to thank The ESA (European Spatial Agency) for the SAR scenes used in this study.

References

Alpers W. and Huhnerfuss H., 1988 “Radar signatures of oil films floating on the sea surface and the Marangoni effect,”J. Geophys. Res., vol. 93, pp. 3642–3648.

Alpers, W., 1985, "Theory of radar imaging of internal waves". Nature, 314, 245-247.

Angiuli, Emanuele, F. D. Frate, and L. Salvatori. 2006. “Neural networks for oil spill detection using ERS and ENVISAT imagery.” In Proceedings of SeaSAR’06, 23-26 January 2006, Frascati, Italy, 1–6.

Apel J.R., 1987. "Principles of ocean physics. Academic Press, 634pp.

Bliven, L., P. W. Sobieski, and C. Craeye, Rain generated ring-waves: Measurements and modelling for remote sensing, Int. J. Remote Sens., 18, 221-228, 1997.

Brekke C. and A.h.S. Solberg. 2005. "Oil Spill Detection by Satellite Remote Sensing." Remote Sensing of Environment 95 (2005): 1-13.

Chang, Lena, Z. S. Tang, S. H. Chang, and Yang-Lang Chang. 2008. “A region-based GLRT detection of oil spills in SAR Images.” Pattern Recognition Letters 29 (14): 1915–23. doi:10.1016/j.patrec.2008.05.022.

Charbonneau F. 2006. “Caractérisation du coefficient de rétrodiffusion radar des surfaces d’hydrocarbure: Modélisation et interprétation.“ Thesis (Ph.D.)-Universite de Sherbrooke (Canada), Publication Number: AAINR14847; ISBN: 9780494148471.

Craeye, C., P. W. Sobieski, and L. F. Bliven, 1997: Scattering by artifical wind and rain roughened water surfaces at oblique incidences. Int. J. Remote Sens., 18, 2241–2246.

Currie A. and Brown M. A., 1992.Wide-swath SAR. IEE Proceedings F, 139(2):123–135.

De Beukelaer, S. M., I. R. MacDonald, N. L. Guinnasso, and J. A. Murray. 2003. “Distinct Side-scan sonar, RADARSAT SAR, and acoustic profiler signatures of gas and oil seeps on the Gulf of Mexico slope.” Geo-Marine Letters 23 (3-4): 177–86. doi:10.1007/s00367-003-0139-9.

Del Frate, Fabio, D. Latini, C. Pratola, and F. Palazzo. 2013. “PCNN for automatic segmentation and information extraction from X-band SAR imagery.” International Journal of Image and Data Fusion 4 (1): 75–88. doi:10.1080/19479832.2012.713398.

Elachi C.. 1988. "Spaceborne Radar Remote Sensing: Applications and Techniques." IEEE press, ISBN 0879422416 (1988), : 288.

Espedal H. A.. 1999. "Satellite SAR oil spill detection using wind history information." International Journal of Remote Sensing 20(1999): 49-65.

Espedal, H. A. and Johannessen, O.M., 2000. Detection of oil spills near offshore installations using synthetic aperture radar (SAR). International Journal of Remote Sensing, issue 21, pages 2141-2144.

European Space Agency Web-site. 2016. http://www.esa.int/Our_Activities/Observing_the_Earth/Copernicus/SAR_missions, accessed 29 June 2016.

Fortuny-Guasch J.. 2003. "Improved oil spill detection and classification with polarimetric SAR." Proc. workshop on Application of SAR Polarimery and Polarimetric Interferometry, ESA-ESRIN Frascati, Italy (2003): 14–16.

Garcia-Pineda, Oscar. 2009. “Spatial and temporal analysis of oil slicks in the gulf of Mexico based on remote sensing”. Texas A&M University.

Gasull, A., X. Fábregas, J. Jiménez, F. Marqués, V. Moreno, and M. A. Herrero. 2002. “Oil spills detection in SAR images using mathematical morphology.” In 11th European Signal Processing Conference (EUSIPCO 2002), 25–28. Toulouse, France. doi:10.1.1.81.3086.

Girard-Ardhuin, Fanny, G. Mercier, and R. Garello. 2003. “Oil slick detection by SAR imagery: potential and limitation.” Oceans 2003. Celebrating the Past. Teaming Toward the Future (IEEE Cat. No.03CH37492). Ieee, 164–169 Vol.1. doi:10.1109/OCEANS.2003.178539.

Gower, J. F. R., 1994, Mapping coastal currents with SAR, using naturally-occurring surface slick patterns, Proceedings of the Second ERS-2 Sympostum, Eur. Space Agency Spec. Publ., ESA SP-, 361, 415–418.

Hersbach Hans, 2002. CMOD5 : An improved geophysical model function for ERS C-band scatterometry, Research Department, ECMWF.

Hu C., Li X., and Pichel W. G., 2011.“Detection of oil slicks using MODIS and SAR imagery,” in Handbook of Satellite Remote Sensing Image Interpretation: Applications for Marine Living Resources Conversation and Management, J.V. Morales, T.P. Stuart, and S. Sathyendranath, eds. (EU PRESPO and IOCCG, Dartmouth, Canada, 2011).

Jackson C. R. and Apel J. R., 2004. Synthetic Aperture Radar marine user's manual. NOAA, Washington, DC, pp 464.

Johannessen, O.M.; Alexandrov, V.; Frolov, I.Y.; Sandven, S.,;Pettersson, L.H.; Bobylev, L.P.; Kloster, K.; Smirnov, V.G.; Mironov, Y.U. and Babich, N.G., 2007. Remote Sensing of Sea Ice in the Northern Sea Route: Studies and Applications. Praxis Publishing, UK, pp 179-180.

Jones C., Minchew B. and Holt B., 2011. "Polarimetric decomposition analysis of the Deepwater Horizon oil slick using L-band UAVSAR data," 2011 IEEE International Geoscience and Remote Sensing Symposium, Vancouver, BC, 2011, pp. 2278-2281. doi: 10.1109/IGARSS.2011.6049663.

Kanaa, T. F. N., E. Tonye, G .Mercier, V. P. Onana, J. M. Ngono, P. L . Frison, J. P. Rudant, and R. Garello. 2003. "Detection of oil slick signatures in SAR images by fusion of hysteresis thresholding responses." In IGARSS 2003. 2003 IEEE International Geoscience and Remote Sensing Symposium. Proceedings (IEEE Cat. No.03CH37477), 4:2750–52. IEEE. doi:10.1109/IGARSS.2003.1294573.

Liu, A. K., C. Y. Peng, and S. Y. Chang. 1997. "Wavelet analysis of satellite images for coastal watch." IEEE Journal on Ocean Engineering 22 (1): 9–17.

Mercier G.; Girard-Ardhuin F., 2 006. Partially Supervised Oil Slick Detection by SAR Imagery using Kernel Expansion, IEEE-TGRS, vol 44(10), pp 2839-2846.

Moore R. K., Claassen J. P., and Lin Y. H. 1981. Scanning spaceborne Synthetic Aperture Radar with integrated radiometer. IEEE Trans. on Aerospace and Electronic Systems, 17(3):410–420.

Moore R., Yu Y., Fung A., Kaneko D., Dome G. and Werp R., 1979, "Preliminary study of rain effects on radar scattering from water surfaces," in IEEE Journal of Oceanic Engineering, vol. 4, no. 1, pp. 31-32,. doi: 10.1109/JOE.1979.1145408.

Najoui Z., Deffontaines B., Xavier J. P. and Riazanoff S., 2017, " Wind Speed and Instrument Modes Influence on the Detectability of Oil Slicks using SAR Images: a Stochastic Approach", submitted to Remote Sensing of Envirnment.

Nystuen, J. A. (1990), A note on the attenuation of surface gravity waves by rainfall, J. Geophys. Res., 95(C10), 18353–18355, doi:10.1029/JC095iC10p18353.

Ochadlick Jr., A. R., P. Cho, and J. Evans-Morgis 1992, Synthetic aperture radar observations of currents colocated with slicks, J. Geophys. Res., 97(C4), 5325–5330, doi:10.1029/91JC01995.

Pellon de Miranda, Fernando, A. M. Q. Marmol, E. C. Pedroso, C. H. Beisl, P. Welgan, and L. M. Morales. 2004. "Analysis of RADARSAT-1 data for offshore monitoring activities in the Cantarell complex, Gulf of Mexico, using the Unsupervised Semivariogram Textural Classifier (USTC)." Canadian Journal of Remote Sensing 30 (3): 424–36. doi:10.5589/m04-019.

Riazanoff S. and Gross K., 2013. Enhancing ENVISAT ASAR WSM Segments To Detect Oil Spills In the Framework Of The "20 Years Of Oil Routes" Project. ESA Living Planet Symposium,

Proceedings of the conference held on 9-13 at Edinburgh in United Kingdom. ESA SP-722. 2-13, p.229.

Robinson, I. S.. 1994. "Satellite oceanography. An introduction for oceanographers and remote-sensing scientists." Wiley–Praxis series in remote sensing (1994): 455.

Shu Y.; Li J.; Yousif H. and Gomes G., 2010. Dark-spot detection from SAR intensity imagery with spatial density thresholding for oil-spill monitoring. Remote Sensing of Environment, Volume 114, Issue 9, 15 September 2010, pp 2026 - 2035.

Smith, R. L. 1968, "Upwelling", Oceannogr. Mar. Biol. Ann. Rev., 6: 11-46.

Solberg, A. H. S., G. Storvik, R. Solberg, and E. Volden., 1999. Automatic detection of oil spills in ERS SAR images. IEEE Transactions on Geoscience and Remote Sensing 37 (4): 1916–24. doi:10.1109/36.774704.

Topouzelis, Konstantinos N. 2008. "Oil spill detection by SAR Images: Dark formation detection, feature extraction and classification algorithms." Sensors 8 (10): 6642–59. doi:10.3390/s8106642.

Tsimplis, M., 1992, "The effect of rain in calming the sea", J. Phys. Oceanogr., 33, 404–412.

Wismann V., "Radar signatures of mineral oil spills measured by an airborne multi-frequency radar and the ERS-1 SAR," in Proc .IGARSS, Tokyo, Japan, Aug. 18–21, 1993, pp. 940–942.

Xu L.; Li J. and Brenning A.. 2014. "A comparative study of different classification techniques for marine oil spill identification using RADARSAT-1 imagery." Remote Sensing of Environment141 (2014): 14-23.

Xu L.; Shafiee M. J.; Wong A.; Li F.; Wang L.; and Clausi D. A, 2015. Oil spill candidate detection from SAR imagery using a thresholding-guided stochastic fully-connected conditional random field model. CVPR, pp 86.

2.3 Conclusion du chapitre

Les capteurs radar sont couramment utilisés par les systèmes de surveillance des déversements d'hydrocarbures en raison de leur capacité de détection bien démontrée. L'émergence de nouveaux satellites qui sont plus efficaces avec de plus grands volumes de données rend la détection automatique des nappes d'huile un besoin. Toutefois, la détection des nappes d'huile est un phénomène multivarié qui dépend de plusieurs paramètres. Notre approche consiste à isoler ses paramètres un par un. Cet article propose des méthodes de prétraitement et d'amélioration qui optimisent la détection automatique des nappes marines en utilisant des images radar à bande C. Un ensemble d'apprentissage de 120 parcelles d'entrainement a été réalisé manuellement.

Les résultats obtenus prouvent qu'une adaptation au CMOD convient parfaitement au prétraitement des images ScanSAR. Elle homogénéise les images et met en évidence les nappes de pétrole. L'étirement local peut être une alternative s'il n'y a pas de problème dû au mode d'acquisition ScanSAR. Dans ce cas, la fenêtre statistique de 30 km est la plus appropriée pour améliorer les nappes marines et optimiser leur détection. En ce qui concerne la méthode de nettoyage, une ouverture par zone 4-connexe suivie d'une fermeture morphologique à l'aide de l'élément structurant ES5 donne de bons résultats. Après la segmentation des corps sombres et l'élimination de certaines sosies d'huiles minérales tels que les vagues internes et les huiles biogéniques, une perspective serait de faire une classification automatique en utilisant des paramètres discriminants (structuraux, morphométriques et contextuels).

Chapitre 3 Détectabilité des nappes d'hydrocarbures

Résumé du chapitre

La détection des nappes d'hydrocarbures à partir des images radar est considérablement entravée par les conditions de vent et dépend des propriétés du capteur. Si des approches empiriques existent déjà, l'article qui fait l'objet de ce chapitre a le mérite - pour la première fois - d'effectuer une étude statistique basée sur du BigData qui vise, d'une part, à déterminer et à prouver l'intervalle de vitesse de vent qui optimise la détection des nappes d'huile dans toutes les images radar et, d'autre part, d'évaluer le comportement de la détectabilité des nappes d'huile par rapport à l'intensité de la vitesse du vent. De plus, il évalue également l'influence du mode d'instrument radar sur la détectabilité des nappes. Pour mener à bien cette étude, nous avons utilisé une base de données de 1333 images radar collectées entre 1992 et 2015 à partir de trois missions de l'Agence Spatiale Européenne (ESA): ERS-1/2, Envisat et Sentinel-1. Cette base de données, qui couvre quatre zones d'intérêt représentatives importantes, nous a permis d'effectuer un jeu de données de 3903 nappes de pétrole détectées manuellement. Les résultats de cette détection manuelle et en particulier le nombre de nappes d'hydrocarbures détectées ont été reliés aux vitesses du vent au moment de l'observation calculées à partir de données basées sur un modèle météorologique global classique (ECMWF). L'analyse des résultats de notre approche stochastique a révélé que la détectabilité de 95% des occurrences de nappes de pétrole, en supposant une distribution gaussienne, se situe entre des vitesses de vent de 2,09 m/s et 8,33 m/s. En procédant à une normalisation statistique de la distribution de la vitesse du vent, l'analyse a également révélé que la détectabilité - contrairement à ce qui est connu jusqu'à présent - augmente presque linéairement avec la vitesse du vent à l'intérieur de l'intervalle de vent 2,09 m/s - 8,33 m/s. De plus, les résultats expérimentaux obtenus sur 5 modes d'acquisition (PRI, APP, IMP, WSM et IW) démontrent que les performances de la détection des nappes dépendent du type de modes. Parmi les modes déjà cités, le mode IW est de loin le plus intéressant pour la détection de nappes de pétrole, vient après APP, PRI, IMP, et finalement WSM, qui semble étroitement liée à la résolution spatiale. Notre analyse statistique de l'association des cinq modes et de la résolution spatiale montre que la détectabilité est plus élevée sous des vitesses de vent élevées pour le mode qui a la meilleure résolution spatiale (IW).

3.1 Introduction du chapitre

Toujours dans l'optique d'optimiser la détection des nappes d'huile à partir des images radar, le présent chapitre traite de l'influence de la vitesse du vent et des paramètres du capteur sur la détectabilité des nappes huile.

La capacité d'un capteur radar à détecter les nappes d'huile dépend des conditions météorologiques, des propriétés du capteur (polarisation, angle d'incidence, résolution spatiale, longueur d'onde, etc.), des propriétés de l'huile, de la saisonnalité, de la température de l'eau, de la salinité, etc. Le présent chapitre met en évidence deux de ces paramètres, à savoir la vitesse du vent et le mode du capteur, qui influencent fortement la détectabilité des nappes d'huile. Quelle est l'intervalle de vitesse de vent qui nous amène à visualiser et à extraire automatiquement les nappes d'huile? Quels sont les autres intrants majeurs que l'on peut déduire d'une analyse stochastique du BigData en matière d'images radar? Le présent chapitre vise à apporter des solutions à ces questions.

Diverses études ont été menées pour juger de la plage de vitesse du vent qui optimise la détection des nappes d'huile sur les images radar. Les intervalles de vitesse de vent proposés sont de 3 à 7-10 m/s (Brekke et Solberg, 2005), de 3,5 à 7 m/s (Garcia-Pineda et al., 2009), de 1,5 à 10 m/s (Fingas et Brown, 2014) et 1 à 7 m/s (Marghany, 2014a). Cependant des différences notables, que ce soit sur le plan approches ou encore résultats, sont à prendre en considération. Toutes ces études sont empiriques et aucune étude statistique explicite n'a été présentée. Les dites études se sont focalisées sur des cas d'accidents pétroliers marins à l'image du *Deep Water Horizon* survenu au Golf du Mexique en 2010 et dont la nature d'huile est très particulière. Ainsi, les données de vent utilisées dans certaines études sont trop ponctuelles (à partir de bouées) et ne sont donc pas représentatives. En outre, dans une perspective d'automatisation de la détection des nappes marines à l'échelle mondiale, les vitesses de vent indiquées varient considérablement et ne tiennent pas compte de la diversité géographique, de tous les types de nappes d'huile et leur âges, des saisons, etc. Pour combler ces lacunes nous proposons une étude statistique basée sur une approche stochastique. L'étude se base à un grand nombre d'échantillons pour obtenir une plage optimale de vitesse du vent qui optimise la détection des nappes d'hydrocarbures à l'échelle mondiale et comparer les performances de 5 modes d'acquisition radar sur la détectabilité des nappes d'huile sous différentes vitesses de vent.

Dans la présente étude, 1333 images et un échantillon de 3903 nappes d'huile (de différentes natures et origines) ont été analysées, ce qui confère aux résultats un caractère, nous osons dire, d'exhaustivité. Au-delà du grand intérêt de traiter une énorme quantité d'images radar, nous avons voulu appliquer notre méthodologie à différentes zones avec différents contextes météorologiques et géographiques. Quatre zones d'intérêt étendues ont été choisies pour cette étude: Nord du Pérou (qui s'étend sur le sud de l'Équateur et le nord du Pérou); Côte ouest africaine (Gabon, Congo et Angola); Santa Barbara (sud

de la Californie) et la mer Caspienne. Les nappes de pétrole qui se produisent dans ces quatre régions proviennent à la fois de suintements d'hydrocarbures naturels et de déversements d'hydrocarbures.

Les images radar utilisées proviennent de trois missions radar de l'Agence Spatiale Européenne et qui sont ERS-1/2, Envisat et Sentinel-1. Les 5 modes utilisées dans cette étude sont : PRI (ERS-1/2), APP (Envisat), IMP (Envisat), WSM (Envisat) et IW (Sentinel-1). Les données de vent utilisées proviennent du modèle de prévision numérique du temps (NWP) du Centre européen de prévisions météorologiques à moyenne échelle (ECMWF).

3.2 Manuscrit 2: Wind speed and instrument modes influence on the detectability of oil slicks using SAR images: a stochastic approach

Zhour Najoui [a,b], Benoit Deffontaines [a], Jean-Paul Xavier [b], Serge Riazanoff [a,b], Guillaume Aurel [b]

[a]Laboratoire de REcherche en Géodésie, LAREG, Université Paris-Est, et Institut Géographique National, Marne-la-Vallée, France, zhour.najoui@univ-paris-est.fr, benoit.deffontaines@univ-mlv.fr, serge.riazanoff@univ-mlv.fr

[b]VisioTerra, Champs-sur-Marne, France, zhour.najoui@visioterra.fr, serge.riazanoff@visioterra.fr, jean-paul.xavier@visioterra.fr, guillaume.aurel@visioterra.fr

Abstract

The detection of marine oil slicks from Synthetic Aperture Radar (SAR) images is considerably hampered by wind conditions and depends on sensing properties. If empirical approaches already exist, this paper has the merit - for the first time - to conduct a statistical study, based on SAR BigData that aims on the one hand, to determine and prove the wind speed range that optimizes the detection of oil slicks in all SAR images, and, on the other hand, to evaluate the behavior of the oil slicks detectability regarding the wind speed intensity. Moreover, it also assesses the influence of the radar instrument mode on slicks detectability. To carry out the present study, a database of 1333 SAR images collected between 1992 and 2015 from three European Spatial Agency (ESA) missions: ERS-1/2, Envisat, and Sentinel-1, has been used. This database which covers four representative large areas of interest has allowed us to perform a dataset of 3903 manually detected oil slicks. The outcome of this manual detection and in particular the number of detected oil slicks, have been linked to the wind speeds computed from observations based on a classic meteorological global model at the time of observation (ECMWF). The analysis of the results of our stochastic approach revealed that the detectability of 95% of oil slicks occurrences, assuming a Gaussian distribution, ranges between 2.09 m/s and 8.33 m/s. By processing a statistical normalization of the wind speed distribution, the analysis revealed also that the detectability - contrary to what is known hitherto - increases almost linearly with the wind speed. Moreover, the experimental results obtained on 5 acquisition modes (PRI, APP, IMP, WSM, and IW) demonstrate that the performance of oil slicks detectability depends on the type of modes. Among them, IW mode is far to be the most interesting for oil slicks detection, comes after APP, PRI, IMP, and finally WSM, which seems closely linked to the spatial resolution. Our statistical analysis of the association of the five modes and spatial resolution shows that the detectability is higher under high wind speed for sensor modes with the best spatial resolution (IW).

Keywords

SAR, Oil slick, Detectability, Marine environment, Wind speed, Sensor mode.

I. Introduction

Given the stakes they represent, marine oil slicks (floating oil covering an area of water), and their detection-especially from SAR images- have been the subject of several studies in recent years. The reason being the impact that oil has on marine ecosystems, fisheries and wildlife, but also the economic interest they can represent. Oil slicks have a multitude of sources (natural oil seeps leaked from petroleum reservoir and anthropic oil spills discharged from ship or petroleum platform), and are present in substantial quantities on the sea surface. As an example, in a quantitative way, the Joint Group of Experts on the Scientific Aspects of Marine Environmental Protection (GESAMP, 2007), estimated the average total worldwide annual release of petroleum from all known sources to the sea to be 1 245 200 tons per year. According to GESAMP (2007), this amount of oil is divided equally between natural oil seeps and oil spills. All this shows the importance of detecting oil slicks to identify polluted areas and to assess the drift of these slicks in order to protect the coasts. In addition to the environmental application, the detection of oil slicks and especially natural oil seepage is a good indicator to assess the presence and the maturity of an oil reservoir which plays a major role in oil exploration/production.

Marine oil slicks detection represents a key where end users needs and aims. However, if the needs and the aims of the detection of marine oil slicks are clear and well defined, the detection remains a complicated task because of various weather conditions and remote sensing parameters. SAR images have proven to be a useful tool for oil slick mapping due to the dampening effect that oil has on capillary and small gravity waves, called Bragg waves. The latter are generated on water by local winds and they are responsible for the radar backscattering (Gades and Alpers, 1998; Alpers and Espedal 2004; Jackson and Apel, 2004; Mercier and Girard-Ardhuin, 2006; Shu et al., 2010; Xu et al., 2015). As a consequence, oil slicks appear darker compared to the brighter radar backscatter produced by Bragg waves. According to Bragg theory, the backscattered radar power is proportional to the spectral energy density of Bragg waves. Therefore, beyond certain conditions related to the wind speed, oil may become undetectable (Buchroithner, 2001; Brekke and Solberg, 2005).

The capability of a SAR sensor to detect marine oil slicks is a multivariate issue. For instance, it depends on the weather conditions, sensor properties (polarization, signal to noise ratio, incidence angle, spatial resolution, wavelength, etc.), oil properties, seasonality, water temperature, salinity, etc (Skrunes et al., 2012). A variety of studies have been carried out about the range of wind speed that optimizes the oil slicks detection on SAR images. Wind speed requirement has been reported to be 3 to 7-10 m/s (Brekke and Solberg, 2005), 3.5 to 7 m/s (Garcia-Pineda et al., 2009), 1.5-10 m/s (Fingas and Brown, 2014), and 1 to 7°m/s (Marghany, 2014a). However, all of these studies are empirical and no explicit statistical study has been presented. Thus, wind data used in some studies are too punctual (from buoys) and consequently are not representative. Furthermore, in an automation perspective of the detection of marine oil slicks on a global scale, the reported wind speed ranges vary considerably

and does not take into account the geographical diversity, all oil slick types, seasons, slick age, etc. Our objective is to tackle these gaps by using a stochastic approach based on a high number of samples to give an optimal range of wind speed that optimizes oil slick detection on a global scale and compare the performance of 5 SAR modes on oil slicks detectability under different winds speed.

In this study we focus on the two following parameters, wind speed and sensor mode, which strongly influence the oil slicks detectability using a stochastic approach. So our paper aims at answering the questions: what is the range of wind speed and the SAR modes that optimize the oil slick detection using a statistic study? What other major inputs can we deduce from a stochastic and statistical analysis of a large dataset of radar images? And how the outcome can make more reliable the recognition of marine oil slicks and optimize further automatic detection?

II. Materiel and Methods

A. Data used

a. SAR dataset

Several spaceborne SAR systems have been used for oil slicks monitoring (Liu et al., 1997; Espedal, 1999; Gad and Alpers, 1999; Solberg et al., 1999; Del Frate et al., 2000; Fiscella et al., 2000; Marghany, 2001; Gasull et al., 2002; Kanaa et al., 2003; Alpers et al., 2004; Brekke and Solberg, 2005; Angiuli et al., 2006; Chang et al., 2008; Garcia-Pineda et al.,2008; Topouzelis, 2008; Garcia-Pineda et al., 2009; Del Frate et al.,2013; Marghany, 2014; Xu and Brenning, 2014; Marghany, 2015; Suresh et al., 2015). In this study we used SAR images from 3 ESA's missions: ERS-1/2 (1992-2010), Envisat ASAR (2002-2012), and Sentinel-1 (2014-2015). The three sensors operates in the C-band in a wide variety of modes that provide numerous functions such as observations of different polarities of the signal or that combine different polarities, angles of incidence, and spatial resolutions. The following five types of products described below (Table 3) have been used and compared:

(i) Wide Swath Medium-resolution mode (WSM) gives a 400 km by 400 km wide swath image. It operates in one of two polarizations types, either HH or VV.

(ii) Alternating Polarization mode Precision image (APP) gives two co-recorded images per acquisition either in HH and VV polarizations, HH and HV or VV and VH.(iii) Image Mode Precision image (IMP) generates high-spatial-resolution data products (30 m for precision images) selected from the total of seven available swaths. Its swath width ranges between 56 km (swath 7) and 100 km (swath 1) across-track. It operates in one of two polarizations types, either HH or VV.

(iii) Image Mode Precision image (IMP) generates high-spatial-resolution data products (30 m for precision images) selected from the total of seven available swaths. Its swath width ranges between

56 km (swath 7) and 100 km (swath 1) across-track. It operates in one of two polarizations types, either HH or VV.

(iv) PRI mode (PRecision Image) gives a 100 km by 100 km wide swath image with a spatial resolution of 30 m by 26.3 m. It operates in VV polarization.

(v) Interferometric Wide swath mode (IW) acquires data with a 250 km swath at 5 m by 20 m spatial resolution (single look). IW mode captures three sub-swaths using Terrain Observation with Progressive Scans SAR (TOPSAR). It operates in single (HH or VV) or dual polarization (HH and HV or VV and VH).

Table 3 Summary of SAR images used in this study (number of scenes) and their characteristics (spatial resolution, pixel spacing, swath width, and incidence angle). The total number of SAR images used is 1333. Spatial resolution is a measure of the system's ability to distinguish between adjacent targets. Pixel spacing is the distance between adjacent pixels in an image, measured in meters. Product overviews: European Space Agency (2016).

Sensor	Product type	Spatial resolution (m)	Pixel spacing (m)	Swath width (km)	Incidence angle	Number of scenes
Envisat ASAR	WSM	150*150	75*75	400	15 - 45	636
	APP	30*30	12.5*12.5	100	15 - 45	46
	IMP	30*30	12.5*12.5	100	15 - 45	96
ERS-1/2	PRI	30*26.3	12.5*12.5	100	20 - 26	324
Sentinel-1	IW	5*20	10*10	250	29.1 - 46.0	231
						Total : 1333

In this study, all of the used SAR scenes are co-polarized (HH or VV). The reason is that many studies discuss the potential of sensor polarization for oil slicks detection (Elachi, 1988; Robinson, 1994; Fortuny-Guasch, 2003; Jackson and Apel, 2004) and they highlight that the cross- polarized (VH, HV) ocean backscattering is considerably less efficient than the co-polarized backscattering (VV, HH). An example showing the influence of the polarization on the oil slicks detectability is presented in Figure 21 and Figure 22. Figure 21 - (A-1) and (A-2) present two images acquired from Envisat ASAR (C-band, mode APP) on 09 September 2005 at 03:55 UTC respectively with HV polarization (A-1) and HH polarization (A-2). In agreement with the bibliography, one can see that cross polarization (HV)

does not provide more results than HH (Figure 21**)**. The oil slicks detected by HH polarization (A-2) are absolutely undetectable using HV polarization (A-1). Figure 22 - (B-1) and (B-2) present two images acquired from Envisat ASAR (C-band, mode APP) on 21 August 2005 at 03:52 UTC respectively with VV polarization (B-1) and HH polarization (B-2). The VV polarization generally gives the same radar backscattering as HH polarization in C-band.

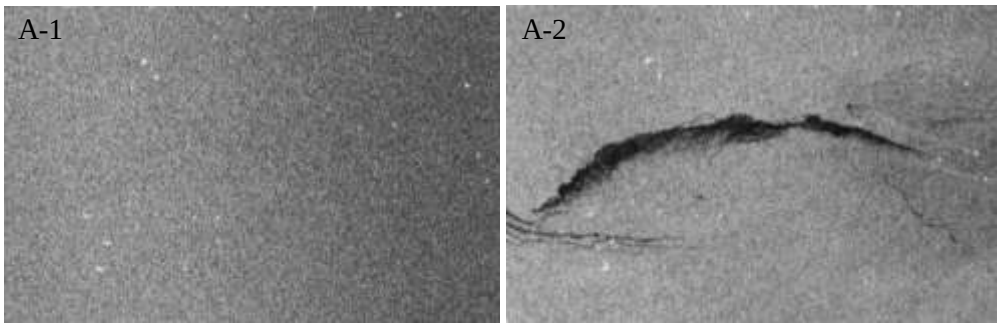

Figure 21. The influence of the polarization on the oil slicks detectability. SAR images acquired from Envisat ASAR (C-band, mode APP) on 09 September 2005 at 03:55 UTC with HV polarization (A-1), and HH polarization (A-2)

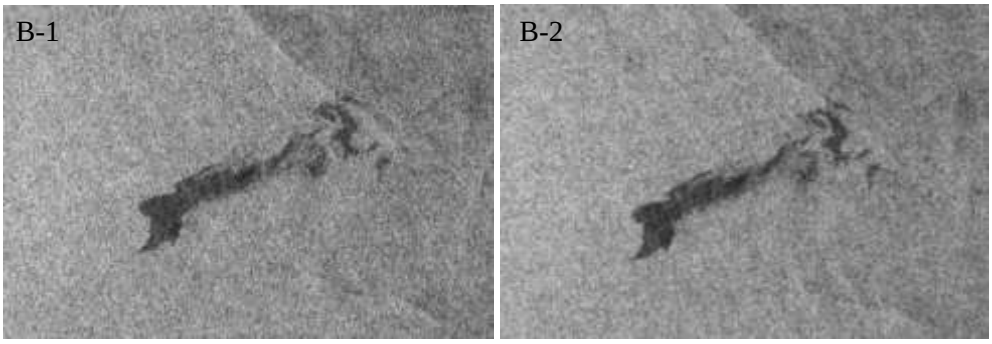

Figure 22. The influence of the polarization on the oil slicks detectability.SAR images acquired from Envisat ASAR (C-band, mode APP) on 21 August 2005 at 03:52 UTC with VV polarization (B-1) and HH polarization (B-2).

b. Wind speed data

In order to determine the wind speed range that optimizes the detection of slicks in SAR images, we used wind speed data that comes from the operational Numerical Weather Prediction (NWP) model of the European Centre for Medium-Range Weather Forecasts (ECMWF). ECMWF model has a global spatial coverage. Its wind fields have a temporal resolution of 6 hours and are defined at 10-m above sea level. According to Dee et al. (2011), used data has a bias of -0.1°m/s that we consider negligible and a normalized standard deviation of 16%.

B. Methodology

As previously explained, the detectability of oil slicks on SAR images depends on several parameters; we focus here on wind speed and SAR modes. Indeed, in this paper, we take advantage of over thousand available SAR images from three radar missions (ERS, Envisat, and Sentinel-1) to carry out a stochastic analysis of oil slicks detectability according to wind speed and SAR modes. Beyond the high interest to process a huge amount of radar images, we definitely wanted to apply it to different zones with different meteorological and geographical contexts. Four Areas Of Interest (AOI) have been chosen for this study: North of Peru (that extends over Southern Ecuador and Northern Peru); West African coastline (Gabon, Congo, and Angola); Santa Barbara (Southern California), and southern Caspian Sea. The oil slicks occurring in these four regions come from both natural oil seeps and oil spills.

Figure 23 presents the methods of data preprocessing and manual detection which are described below.

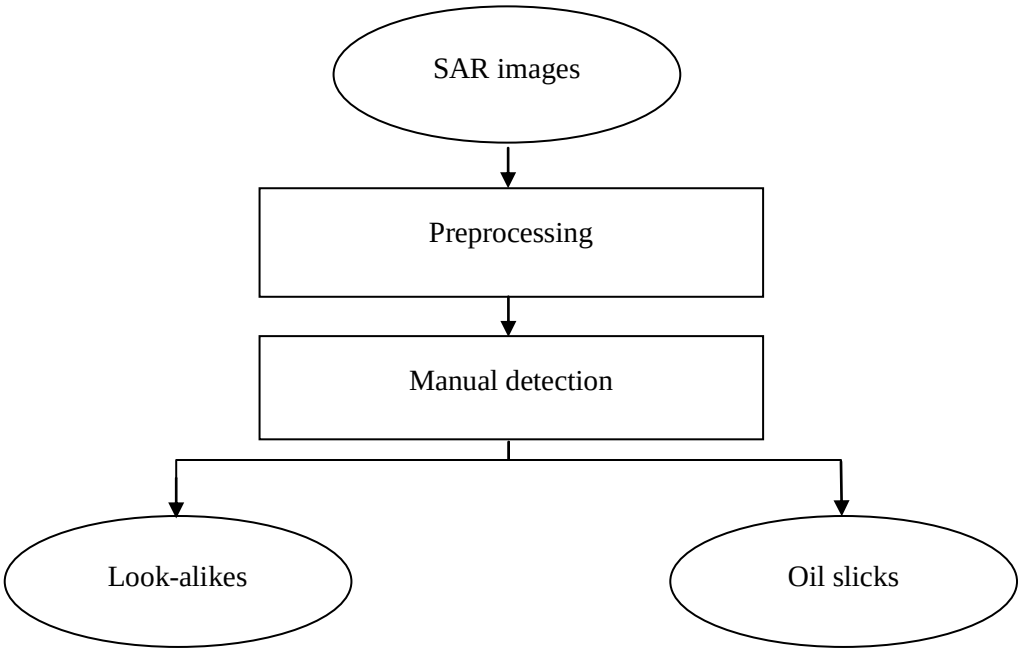

Figure 23. Methodological framework for data preprocessing and manual detection.

a. Image preprocessing

All radar images have been georeferenced in the geographic coordinate reference system over the WGS84 ellipsoid, datum WGS84. A land mask has been applied and the images have been

radiometrically corrected. The radiometric correction consists on correcting the brightness variations due to SAR peculiarities. Indeed, the radar backscattering on offshore area is mainly guided by non-Lambertian reflections (the surface does not reflect the radiation uniformly in all directions). This non-Lambertian reflection leads to heterogeneity of the brightness in the radar image. The images are processed in 16-bits Digital Number (DN). In order to homogenize the radiometry of all SAR images, the sea part is stretched linearly with a sliding window. After several tests to overcome the problem of brightness and heterogeneity, the best standard stretching choice in order to equalize all SAR images is a mean of 33410 and a standard deviation of 20560, in all parts of the output image.

b. Manual detection

In addition to oil slicks, many phenomena may appear as dark in SAR images. Non-oil dark patches are termed as look-alikes features that include upwelling, eddies, rainfalls, wind shadows, bathymetry, internal waves, current shear zones, etc. (Espedal, 1999; Brekke and Solberg, 2005; Xu and Brenning, 2014).

Three approaches exist for oil slick detection in SAR images: a manual approach conducted by trained human operators who analyze images to detect oil slicks, the semi-automatic approach where a computer detects all the black bodies in the SAR image using different techniques of segmentation after which an experienced human operator classifies these objects as slicks or look-alikes, and finally the automatic system that uses complicated image processing and programming techniques to perform both segmentation and classification.

If we did not found examples of manual detection in the bibliography, the semi automatic and automatic segmentation and classification are widely illustrated below. Some used segmentation, or dark spot extraction techniques are adaptive thresholding (Solberg et al., 1999), hysteresis thresholding (Kanaa et al., 2003), edge detection using Laplace of Gaussians or Difference of Gaussians (Chang et al., 2008), wavelets (Liu et al., 1997) and mathematical morphology (Gasull et al., 2002). Neural network based segmentation techniques were demonstrated in Garcia-Pineda et al. (2009), Angiuli et al. (2006), and Del Frate et al. (2013). Some automatic oil slick detection algorithms are "Classifiers" using a Gaussian density function based on statistical model approach (Solberg et al., 1999), a Mahalanobis classifier (Fiscella et al., 2000), neural networks (Del Frate et al.,2000; Garcia-Pineda et al.,2008; Del Frate et al.,2013) , texture analysis, (Marghany, 2001), genetic algorithm (Marghany, 2014 and Marghany, 2015), multi-objective entropy evolutionary algorithm (Marghany, 2014) and Automatic Seep Location Estimator (Suresh et al., 2015).

Due to the real unknown accuracy of the semi-automatic and automatic approach, we focus below on a reliable manual detection approach. The manual detection is based on the "Synthetic Aperture Radar marine user's manual" (Jackson and Apel, 2004). Each of the 1333 SAR images has been manually

interpreted independently from the others. Each oil slick has been categorized depending on the interpretation based on morphological and textural criteria. Thereafter, a multi-date analysis has been performed. We use all the interpretations at different dates in order to assess the manual interpretation. Indeed, repetitive slicks are more likely due to leaks from static sources: a geological feature for oil seeps, a platform or pipeline for oil spills, for instance. To perform and validate our analysis, the manual detection output has been integrated within a GIS with several data (geological data, marine traffic, oil platforms, oil and gas fields, wind fields, bathymetry, etc.). This work let to the constitution of a dataset with 3903 interpreted oil slicks.

III. Results and analysis

A. Wind influence

The assessment of the influence of the wind speed on the detectability of oil slicks consists of calculating the probability to detect an oil slick for a given wind speed. To do this, as a first step we calculated the wind speed probability of the 3903 observed oil slicks for all four areas of interest (section a). The second step was to calculate the wind speed distribution (probability of occurrence of wind speed) in all areas of interest (b). The last step was to calculate the probability to detect an oil slick for a given wind speed (c) as the normalized ratio of the two above probabilities.

a. Wind speed probability of observed oil slicks: $p(W_i/S)$

Using the ECMWF wind speed model, we got the wind speed of each of the 3903 observed oil slicks all AOI's Therefore, the distribution of wind speed (W_i) of 3903 observed oil slicks (S) is a conditional probability and is noted as $p(W_i/S)$. In other words, $p(W_i/S)$ is the frequency of the occurrences of wind speed of the 3903 observed oil slicks within each wind speed. By analyzing the result given in Figure 24 one can see that the detectability of oil slicks in Peru is high for wind speed equal to and higher than 5.5 m/s. And conversely, a lower detectability is observed in Peru for wind speed lower than 5.5 m/s. A low detectability of oil slicks is observed in the Congo/Angola for wind speed lower than 2.5 m/s and higher than 7 m/s. About 20 % of 682 detected oil slicks in the Caspian Sea are observed at wind speed between 4.5 m/s and 5 m/s. The detectability of Santa Barbara's observed oil slicks remains relatively stable at wind speed between 2.5 m/s and 6.5 m/s. The mean wind speed and the standard deviation were calculated for all oil slicks of each AOI. By drawing a Gaussian function with the mean and the standard deviation of observations, one may see that 95% observed oil slicks in Peru, Congo/Angola, Caspian Sea, and Santa Barbara range respectively between 2.43 - 8.55 m/s, 2.30 - 7.50 m/s, 1.64 - 8.20 m/s, and 1.03 - 8.23 m/s (see Table 4).

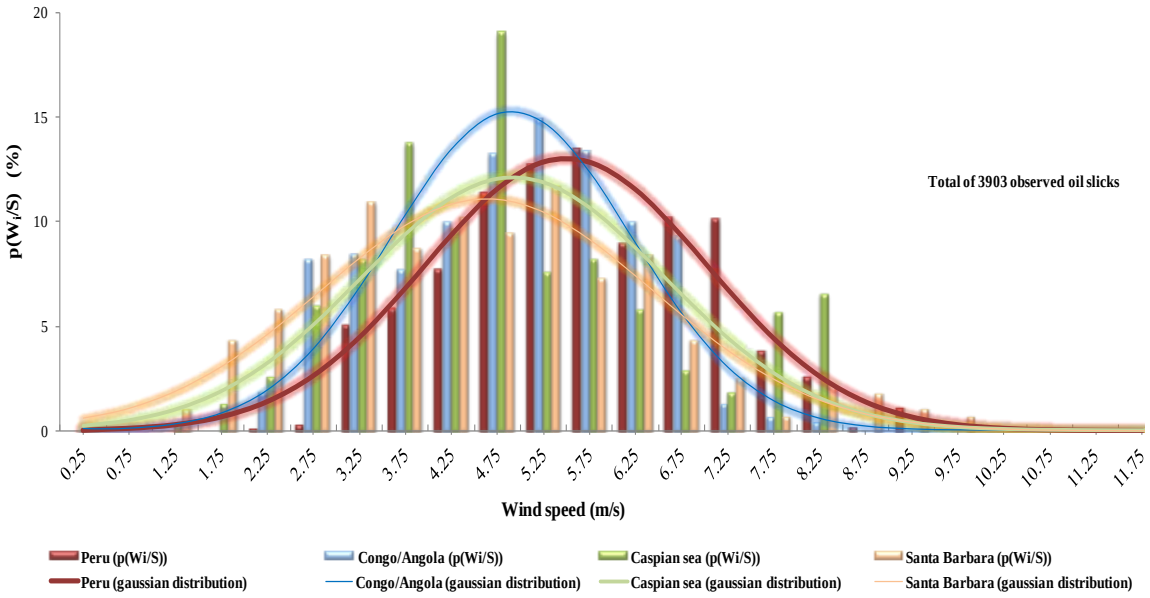

Figure 24. Wind speed distribution obtained from ECMWF of observed oil slicks ($p(W_i/S)$) in Peru (red, 2111 samples), Congo/Angola (blue, 836 samples), Caspian Sea (green, 682 samples), and Santa Barbara (orange, 274 samples). One may note the general Gaussian distribution of the wind speed and the 95% confidence of wind distribution range in between 2 and 8m/s.

Table 4 Wind speed statistics obtained from ECMWF: Min, Max, Mean, Standard deviation, and Wind range for all observed oil slicks on each AOI. Wind speed ranges are calculated assuming a Gaussian distribution (95% - Figure 22). So oil slicks are visible from 0,7m/s to 10m/s. The Mean is consistent for Caspian Sea, Congo, and Santa Barbara but higher for Peru probably due to different wind conditions.

AOI	Number of scenes by sensor mode	Number of observed oil slick	Min (m/s)	Max (m/s)	Mean (m/s)	STD V (m/s)	Wind range 95% (m/s)
Peru	53 scenes WSM 46 scenes APP 96 scenes IMP 324 scenes PRI 231 scenes IW	2111	1.1	10	5.49	1.53	2.43 - 8.55
Congo/Angola	244 scenes WSM	836	0.7	8.2	4.90	1.30	2.30 - 7.50
Caspian Sea	180 scenes WSM	682	0.9	8.4	4.92	1.64	1.64 - 8.20
Santa Barbara	159 scenes WSM	274	0.7	9.5	4.63	1.80	1.03 - 8.23

The global wind speed distribution of the 3903 observed oil slicks from all AOI is given in Figure 25. The Pearson correlation coefficient between data (global wind speed distribution) and a Gaussian distribution, calculated as given by Asuero et al. (2006) is high (0,987). Thus, by analyzing the outcome, one may see that 95% of observed oil slicks are detected at wind speed ranging between 2.09 m/s and 8.33 m/s, with a maximal detectability at 4.75 m/s, while the lower and the upper bounds are found to be 0.7 and 10 m/s (Table 4). Above 10 m/s the detection seems practically nonexistent. The few cases with wind speed less than 1 m/s show that oil slicks may be detectible on SAR images beyond the lower bounds reported in the literature (ref. see above).

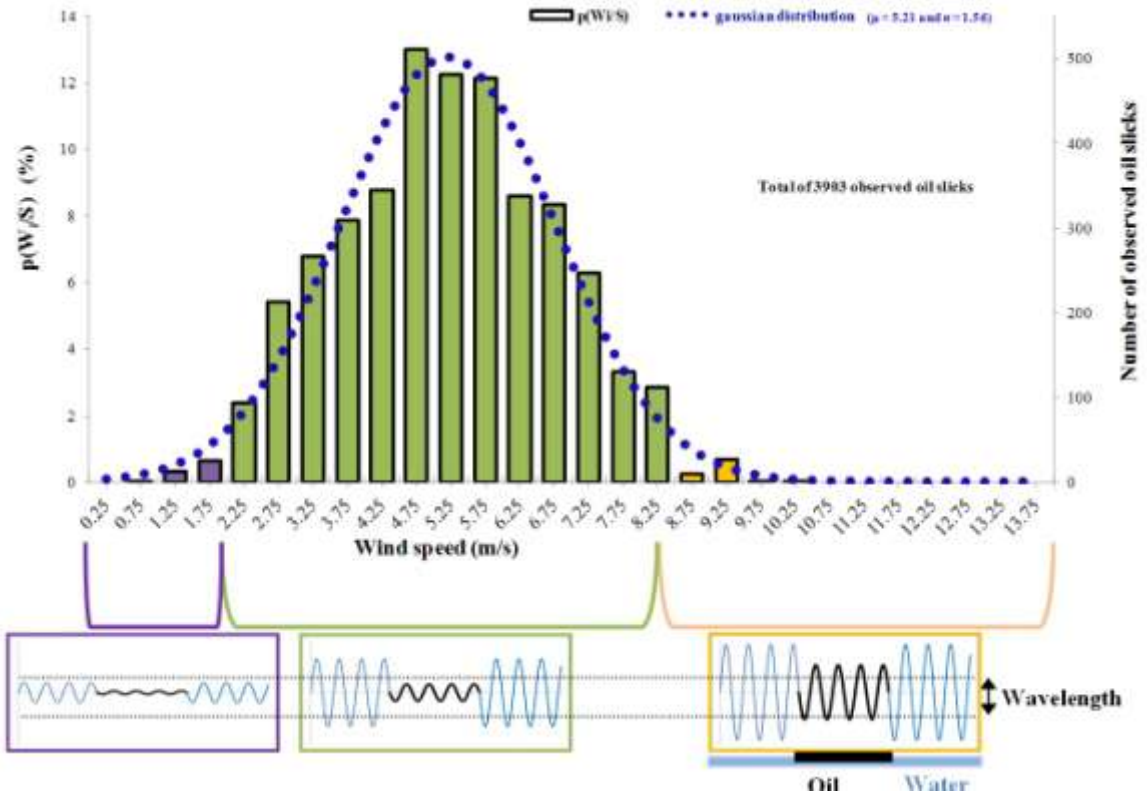

Figure 25. The global wind speed distribution of the 3903 observed oil slicks from all AOI (p(Wi/S)). One can see that 95% of oil slicks have been detected at wind speed ranging between 2.09 m/s and 8.33 m/s. The three rectangles below highlight a vertical section of the sea (water waves = sinusoid in blue) and the oil slick (black sinusoid) for the three different wind ranges. Scarcity of oil slicks below 2.09 m/s and above 8.33 m/s (left and right rectangles), contrasting with the central rectangle corresponding to the optimal wind speed for triggering the Bragg waves without harming the dampening effect of oil. This central green rectangle reflects 95% of confidence to detect oil slicks within a radar image. Mean wind speed (μ) and standard deviation (σ). We herein confirm from a stochastic methodology using a very large panel of radar images the wind range that previous authors already inferred empirically.

b. *Wind speed probability: $p(W_i)$*

Few oil slicks have been observed outside the range 2.09 - 8.33 m/s. This can be due to the fact that few winds are measured outside this range in our dataset. To asses this eventuality, we calculated the wind speed of each location where an oil slick is observed at the date of observation and at the rest of the dates of our SAR dataset that cover this location. This wind speed distribution is the probability of occurrence of wind speed and is noted as $p(W_i)$. The $p(W_i)$ has been calculated per AOI and later for all AOI's where a total of 609220 wind speed occurrences are plotted. The goal here, is to decorrelate (i) the probability to detect an oil slick according to a given wind speed from (ii) the probability of occurrence of this wind speed. The outcome is given in Figure 26. The results are given by AOI in order to differentiate the wind behavior of different geographic, geologic zones. Moreover we added all AOI's results in order to get the global AOI's wind speed distribution. In detail, Peru mean wind speed (4.89 m/s) is higher than that of the other AOI (Caspian Sea: 4.13 m/s, Congo/Angola: 3.28 m/s, and Santa Barbara: 3.21 m/s). The mean wind speed of the total distribution of the four zones is around 4.26 m/s.

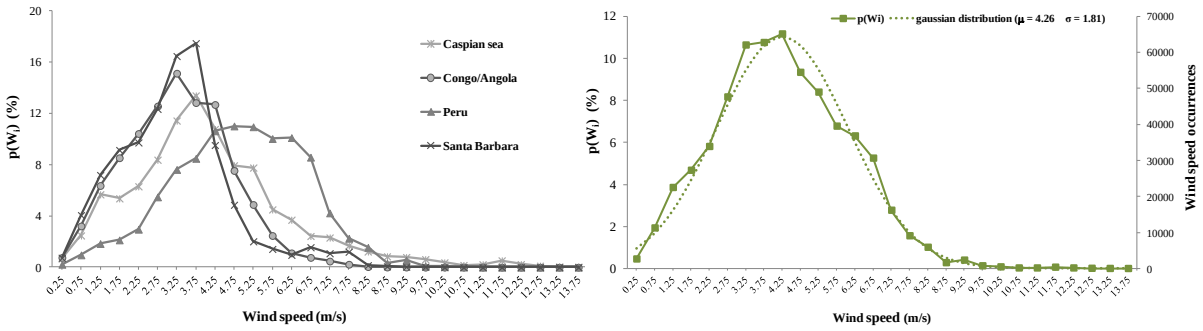

Figure 26. The wind speed probability (p(Wi)) for each AOI (curves in grey - left panel). The right panel corresponds to the total distribution of the wind speed of the four AOI. The green curve corresponds to the analyses of 609220 wind speed occurrences. (μ): Mean wind speed, (σ): standard deviation. In Peru area one may note the higher occurrence of high wind values than last 3 AOI which have coarsely the same wind speed ranges.

c. *Probability to detect an oil slick for a given wind speed: p(S/Wi)*

The scope of this section is to calculate the probability to detect an oil slick for a given wind speed. This probability can be mathematically presented as a conditional probability noted as $p(S/W_i)$. As given by Equation 8, $p(S/W_i)$ is calculated using (i) the probability of occurrence of the wind speed in all locations where an oil slick has been observed $p(W_i/S)$ (Figure 25), (ii) the probability of occurrence of the wind speed in all acquisitions, in all locations where an oil slick has been observed in at least one acquisition $p(W_i)$ (Figure 26, right panel), and (iii) the probability for an oil slick to

occur on the sea surface. Without any prior knowledge, *Ps* can be considered as constant for a given AOI.

$$p(S/W_i) = P_s * \frac{p(W_i/S)}{p(W_i)} \qquad \text{(Equation 8)}$$

Where:

$p(S/W_i)$ is the probability to detect an oil slick S for a given wind speed W_i,

P_s is the probability for an oil slick to occur on the sea surface in a given AOI. Without any prior knowledge, *Ps* can be considered as constant for a given AOI,

$p(W_i/S)$ is the probability of occurrence of the wind speed W_i in all locations in the single acquisition where an oil slick has been observed,

$p(W_i)$ is the probability of occurrence of the wind speed W_i in all acquisitions, in all locations where an oil slick has been observed in at least one acquisition (609220 occurrences).

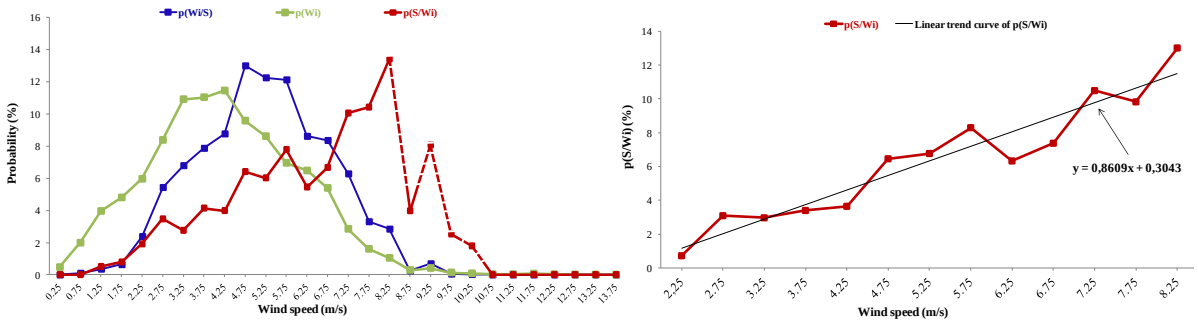

Figure 27. Probability to detect an oil slick on the sea surface (red curve). The blue curve - p(Wi/S)- (left panel) corresponds to the wind speed distribution obtained from ECMWF model on all observed oil slicks (total 3903 studied samples – same as Figure 25); The green curve is the wind speed distribution in all location where a minimum of one oil slick is observed on all the SAR image dataset (total 609.220 studied samples same as Figure 26 right panel); Consequently, the red curve corresponds to the probability- p(S/Wi)- to detect an oil slick for a given wind intensity. It is the decorrelation in between the blue and the green curves as it is calculated from the ratio of p(Wi/S): p(S/Wi). (Equation 1). The dashed part of the red curve is not here taken into consideration because of the low number of oil slicks samples analyzed with strong winds. For the first time, contrasting to previous studies, the red curve prove that the probability to detect an oil slick arises almost linearly with the increase of the wind speed as we observe that the maximum probability is reached at 8.25m/s !

Figure 27 (left panel) shows *p(S/Wi)* (red curve), *p(Wi/S)* (blue curve), and *p(Wi)* (green curve). The analysis of the outcome shows that the probability to detect an oil slick (red curve) increases with the increase of the wind speed. A maximum probability is reached at 8.25 m/s. above 8.25 m/s, the red curve is in dashed part of the *p(S/Wi)* curve and not taken into consideration because of the low number of oil slicks samples. Figure 27 (right panel) shows *p(S/Wi)* (red curve) and its linear trend curve (black curve) for the optimal wind speed for the detectability of oil slicks, previously defined (2.09 - 8.33 m/s). One can see that the detectability of oil slicks arises almost linearly with the increase of the wind speed. Indeed, *p(S/Wi)* is well correlated to the linear trend curve (0.953) for wind speed ranging between 2.09 m/s and 8.33 m/s. This finding is important since it contrast with what is known hitherto (Gade and Viebahn, 2000; Bayramov et al., 2015).

B. Instrument mode influence

Below we now want to assess the influence of SAR instruments on oil slicks detectability and then to assess this influence under different wind speed with oil slicks detectability. As it's well known that the detection of marine oil slicks on SAR imagery depends on environment conditions (wind, waves, currents, tides, etc.) as well as radar system parameters (frequency, spatial resolution, polarization, incident angle, etc.) (Gades and Alpers, 1998; Trivero et al., 1998). In order to assess the instrument influence a normalized frequency of oil slicks S_f is calculated as:

$$Sf = \frac{Sn}{Op * GSD} \qquad \text{(Equation 9)}$$

Where:

S_f is the normalized frequency of observed oil slicks

S_n is the total number of observed oil slicks

GSD is the pixel spacing also called the Ground Sampling Distance (GSD). It's the distance between adjacent pixels in an image, measured in meters.

O_p is the total number observed pixels defined by the equation below:

$$Op = \sum_{l=0}^{M-1}\sum_{p=0}^{N-1} Oc\ (l, p) \qquad \text{(Equation 3)}$$

Where:

$O_c(l,p)$ is the number of scenes (observed at different dates) which pixel(s) fall at (l,p) location.

The normalized frequency of oil slicks has been computed for five types of products (PRI, APP, IMP, WSM, and IW). The result (Figure 28) demonstrate that the performance of oil slicks detectability depends on the acquisition modes in the following decreasing order IW, APP, PRI, IMP, and WSM. By analyzing the Figure 28 (left panel) one can see that the established order seems to be highly correlated with the pixel spacing. In order to characterize this correlation, the normalized frequency of observed oil slicks is calculated according to the pixel spacing (10 m, 12.5 m, and 75 m). The results given in Figure 28 (right panel), show that about 55% of interpreted oil slicks are observed with a pixel spacing of 10 m (IW), 38% with a pixel spacing of 12.5 m (IMP, PRI, and APP), and only 7% with a pixel spacing of 75 m pixel spacing (WSM). This may be explained by the fact that the oil slicks smaller than the spatial resolution of the WSM mode are not detected.

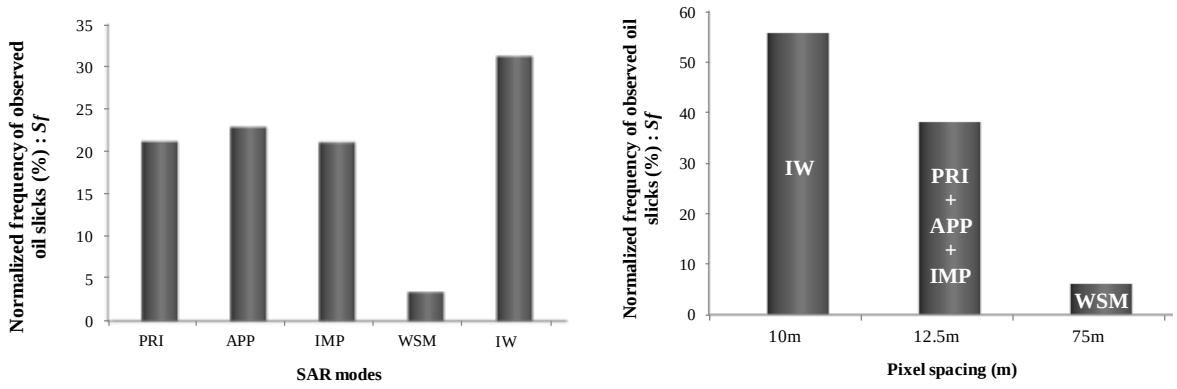

Figure 28. Normalized frequency of observed oil slicks according to the radar acquisition mode (left panel) and the pixel spacing (right panel). One may notice that IW, APP, IMP, and PRI acquisition modes are more powerful than WSM mode on oil slicks detection because of the higher spatial resolution. It shows that the smaller pixel spacing is, the better the detectability of oil slick is. Remember that small slicks are not detected by WSM mode.

Another explanation is that under high wind speed, oil slicks tend to breakup and may be undetectable by the low pixel spacing WSM. In order to check the influence of the sensor mode under different winds speed, we plotted the normalized frequency of observed oil slicks of the 5 sensors mode according to wind speed. The analysis of the result given on Figure 7 shows that under high winds speed, the normalized frequency of observed oil slicks is the higher for IW mode. So despite the few number of oil slicks observed under strong wind speed, these slicks are detected mainly by sensors with the higher spatial resolution (IW). By intersecting these results with the earlier ones (Figure 4 and Figure 5), one concludes that the high probability to detect an oil slick (p(S/Wi) under high winds speed is due to both the higher amount and pixel spacing of IW, APP, IMP, and PRI scenes on the AOI where the wind is the strongest.

Another explanation is that under high wind speed, oil slicks tend to breakup and may be undetectable by the low pixel spacing WSM. In order to check the influence of the sensor mode under different winds speed, we plotted the normalized frequency of observed oil slicks of the 5 sensors mode according to wind speed. The analysis of the result given on Figure 29 shows that under high winds speed, the normalized frequency of observed oil slicks is the higher for IW mode. So despite the few number of oil slicks observed under strong wind speed, these slicks are detected mainly by sensors with the higher spatial resolution (IW). By intersecting these results with the earlier ones (Figure 25 and Figure 26), one concludes that the high probability to detect an oil slick (p(S/Wi) under high winds speed is due to both the higher pixel spacing and amount of IW, APP, IMP, and PRI scenes on the AOI where the wind is the strongest.

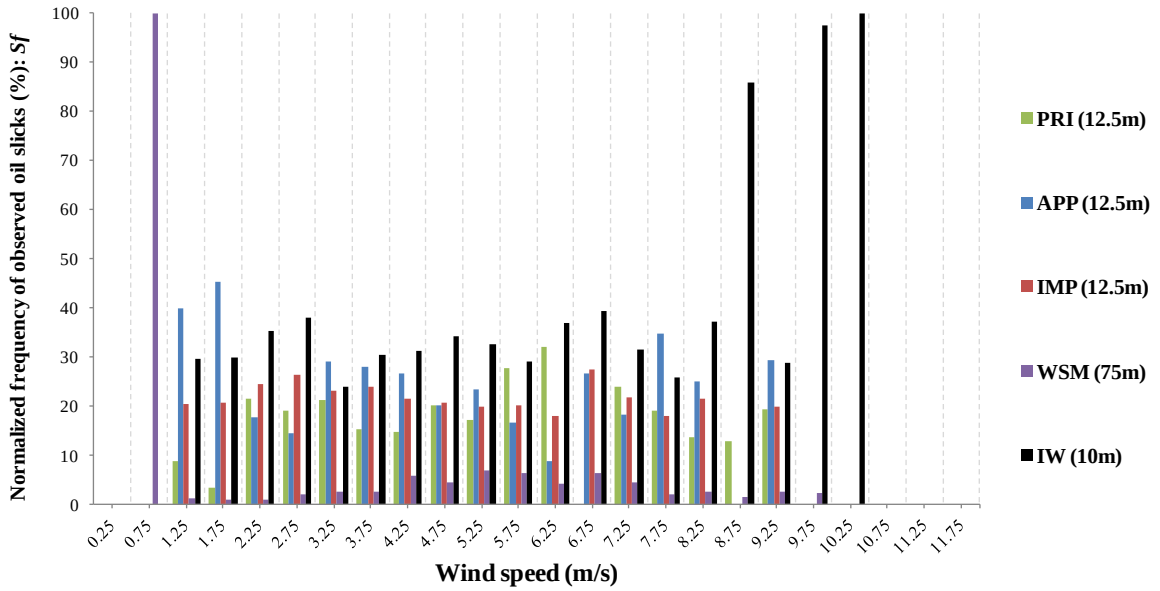

Figure 29. Normalized frequency of observed oil slicks Sf by radar sensor mode according to the wind speed. One may note that all sensor modes present the same response within 1 m/s up to 9 m/s. For the higher wind range only the small spacing resolution sentinel IW sensor mode succeed to reveal oils slicks. We suggest that this is due to the oil slicks fragmentation probably due to breaking through strong winds. In contrast the high value of WSM in the low wind speed value (less than 1m/s) is biased by the absence of radar images of IW, IMP, APP, PRI modes in the Caspian sea, Congo/Angola and Santa Barbara (see table 3).

IV. Conclusions and perspectives

We are interested, like the numerous previous empiric approaches, in the relations in between the detection of oil slicks from SAR images and wind speeds. But, contrasting with the bibliography, we herein use, for the first time, a stochastic method to assess this relation as it is a very decisive element

in the detection of marine oil slicks. After analyzing 1333 SAR images (1992-2015), acquired by three SAR missions on four areas of interest, we achieved this first result: an optimal detectability of oil slicks is ensured when the wind speed is between 2.09 and 8.33 m/s. Beyond these conditions, ie above 8.33 m/s and below 2.09 m/s, there is little chance (5%) to detect an oil slick. Note that intervals have already been announced like 7-10 m/s (Brekke and Solberg, 2005), 3.5 to 7 m/s (Garcia-Pineda et al., 2009), 1.5-10 m/s (Fingas and Brown, 2014), and 1 to 7°m/s (Marghany, 2014a). Within the same interval, 2.09 and 8.33 m/s, the detectability obviously varies. Contrary to the literature hitherto produced - and this is the second important result - in this interval, the higher the wind speed is the better the detectability is (Figure 27) up to the maximum we register in this work 8.25m/s.

In addition, a performance order of 5 instrument modes is established (IW, APP, PRI, IMP and WSM). The present study shows that the IW mode (Sentinel-1), with the higher spatial resolution of 5x20 m, is to be the most suitable for detecting an oil slick at high wind speed. This may be due to the fact that the slicks break under the influence of strong winds and that only the higher pixel spacing IW is able to detect them.

Our stochastic study improves and quantifies the dependence of marine oil slicks detectability on wind speed and sensing modes on a global scale. With the challenge of BigData and dealing with lots of data, these findings help to optimize the automatic detection of oil slicks. Optimization consists on eliminating false alerts that make ambiguity between slick and areas of low wind. For high wind areas where the detection of slicks is not possible, further process optimization is to minimize the processing time by the non consideration of the very low and high wind speed. We recommend extending this study by taking into account the influence of seasons, more wavelengths, and oil properties. Also, for more accurate wind data we recommend the use of local wind models or a large number of in situ observations using our statistic methodology.

Acknowledgments

This work is performed as a part of a PhD research program funded by VisioTerra/UPE (Université Paris-Est) and ANRT/CIFRE. The authors would like to thank The European Spatial Agency (ESA) for the SAR scenes used in this study, and the ECMWF for wind data.

References

Alpers, Werner, and H. A. Espedal. 2004. "Chapter 11. Oils and Surfactants." In Synthetic Aperture Radar Marine User's Manual, edited by Christopher R Jackson and John. R. Apel, 263–75. Washington, DC: U.S Department of Commerce, National Oceanic and Atmospheric Administration, National Environmental Satellite, Data and Information Service, Office of Research and Applications.

Angiuli, Emanuele, Frate F. D, and Salvatori L.. 2006. "Neural networks for oil spill detection using ERS and ENVISAT imagery." In Proceedings of SeaSAR'06, 23-26 January (2006), Frascati, Italy: 1–6.

Asuero A. G., Sayago A., and A. G. González, 2006. "The Correlation Coefficient: An Overview" Critical Reviews in Analytical Chemistry: 41-59. DOI: 10.1080/10408340500526766.

Bayramov, E. R., Buchroithner, M. F., and Bayramov, R. V., 2015. "Detection of oil pollution hotspots and leak sources through the quantitative assessment of the persistence and temporal repetition of regular oil spills in the caspian sea using remote sensing and gis." ISPRS Ann. Photogramm. Remote Sens. Spatial Inf. Sci., II-3/W5:451-457. doi:10.5194/isprsannals-II-3-W5-451-2015, 2015.

Brekke C. and A.h.S. Solberg. 2005. "Oil Spill Detection by Satellite Remote Sensing." Remote Sensing of Environment 95 (2005): 1-13.

Buchroithner, M. F. 2001. "A decade of trans-European remote sensing cooperation." Balkema, Rotterdam ISBN 90 5809 1872 (2001): 131-135.

Chang, Lena, Z. S. Tang, S. H. Chang, and Yang-Lang Chang. 2008. "A region-based GLRT detection of oil spills in SAR Images." Pattern Recognition Letters 29 (14): 1915–23. doi:10.1016/j.patrec.2008.05.022.

Dee, D. P., and 35 co-authors. 2011. "The ERA-Interim reanalysis: Configuration and performance of the data assimilation system". Quart. J. R. Meteorol 137 (2011) 553-597. DOI: 10.1002/qj.828.

Del Frate, Fabio, A. Petrocchi, J. Lichtenegger, and G. Calabresi. 2000. "Neural networks for oil spill detection using ERS-SAR data." IEEE Transactions on Geoscience and Remote Sensing 38 (5): 2282–87. doi:10.1109/36.868885.

Del Frate, Fabio, D. Latini, C. Pratola, and F. Palazzo. 2013. "PCNN for automatic segmentation and information extraction from X-band SAR imagery." International Journal of Image and Data Fusion 4 (1): 75–88. doi:10.1080/19479832.2012.713398.

Elachi C.. 1988. "Spaceborne Radar Remote Sensing: Applications and Techniques." IEEE press, ISBN 0879422416 (1988), : 288.

Espedal H. A.. 1999. "Satellite SAR oil spill detection using wind history information." International Journal of Remote Sensing 20(1999): 49-65.

European Space Agency Web-site. 2016. http://www.esa.int/Our_Activities/Observing_the_Earth/Copernicus/SAR_missions, accessed 29 June 2016.

Fingas, M. And Brown C.. 2014."A review of oil spill remote sensing." Marine Pollution Bulletin 83 (2014): 9–23.

Fiscella, B., A. Giancaspro, F. Nirchio, P. Pavese, and P. Trivero. 2000. "Oil spill detection using marine SAR images." International Journal of Remote Sensing 21 (18): 3561–66. doi:10.1080/014311600750037589.

Fortuny-Guasch J.. 2003. "Improved oil spill detection and classification with polarimetric SAR." Proc. workshop on Application of SAR Polarimery and Polarimetric Interferometry, ESA-ESRIN Frascati, Italy (2003): 14–16.

Gade M. and Alpers W.. 1998. "Imaging of biogenic and anthropogenic ocean surface films by the multifrequency/multipolarization SIR-C/X-SAR." Journal of Geophysical Research 103 (1998):18,851-18,866.

Gade M. and von Viebahn C., 2000. "Oil spill data from the Baltic Sea obtained by spaceborne SAR and airborne multisensors." Proc. EARSeL Dresden, Germany, Rotterdam; Balekma: 14-16

Gade M.; Alpers W..1999. "Using ERS-2 SAR images for routine observation of marine pollution in European coastal waters." The Science of The Total Environment (1999): 441-448.

Garcia-Pineda, Oscar, I. R. MacDonald, and B. Zimmer. 2008. "Synthetic Aperture Radar image processing using the supervised Textural-Neural Network Classification Algorithm." In IGARSS 2008 - 2008 IEEE International Geoscience and Remote Sensing Symposium, IV – 1265–IV – 1268. IEEE. doi:10.1109/IGARSS.2008.4779960.

Garcia-Pineda, Zimmer B., Howard M., Pichel W., Li X., MacDonald R.. 2009. "Using SAR images to delineate ocean oil slicks with a texture-classifying neural network algorithm (TCNNA).", Canadien Journal Remote Sensing 35(2009):411-421.

Gasull, A., X. Fábregas, J. Jiménez, F. Marqués, V. Moreno, and M. A. Herrero. 2002. "Oil spills detection in SAR images using mathematical morphology." In 11th European Signal Processing Conference (EUSIPCO 2002), 25–28. Toulouse, France. doi:10.1.1.81.3086.

GESAMP (IMO/FAO/UNESCO IOC/UNIDO/WMO/IAEA/UN/UNEP Joint Group of Experts on the Scientific Aspects of Marine Environmental Protection). 2007. "Estimates of oil entering the marine environment from sea-based activities." Rep. Stud. GESAMP No. 75 (2007):96.

Jackson C. R. and Apel J. R.. 2004. "Synthetic Aperture Radar marine user's manual." Edited by John. R. Apel and Christopher R Jackson. Washington, DC: U.S department of commerce, National Oceanic and Atmospheric Administration (NOAA), National Environmental Satellite, Data and Information Service, Office of Research and Applications.

Kanaa, T. F. N., E. Tonye, G .Mercier, V. P. Onana, J. M. Ngono, P. L . Frison, J. P. Rudant, and R. Garello. 2003. "Detection of oil slick signatures in SAR images by fusion of hysteresis thresholding responses." In IGARSS 2003. 2003 IEEE International Geoscience and Remote Sensing Symposium. Proceedings (IEEE Cat. No.03CH37477), 4:2750–52. IEEE. doi:10.1109/IGARSS.2003.1294573.

Liu, A. K., C. Y. Peng, and S. Y. Chang. 1997. "Wavelet analysis of satellite images for coastal watch." IEEE Journal on Ocean Engineering 22 (1): 9–17.

Marghany Maged. 2001. "RADARSAT automatic algorithms for detecting coastal oil spill pollution." International Journal of Applied Earth Observation and Geoinformation 3.2 (2001): 191-196.

Marghany Maged. 2014. "Multi-Objective Evolutionary Algorithm for Oil Spill Detection from COSMO-SkeyMed Satellite." Computational Science and Its Applications-ICCSA 2014. Springer International Publishing, (2014): 355-371.

Marghany Maged. 2014a. "Utilization of a genetic algorithm for the automatic detection of oil spill from RADARSAT-2 SAR satellite data." Marine pollution bulletin 89.1 (2014): 20-29.

Marghany Maged. 2015. "Automatic detection of oil spills in the Gulf of Mexico from RADARSAT-2 SAR satellite data." Environmental Earth Sciences 74.7 (2015): 5935-5947.

Mercier G.; Girard-Ardhuin F.. 2006. "Partially Supervised Oil Slick Detection by SAR I magery using Kernel Expansion.", IEEE-TGRS44 (2006):2839-2846.

Robinson, I. S.. 1994. "Satellite oceanography. An introduction for oceanographers and remote-sensing scientists." Wiley–Praxis series in remote sensing (1994): 455.

Shu Y.; Li J.; Yousif H. and Gomes G.. 2010. "Dark-spot detection from SAR intensity imagery with spatial density thresholding for oil-spill monitoring." Remote Sensing of Environment 114 (2010): 2026 - 2035.

Skrunes S.; Brekke C.; Eltoft T.. 2012. "Oil spill characterization with multi-polarization C- and X-band SAR." Geoscience and Remote Sensing Symposium (IGARSS), IEEE International5117 (2012):22-27.

Solberg, A. H. S., G. Storvik, R. Solberg, and E. Volden. 1999. "Automatic detection of oil spills in ERS SAR images." IEEE Transactions on Geoscience and Remote Sensing 37 (4): 1916–24. doi:10.1109/36.774704.

Suresh, Gopika, C. Melsheimer, J.-H. Körber, and G. Bohrmann. 2015. "Automatic estimation of oil seep locations in Synthetic Aperture Radar images." IEEE Transactions on Geoscience and Remote Sensing 53 (8): 4218 – 4230. doi: 10.1109/TGRS.2015.2393375.

Topouzelis K.. 2008. "Oil spill detection by SAR images: Dark Formation Detection, Feature Extraction and Classification Algorithms." Sensor Journal (8): 6642-6659.

Trivero P.; Fiscella B.; Gomez F.; Pavese P.. 1998. "SAR detection and characterization of sea surface slicks." International Journal of Remote Sensing 19 (1998): 543-548.

Xu L.; Li J. and Brenning A.. 2014. "A comparative study of different classification techniques for marine oil spill identification using RADARSAT-1 imagery." Remote Sensing of Environment141 (2014): 14-23.

Xu L.; Shafiee M. J.; Wong A.; Li F.; Wang L.; and Clausi D. A. 2015. "Oil spill candidate detection from SAR imagery using a thresholding-guided stochastic fully-connected conditional random field model." CVPR (2015): 86.

3.3 Conclusion du chapitre

Le RSO est l'outil spatial le plus approprié pour surveiller les nappes d'huile marines en raison de sa large couverture, de son indépendance par rapport aux conditions météorologiques et de l'éclairage solaire. La détection des nappes d'hydrocarbures devient difficile dans certaines conditions de vent. Cet article fournit une étude statistique pour améliorer et quantifier la dépendance de la détection des nappes de pétrole de la vitesse du vent et les modes d'acquisition radar en utilisant le modèle de vent ECMWF à l'échelle mondiale. Nous avons utilisé 1333 images radar (1992-2015) acquises par trois missions radar sur quatre domaines d'intérêt. Nous prouvons ici qu'une détectabilité optimale est assurée lorsque la vitesse du vent est comprise entre 2.09 m/s and 8.33 m/s. Au-delà de ces conditions, c'est-à-dire au-dessus de 8.33 m/s et au-dessous de 2.09 m/s, il ya peu de chance (5%) de détecter une nappe d'huile. De plus, un ordre de performance de 5 modes de capteur est établi. Le mode IW (Sentinel-1) avec une résolution spatiale de 5x20 m semble être le plus appropriée pour détecter une nappe d'huile à de fortes vitesses de vent. Ces résultats peuvent aider à optimiser la détection automatique des nappes d'huile. En effet, avec le défi des grandes données, nous devrons traiter beaucoup de données. L'optimisation consiste à éliminer les fausses alertes qui font de l'ambiguïté entre la nappe d'huile et les zones à faible vent. Pour les zones de fortes vitesses de vent où la détection des nappes n'est pas possible, l'optimisation est de minimiser le temps de traitement par la non prise en compte de ces dernières. Nous recommandons d'étendre cette étude en tenant compte de l'influence des saisons, des longueurs d'onde et des propriétés de l'huile.

Chapitre 4 Modèle de dérive verticale

Résumé du chapitre

Les réservoirs pétroliers sont caractérisés par la présence d'indices d'huile en surface. Ces indices sont activement recherchés par les pétroliers à des fins d'exploitation en mer (offshore). Sur mer ces indices (nappes d'hydrocarbures) sont détectables par l'utilisation des différences de rugosités locales multidates du signal d'amplitude de l'imagerie radar. Les manifestations de suintements d'hydrocarbures sur la surface de la mer ("*Sea Surface Outbreak*", SSO) sont généralement décalées de leur sources sur les fonds marins ("*Sea Floor Source*", SFS) de plusieurs centaines de mètres ou même de kilomètres. Ce déplacement est fonction de la vitesse ascensionnelle et des courants marins le long de la colonne d'eau. L'article qui fait objet de ce chapitre propose un modèle de dérive verticale ("*Vertical Drift Model*", VDM) qui combine des images radar et un modèle hydrodynamique (HYCOM). Après la détection des nappes d'huile à partir des images radar, le VDM procède à une régression dans le temps et l'espace basée sur la vitesse ascensionnelle de l'huile (loi de Stokes) et les conditions hydrodynamiques (HYCOM) pour trouver l'emplacement de la source de fuite sur le fond marin. La vitesse ascensionnelle dépend fortement de la taille des gouttelettes qui est inconnue. Dans le cadre de ce travail, nous proposons une nouvelle méthode appelée «chemins des sources» qui permet d'estimer les sources des nappes d'hydrocarbures sur le fond marin sans connaître a priori la taille des gouttelettes d'huile en trouvant, pour chaque nappe, les SFS correspondants à différents diamètres. Nous appelons chemins sources la ligne qui rejoint les SFS pour une fuite d'huile. Les SFS finaux devraient être à l'intersection des chemins des sources. La méthodologie a été appliquée dans le Golfe du Mexique où l'on connaît l'emplacement de nombreux sites d'hydrocarbures prolifiques.

4.1 Introduction du chapitre

L'exploration offshore a fourni près de 70% des principales découvertes de pétrole et de gaz dans le monde au cours de la dernière décennie (Sandrea et Sansdrea, 2010). Mais avant tout forage O & G, il est nécessaire d'effectuer une véritable préparation détaillée qui mette en œuvre des techniques géologiques et géophysiques complexes et coûteuses, quelle que soit la teneur en O & G du bassin. Cette préparation peut être optimisée en termes de coût, de temps et d'espace en utilisant des images RSO qui demeure cependant insuffisante : la localisation des points sources sur les planchers océaniques reste un complément indispensable de la préparation.

En effet, les nappes d'hydrocarbures marines provenant de suintements d'huile naturelle, appelés aussi hydrocarbures, sont l'extrusion d'hydrocarbures qui se produit sur les zones extracôtières. Ils sont visibles sur la surface de la mer parce que le rapport de densité entre l'huile et l'eau permet à l'huile de flotter à la surface de l'eau. La manifestation de ces effusions est due à la présence de systèmes pétroliers dont la couverture est soit absente (migration directe vers la surface), soit de mauvaise qualité altérée par des structures permettant une migration secondaire à travers elle. Ces expulsions sont facilement observables sur la surface marine.

Les images radar sont utilisées pour se concentrer sur la détection des nappes d'hydrocarbures marins uniquement sur la surface de la mer. Cependant, à des fins d'exploration, il est essentiel d'estimer l'origine de la fuite sur le fond marin. Selon le système hydrodynamique et la vitesse ascendante de l'huile, la distance entre les positions de l'éclosion en surface de la mer (SSO) et de la source sur le fond marin (SFS) d'une fuite d'huile peut varier entre cent et mille mètres (Macdonald et al. 2002) dans le golfe du Mexique, ce qui contraste considérablement avec plus de 50 kilomètres prédits par Mano et al., (2016) sur la même zone d'étude. Une telle variation de dérive suggère des variations importantes de la taille des gouttelettes d'huile et des conditions hydrodynamiques de la colonne d'eau de mer. Pour évaluer cette variabilité, notre étude développe un modèle inverse de la dérive verticale des suintements d'hydrocarbures naturels observés sur les images radar en combinant des images RSO et le modèle océanique HYCOM (HYbrid Coordinate Ocean Model) dans le Golfe du Mexique.

Le modèle vertical trace la trajectoire d'une goutte d'huile d'un diamètre donné (d) à partir de la nappe d'huile en surface de la mer identifiée à distance à partir des images RSO à la source sur fond marin. Le modèle est basé sur une régression dans le temps et l'espace à travers la colonne d'eau. La distance horizontale entre le point d''éclosion en la surface de la mer et la source sur fond marin est appelée «dérive». Pour surmonter la question du diamètre des gouttelettes d'huile (qui est inconnu), la méthode novatrice de «chemin des sources» a été développée et appliquée à la zone d'étude. Pour évaluer l'efficacité du modèle vertical et valider ses résultats, une corrélation avec les données géologiques disponibles a été établie.

4.2 Manuscrit 3: Estimated location of the seafloor sources of marine natural oil seeps? Inputs of a new vertical drift model applied to the Gulf of Mexico

Zhour Najoui [a,b], Serge Riazanoff [b,c], Benoit Deffontaines [a], Jean-Paul Xavier [b]

[a]Laboratoire de REcherche en Géodésie, LAREG, Université Paris-Est Marne-La-Vallée , et Institut Géographique National, France, zhour.najoui@univ-paris-est.fr, benoit.deffontaines@univ-mlv.fr.

[b]VisioTerra, 14 rue Albert Einstein Champs-sur-Marne, France, zhour.najoui@visioterra.fr, serge.riazanoff@visioterra.fr, jean paul.xavier@visioterra.fr.

cUniversité Paris-Est Marne-La-Vallée UPEM – Institut Gaspard Monge -IGM, 5 boulevard Descartes, Champs sur Marne, serge.riazanoff@univ-mlv.fr.

Abstract

Marine oil reservoirs are generally characterized on the sea surface by the presence of natural oil seeps (Sea Surface outbreaks - hereafter SSO). The latter are easily evidenced with Synthetic Aperture Radar (SAR) images because of the dampening effect that oil has on the capillary and associated small gravity waves (Bragg waves). The sea surface outbreaks of oil seeps are offset from their source on the seabed (seafloor sources - SFS) by hundreds meters or even kilometres. This displacement all along the sea water column is a function of the upward velocity of the oil droplet size, and the presence of lateral marine currents. This paper proposes a Vertical Drift Model (VDM) that combines both SAR images to get the SSO and the hydrodynamic model (HYCOM) function of the oil droplet size to estimate the SFS. After oil seeps detection from SAR images, the VDM proceeds to a regression in time and space based on the upward velocity of the oil, based on Stokes law, and the hydrodynamic conditions (HYCOM) to estimate the location of the seep source on the seafloor. The upward velocity depends strongly on the unknown droplet size. We propose herein a new VDM method named "sources paths" that allows to estimate the oil seeps sources on the seafloor without a priori knowledge of the oil droplet size by finding, for each oil seep, the seafloor sources corresponding to different diameters. We call "sources path" the line that joins the seafloor sources for an oil seep. The seafloor sources ought to be at the intersection of the maximum sources paths. The methodology has been applied to the northern Gulf of Mexico where the locations of many prolific oil seep sites are well known.

Keywords

Oil seep, SeaSurface Outbreak, SeaFloor Source, SAR image, Stochastic approach, Vertical drift Model, Sources path, Geological validation, N. Gulf of Mexico.

I. Introduction

The offshore exploration provided nearly 70% of the major oil and gas discoveries worldwide in the last decade (Sandrea and Sandrea, 2010). But, before any O&G drilling, it is required a real detail Exploration which implements both complex and expensive geological and geophysical techniques whatever the basin O&G content. Exploration need to be optimized in cost, time and focused in space by using SAR images in order to detect natural oil seeps (also called oil seepages) on the sea surface as they prove the presence of source rock and mature organic matter within the basin. However, the detection on oil seeps on the sea surface remains insufficient: their precise sources locations on the seafloor appear of great interest for any marine E&P.

Indeed, marine natural oil seeps are hydrocarbon extrusions occurring on the oil offshore areas. They are visible on the sea surface because the oil density is lighter than sea water which allows oil to float on the sea surface. Oil extrusion is due to (1) the lack of cap/cover in the petroleum systems which lead to a direct oil migration to the surface, or (2) to its poor quality (altered/weathered and/or fractured by structures) allowing secondary migration through it. These expulsions are easily observable in the marine surface.

SAR images have proven to be a useful tool for oil slicks (from any biogenic and/or mineral origin) mapping due to the dampening effect that oil has on the capillary and small gravity waves, so-called Bragg waves (Jackson and Apel, 2004; Brekke and Solberg, 2005; Mercier and Girard-Ardhuin, 2006; Shu et al., 2010; Xu et al., 2015). In fact, with higher surface tension than water, oil produces a smoother sea surface than an "oil-free sea surface" resulting in decreasing of the radar backscatter, and hence causing dark patches (Jackson and Apel, 2004; Mercier and Girard-Ardhuin, 2006; Shu et al., 2010; Xu et al., 2015). Consequently, oil seeps appear darker compared to the brighter radar backscatter produced by Bragg waves. In addition to oil seeps, many phenomena may appear as dark in SAR images (Najoui et al, submitted A and B). For instance, some natural features are biogenic oil from algae or phytoplankton blooms, upwelling, rain cells, wind shadows, internal waves, current shear zones, etc. Man-made oil pollution (oil spill) from ships, oil rigs or leaking pipelines, also produces dark signatures in SAR images. Non-oil seeps features are termed as oil seeps lookalikes (Espedal, 1999; Brekke and Solberg, 2005; Xu and Brenning, 2014).

Unfortunately SAR images are able to detect marine oil seeps only on the water surface (Sea Surface Outbreak - SSO below). However, for Exploration purposes, it is compulsory to get the precise origin of the seeps on the seafloor (Sea Floor Source - SFS). In the literature, two approaches have been used to locate the seeps SFS: statistical analysis of surface marine oil seeps using SAR images (Dhont et Dubucq, 2016) and a 3D vertical drift model based on an hydrodynamic model (Mano et al., 2016). In this study, a combination of SAR images analysis and a vertical drift model has been adopted.

Note that the distance between the positions of the seasurface outbreak (SSO) and the seafloor source (SFS) of an oil seep depends on the upward velocity and the hydrodynamic system of the sea water column. For instance, in the Gulf of Mexico, the distance between the positions of the SSO and the SFS of an oil seep can ranges between hundred and thousand meters (Macdonald et al., 2002) that contrast considerably with more than 50 kilometers obtained by Mano et al., (2016). Such important SSO/SFS deflection variation suggests high variations in the oil droplet size and the hydrodynamic conditions of the seawater column. To assess this variability, our study develops a vertical drift model (VDM) of natural oil seeps observed on SAR images. The VDM combines SAR images and the oceanic model HYCOM (HYbrid Coordinate Ocean Model) to trace the trajectory of an oil droplet of a given diameter (d) from the sea surface outbreak remotely identified from SAR images to the seafloor source. This VDM is based on a regression in time and space through the column water. To overcome the issue of the oil droplet diameter size the innovative method of "sources path" has been developed and applied to the northern part of the Gulf of Mexico (test area), well known for the locations of many prolific oil seep sites. To assess the effectiveness of the Vertical Drift Model and validate its outputs, a correlation with the available geological data has been established.

This paper is organised as follow. The section II focuses on the migration mechanisms of an oil seep from the sediments to the sea surface. In the section III a description of the tectonic, petroleum and oceanic settings of the study area (N. Gulf of Mexico) is briefly presented. Section V provides a detailed description of the used methodology that we settled in three main steps : (1) detection of oil seeps and their SSO from SAR images; (2) building the vertical drift model (VDM) using the hydrodynamic model HYCOM and the Stokes equations ; and (3) application of the sources paths algorithm. Finally, results and validation are given in section VI before the conclusions and perspectives.

II. Natural oil seeps migration from deep sediments to sea surface

Offshore natural oil seeps are streams of naturally occurring oils that migrate from the sediments below the seafloor and flow through the water column as oil drops, resulting in telltale slicks on the sea surface (Judd & Hovland 2007). Oil seeps come from the decomposition of organic matter (plankton, plants, animals, etc.) accumulated in marine sedimentary basins. The organic matter evolves into oil with time, depending of the basin infilling, the temperature heat flow as well as pressure phenomena. Because of the lower density of oil compared to water, oil migrates to the sea floor surface through the sedimentary stratas. During this migration, the oil may encounter an impermeable layer and thus be trapped below this "rooftop" (called cover-rock or seal), within a porous and permeable strata that becomes the reservoir rock. The couple reservoir-rock/cover-rock forms a so-called "oil trap" structure. The most common oil traps are: structural (anticlines, faults, salt dome) and stratigraphic traps (pichout, lens and unconformity traps - see Figure 30). The poor quality, or lack of a

cover-rock, allows the oil to escape and reach the surface. Faults or fractures provide natural fluid pathways through which oil is released into the water column. Consequently, the detection and the identification of these natural oil seeps at the sea floor helps and guides E&P resources because active oil seeps provide information about source rock type and maturity, location of seafloor sources, resources, and migration pathways.

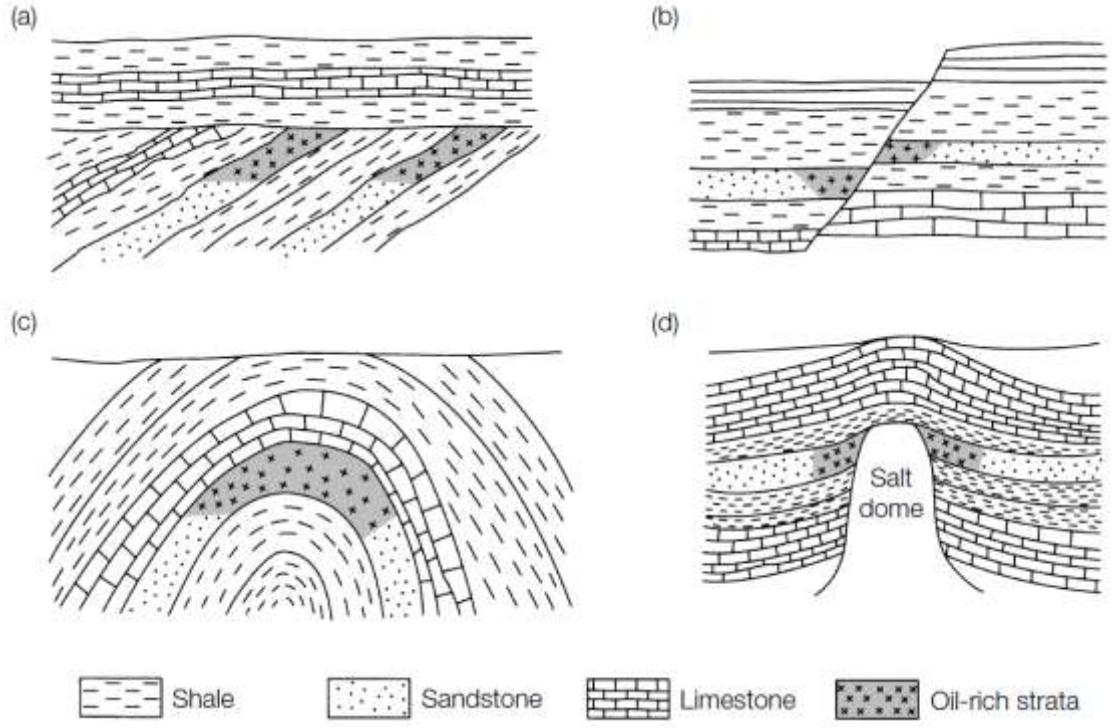

Figure 30. Different possible types of oil traps. a) Stratigraphic trap below an unconformity, b) fault trap c) anticline and d) salt dome (structural trap) (modified from Ross, 1988).

III. Study area

A. Tectonic and petroleum settings

The Gulf of Mexico is a small ocean basin of about 1.5 million square kilometers of arched shape connected eastward to the Atlantic Ocean by the Yucatan Channel and the Straits of Florida. The Gulf of Mexico is geographically surrounded on the north by the South United States of America coast (Texas, Louisiana and Florida) and on the south and the east by Mexico (Yucatan, Campeche, Tabasco, Veracruz, and Tamaulipas). The Gulf of Mexico is characterized by a passive margin that developed through an episode of rifting from the end of Triassic during the Mesozoic breakup of Pangea and specifically due to the separation of the North American and Yucatan plates (Salvador,

1987; Sawyer et al., 1991; Buffler and Thomas, 1994; Jacques and Clegg, 2002; Harry and Londono, 2004). The slow oceanic opening leads to the first salt-bearing deposits characteristic of a shallow depositional environment during the Jurassic (Callovian -Oxfordian ~160Ma). These evaporites are deposited in the shallow basin while the ocean floor is not yet opened (Bird et al, 2005). During Kimmeridgian time, the GOM was submitted to an extensionnal regime that deepens the basin that lead to the setting of oceanic crust and to the end of the evaporitic sedimentation (Buffler and Thomas 1994; Bird et al, 2005). The Oceanic opening which is characterized by a counterclockwise rotation of the Yucatan block divides the salt-bearing deposits into two different set : (1) Louann salts, located on the northernmost part of the Gulf of Mexico and (2) Campeche in the southern part (White, 1980; White and Burke, 1980; Winker and Buffler, 1988; Salvador, 1991; Angeles Aquino et al., 1994; Buffler and Thomas, 1994; Marton and Buffler, 1994; Pindell, 1994; Bird et al, 2005). The Berriasian marks the end of the oceanic rifting and the beginning of an intense salt tectonic activity (Pindell, 1985; Salvador, 1987; Winker and Buffler, 1988; Salvador, 1991; Marton and Buffler, 1994; Bird et al, 2005). It is believed that the salt tectonic is responsible of the creation of the oil traps. Thus, Gulf of Mexico is a province intensely explored by Oil companies and highly oil and gaz producing area.

The Gulf of Mexico has been studied extensively over the past few decades. The evidence of natural hydrocarbon seepage in the continental slope as seen in radar remote sensing images due to oil slicks has been documented and reported earlier by Hood et al. (2002), MacDonald et al. (1993), and Surech (2015). Thermally mature petroleum source rock strata occur in Jurassic, Cretaceous, and Early Cenozoic basinal marls and shales, principally deposited during Eocene, Turonian, and Tithonian–Oxfordian depositional episodes (Hood et al., 2002). Generation phases have extended over several tens of millions of years, depending on source level, burial history, and ambient heat flow. The Gulf petroleum system is a large-scale vertical migration from Mesozoic source rocks into Cenozoic reservoirs (Galloway, 2008).

B. Oceanic settings

The sea currents in the Gulf of Mexico are dominated by mesoscale features that include the Loop Current (LC) and the Loop Current Rings (LCRs), also called eddies (Sturges and Leben, 2000; Zavala-Hidalgo et al., 2003; Smith et al., 2014). The Loop Current forms as the pre-Gulf Stream waters flow from the Caribbean Sea, through the Gulf of Mexico, and on into the Atlantic (Smith et al., 2014 - see Figure 31). When the LC is in an extended northward state, it tends to form and ultimately shed an anticyclonic (clockwise circulation), eddy or LCR that drift to the west, driving the deep circulation just about everywhere in the Gulf (Sturges et al., 2005). LCRs may reach depths of up to ~1000 m and possess swirl speeds of 180–200 $cm.s^{-1}$ (Oey et al., 2005; Smith et al., 2014). Cyclonic (counter-clockwise circulation) frontal eddies are also often found along the edges of the LC and

LCRs. They can have swirl velocities > 100 cm.s^{-1} (Vukovich and Maul, 1985) and can extend to 1000 m at depth (Oey et al., 2005).

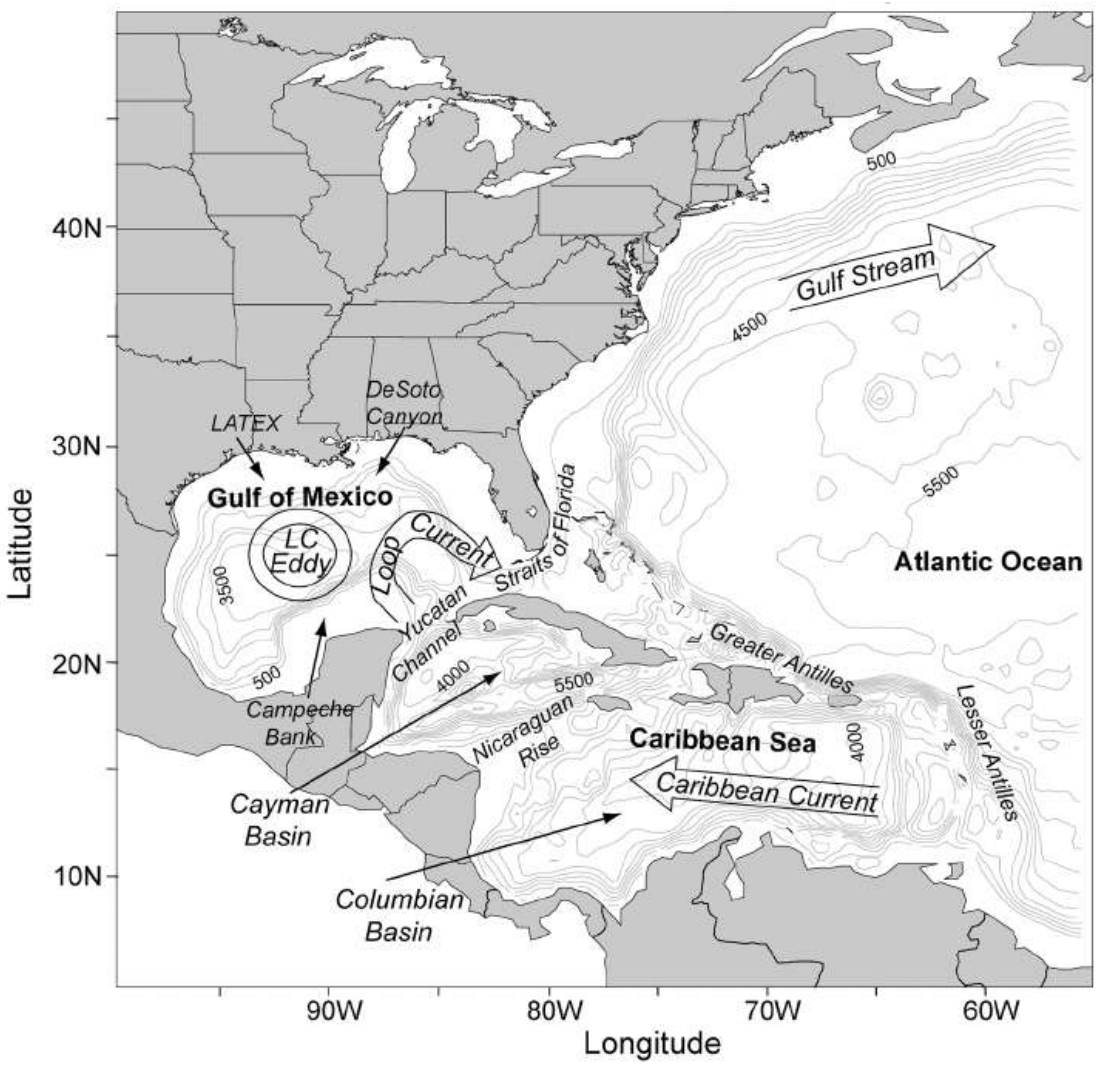

Figure 31. A map for the Gulf of Mexico and the Caribbean Sea with schematic cartoons showing the Caribbean and Loop Currents, Loop Current eddy and the Gulf Stream. The isobaths shown are in meters (from Oey et al., 2005).

V. Methodology

In order to identify and locate the oil seeps sources, we proceeds herein by the three following steps. If the first step is based on the detection of oil seeps from SAR images (see section V-A), the second one focus on the building of a vertical drift model (VDM) that considers two components: the upward velocity of the oil droplet strongly influenced by the diameter of the droplet and the marine currents (section V-B). The last and third step consists in the application of the "source path algorithm" whose role is to locate the seafloor source on the sea floor taking into account the different diameters of the droplets, a priori unknown information (section V-C).

A. Oil seeps detection using SAR images

In the literature, three approaches exist for oil slicks detection from SAR images: (1) a manual approach conducted by trained human operators who analyse individually each SAR images to detect oil slicks (Jatiault et al, 2017), (2) the semi-automatic approach where a computer detects all the dark patches in the SAR image using different techniques of segmentation after which an experienced human operator classifies these objects as oil slicks or look-alikes (Liu et al., 1997 ; Solberg et al., 1999 ; Gasull et al., 2002 ; Kanaa et al., 2003 ; Angiuli et al.,2006 ; Chang et al., 2008 ;Garcia-Pineda et al., 2008 ; Del Frate et al.,2013), and finally (3) the automatic system that uses complicated image processing and programming techniques to perform both segmentation and classification (Solberg et al., 1999 ; Fiscella et al., 2000 ; Del Frate et al, 200; Marghany, 2001 ;Marghany, 2014 ; Marghany, 2015 ;Suresh et al., 2015 ; Mano et al., 2016).

Due to the real unknown accuracy of the semi-automatic and automatic approaches, we focus herein on a reliable manual detection approach even if it is needed to analyse several hundreds of images. In this study a dataset of 215 images (Figure 32) from ENVISAT's ASAR sensor acquired in Wide Swath Mode (WSM) has been used with a temporal coverage of 10 years (2002-2012). Envisat ASAR operates in C-Band (4.20 – 5.75 GHz). The WSM mode gives a 400 km by 400 km wide swath image. Its spatial resolution is approximately 150 m by 150 m with pixel spacing of 75 m by 75 m. ASAR WSM operates according to the ScanSAR principle, using five predetermined overlapping antenna beams which cover the wide swath. The images were provided by the European Spatial Agency (ESA), in digital numbers in a 16 bits format. All images have been georeferenced in the geographic coordinate reference system over the WGS84 ellipsoid, datum WGS84. An accurate land-sea mask has been applied. Thereafter, the images have been radiometrically corrected to ensure uniformity on offshore area by using an adaptation to a backscattering model (Riazanoff and Gross, 2013; Najoui et al., submitted B).

All SAR images have been manually interpreted. The manual detection and recognition of oil seeps are based on the "Synthetic Aperture Radar marine user's manual" (NOAA, 2004). Each of the 215 SAR images has been interpreted independently from the others. Each oil slick has been categorised depending on the interpretation based on morphological and textural criteria (Figure 33).Oil slicks are divided into two major categories: biogenic and mineral. Biogenic oil slicks are produced by plankton and fish substances normally released into the environment. The mineral oils are subdivided into those of natural seeps from the sea bottom or anthropogenic oil spills that originate from ships, refineries, oil terminals, industrial plants, oil platforms, and pipelines (Espedal and Johannessen, 2000). For instance, oil spills from platforms or ships induce significant pitfalls (Johannessen et al., 2000; Trivero and Biamino, 2010; Leifer et al., 2012). If biogenic oils appear as shinny diffracting points on SAR

data, oil seeps are characterized by curvilinear shapes due to short-term changes of the strength and orientation of the wind and of the surface currents (Espedal and Wahl, 1999).

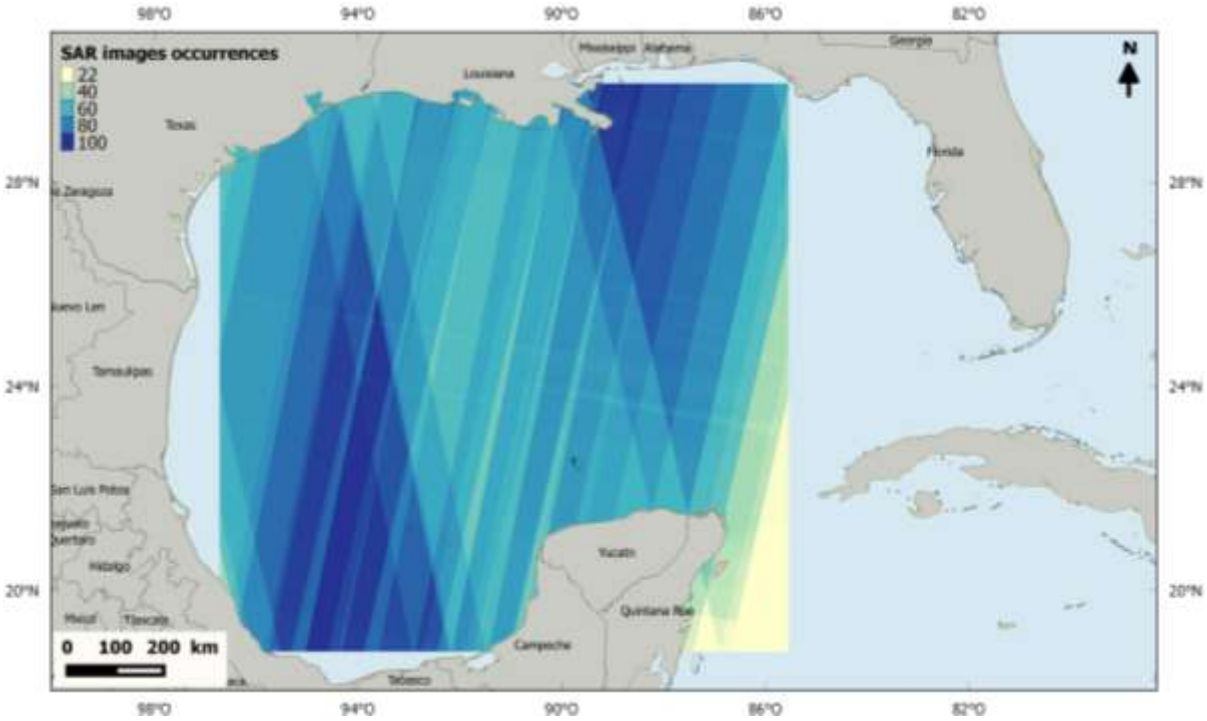

Figure 32. SAR images occurrences map in the Gulf of Mexico.

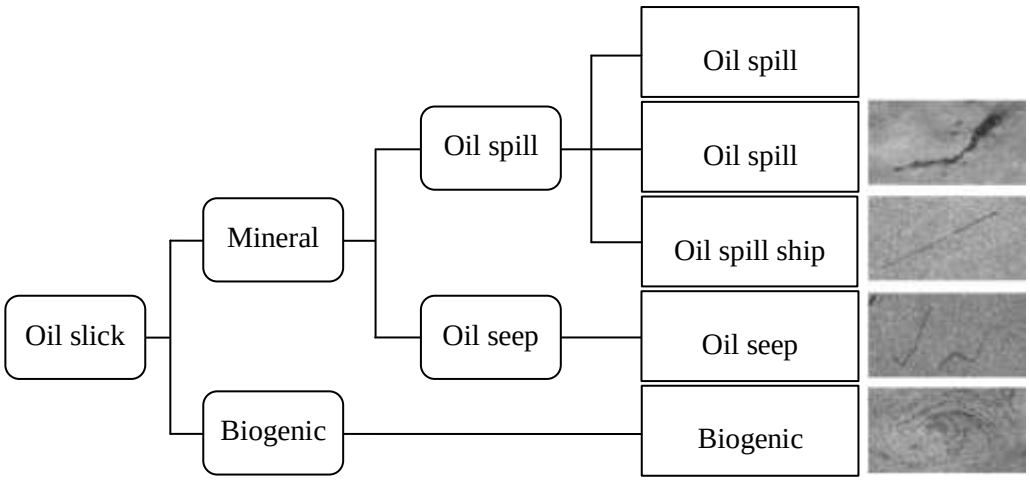

Figure 33. Main offshore oil slicks seen in SAR images.

Thereafter, a multi-date analysis has been performed combining all SAR oil slicks analyses. We use all the interpretations at different dates in order to assess the manual interpretation. Indeed, repetitive slicks are more likely due to leaks from static objects, as a geological pockmark for oil seeps, or a

platform or pipeline for oil spills. To perform and validate this manual classification, the manual detection output has been integrated within a GIS with several data (marine traffic, oil platforms, oil and gas fields, wind fields, bathymetry, etc.). Only high confidence oil slicks from natural oil seeps have been retained and thereafter studied. The oil seeps sea surface outbreaks (SSO herein) correspond to the probable impact area of the fresher oil droplets at the sea surface. The SSO is also called the Oil Slick Origin (OSO, of Garcia-Pineda et al., 2010; Körber et al, 2014; Macdonald et al., 2015). In this study, the term "OSO" has not been used as it is not precise enough to distinguish both Sea Surface Outbreak (SSO) and Sea Floor Source (SFS) which are quite different in location from the sea column point of view.

B. Vertical drift model

Once the SAR images have been analyzed in order to detect manually the different oil seeps, the vertical drift model is built. As explained above, the oil seeps on the sea surface (SSO) are offset from their Sea Floor Sources by their ascending transit within the sea water column of several hundred meters or even kilometers depth. Note that the displacement of an oil droplet within the sea water column is a function of two components: a vertical component representing the upward velocity V_T (also called terminal velocity), and an horizontal component representing the cumulated effect of the marine currents velocity V_c. Assuming a spherical oil droplet dynamic without consider the droplet size variations due to coalescence and dissolution process. V_T can be calculated by the law of Stokes (eq. 10). Factors to consider are the difference in density between water and oil, the viscosity of water (which is a function of temperature, salinity and water density), gravitational acceleration, and diameter of oil droplet (Goncharov, 2009).

$$V_t = \frac{12\mu}{d/2}\left\{\sqrt{\frac{1}{27}\frac{\rho_{water}-\rho_{oil}}{\rho_{water}}\frac{g(d/2)^3}{\mu^2}+1}-1\right\} \qquad \text{(eq. 10)}$$

Where:

V_t is the upward drift,

ρ_{water} is the water density in g/cm^{-3},

ρ_{oil} is the oil density in g/cm^{-3},

μ is the absolute viscosity of water in g/cm^{-3},

g is the gravitational acceleration (9,81 m/s^{-2}),

d is the diameter of the oil droplet in cm.

The temperature, salinity, and current data used come from the HYCOM-GOM (Gulf of Mexico) model. HYCOM is designed as a generalized hybrid (isopycnal/σ/z) coordinate ocean model. It is isopycnal in the open stratified ocean, but reverts to a terrain-following (σ) coordinate in shallow coastal regions, and to z-level coordinates near the surface in the mixed layer. HYCOM-GOM model has 1/25° equatorial resolution and latitudinal resolution of 1/25° cos(lat) or ~3.5 km for each variable at mid-latitudes. The variables are temperature, salinity and currents. The reanalysis data used in this study are interpolated to form a vertical grid of 40 vertical z-level (at constant depth levels) with a temporal resolution of 3 hours.

The vertical drift model traces the trajectory taken by an oil droplet of a given diameter *d* from its surface outbreak remotely defined to its seafloor source (SFS) by going backward in time and space over the whole water column (Figure 34).

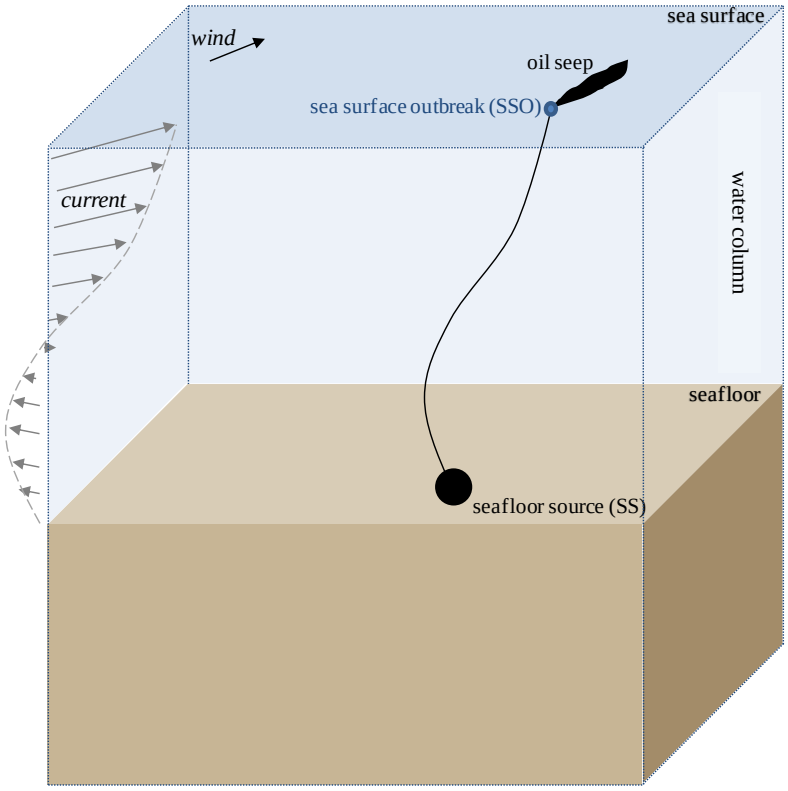

Figure 34. 3D scheme of the vertical drift model of an oil seep remotely detected. Left side: Sea current directions and speeds function of the water column deduced from the HYCOM model for the oil seep sea surface outbreak given date. Black line: represent the trajectory of an oil droplet with a given diameter in the water column.

The application of the vertical drift model would have been sufficient to locate the seafloor source of a droplet if the diameter of the droplet was known. However, this step allows only locating the various probable locations of seafloor sources of a sea surface outbreak and this according to a variable: the

diameter of a droplet. Hence, a third step is required so-called the "sources paths" that correspond to the inverse location of the most common oil diameters SeaFloor Source for each SeaSurface Outbreak.

C. Sources paths algorithm

The diameter of the oil droplet is an important element in the vertical drift and must be taken into account in calculations aimed at locating the seafloor source (SFS). Effectively the diameter of the oil droplet at the SFS is function of the geochemistry of the initial organic matter within the source rock as well as its situation (such as due to its depth, the local heat flow, the pressure, and their residence time within both the source rock, the reservoir, as well as the different migrations (expulsion and secondary migration within the reservoir rock). The smaller it is the longer it stands within the reservoir. Indeed, as given by the equation (eq. 10), the upward velocity of a droplet varies substantially as a function of its diameter. Thus, the bigger the drop, the faster it rises to the surface. And the smaller it is, the slower it ascends (Figure 35, left). The speed of a droplet to rise to the surface is capital since it determines how long the droplet will be under the influence of the marine currents in the water column. In summary, the bigger the drop, the faster it rise, and the less it drifts and vice versa.

As we do not know the diameter of the droplets -and this is the most interesting aspect of this study - we propose a method herein called "sources path" that inverse the SFS depending of the droplet size taking into account the SSO. The first step is to apply the vertical drift model for each oil seep with both different times and diameters. In other words, it consists in finding, for each oil seep, the seafloor sources corresponding to different diameters for a fixed SSO. The line that joins the seafloor sources for an oil seep is called the "sources path" (Figure 35, left). Until now, the more or less exact location of the seafloor source (SFS) is not possible. In order for it to become so, at least a second path applied to different oil seep (different date) is required assuming the fact that they comes from the same SFS. Consequently the crossing of the two paths will give a point of intersection that we consider as the point of potential seafloor source (SFS - see Figure 35, right). For a better accuracy of the location of the seafloor source, a multitude of multidate paths is necessary. Indeed, the greater the number of paths used in the analysis, the more likely the results will be accurate. However, the intersection of more than two paths multidates in one point is unlikely. In most cases, one will have a set of points more or less close to each other. We will speak of a crossing area which delimits the seafloor source.

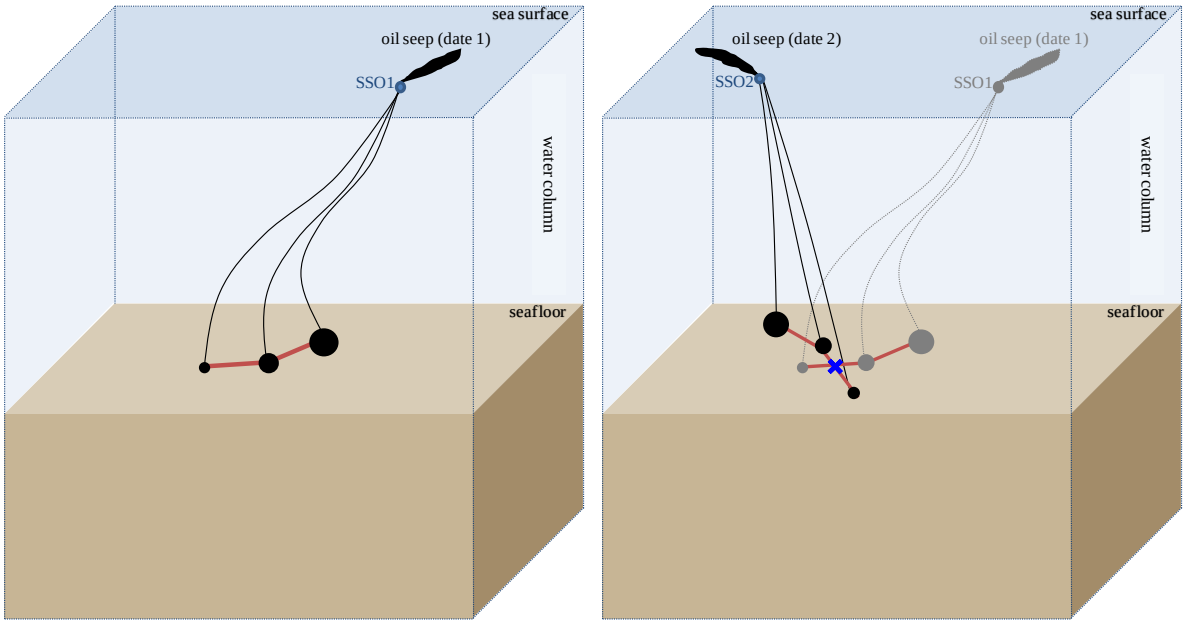

Figure 35. Illustration of the sources paths principle. Left: sources path (red line) of a sea surface outbreak (SSO1) corresponding to an oil seep 1(observed on date 1). The black disks are the seafloor sources corresponding to droplets sizes. Right: sources paths corresponding to the oil seep 1(observed on date 1) and the oil seep 2(observed on date 2). The red point corresponding to the intersection between the two sources paths is likely the seafloor source of the two multidate oil seeps.

VI. Results and validation

A. GOM Oil seeps surface outbreaks (SSO) detection

The manual analysis of the 215 SAR images (acquired in between 2002-2012) led to the identification of 682 oil seeps in the Gulf of Mexico. The location of SSO has been drawn for each oil seep from the location of the fresher oil droplets (Figure 36, left). Note that the oil seeps SSO form usually clusters structures patterns as shown by the normalized density map of the detected oil slicks (Figure 36, right). The latter is computed as the kernel density with the QGIS toolbox in order to better display areas of active seeps. The normalization of the density map has been done according to the SAR images occurrences shown in Figure 32.

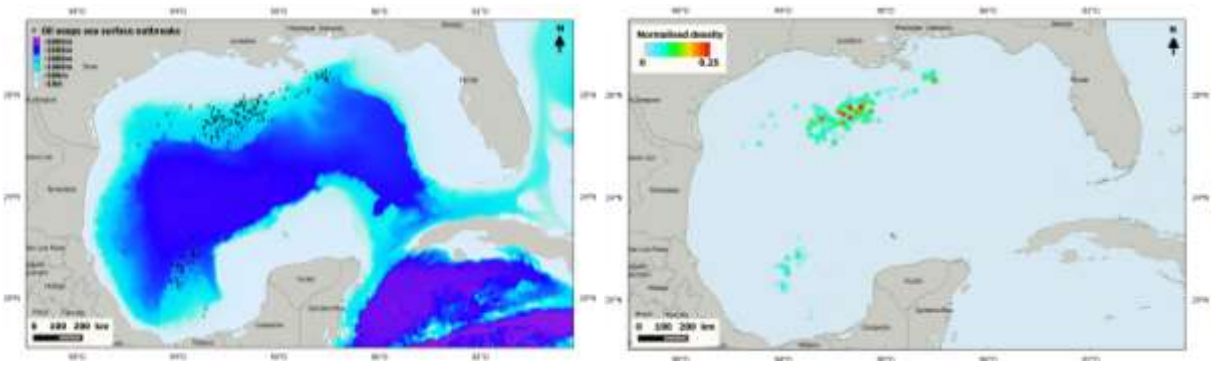

Figure 36. Oil seeps in the Gulf of Mexico. Left: the 682 Sea Surface Outbreaks (SSO = Black dots), calculated from the 682 oil seeps sea surface outbreaks visually detected from 215 SAR images (2002-2012). Colour chart: GOM bathymetry. Right: the normalised density map of the 682 Sea Surface Outbreaks.

The detected oil seeps are concentrated in both (1) the northern part of the Gulf including the Texas-Louisiana Slope and Mississippi Canyon and (2) the south-west area that include the Campeche Knolls. This outcome is consistent with the previous studies (MacDonald et al., 1993; Macdonald et al., 1996; Mitchell et al., 1999; De Beukelear, 2003; Suresh, 2015; Macdonald et al., 2015). According to the normalized density map of observed oil seeps, the northern Gulf of Mexico represents a relatively high density compared to the southern GOM (see Figure 36). This is the reason why we choose herein as an example the northern GOM to illustrate this "sources path methodology".

B. Estimated location of the GOM Oil seeps seafloor sources (SFS)

The second and third steps of the methodology adopted within the framework of this paper (cf. B and C) involve the application of the vertical drift model VDM) within the sea column taking into account the droplet size. In other words, for each oil seep SSO, the VDM has been applied to get the possible locations of the SFSs corresponding to different oil droplets sizes. The oil droplets size range between 0.5mm and 100mm with a stride of 0.05mm. This interval has been fixed according to experiments founded in both the literature (Brewer et al, 2002; Goncharov, 2009). The sources path of an oil seep SSO is the polyline that joins the seafloor sources locations obtained by applying the VDM to this oil seep SSO. Thus, the 1991 seafloor sources correspond to diameters ranging between 0.5mm and 100mm with a stride of 0.05mm. Figure 37 shows an example of two sources paths generated by the VDM from the SSOs of two oil seeps observed on Envisat ASAR WSM image acquired on 02 October 2010 at 16:00:50. The red arrows are the SSOs of the observed oil seeps while the blue points are the seafloor sources corresponding to the droplets diameters sizes (between 0.5mm and 100mm with a stride of 0.05mm). The black polyline that joins the seafloor sources of an oil seep forms the

sources path. For instance, the blue point with the value 0.5 correspond to the seafloor source related to the droplet diameter of 0.5mm, the blue point with the value 100.0 correspond to the seafloor source related to the droplet diameter of 100mm. One may see that the smaller the droplet is, the farthest the seafloor source from the SSO is.

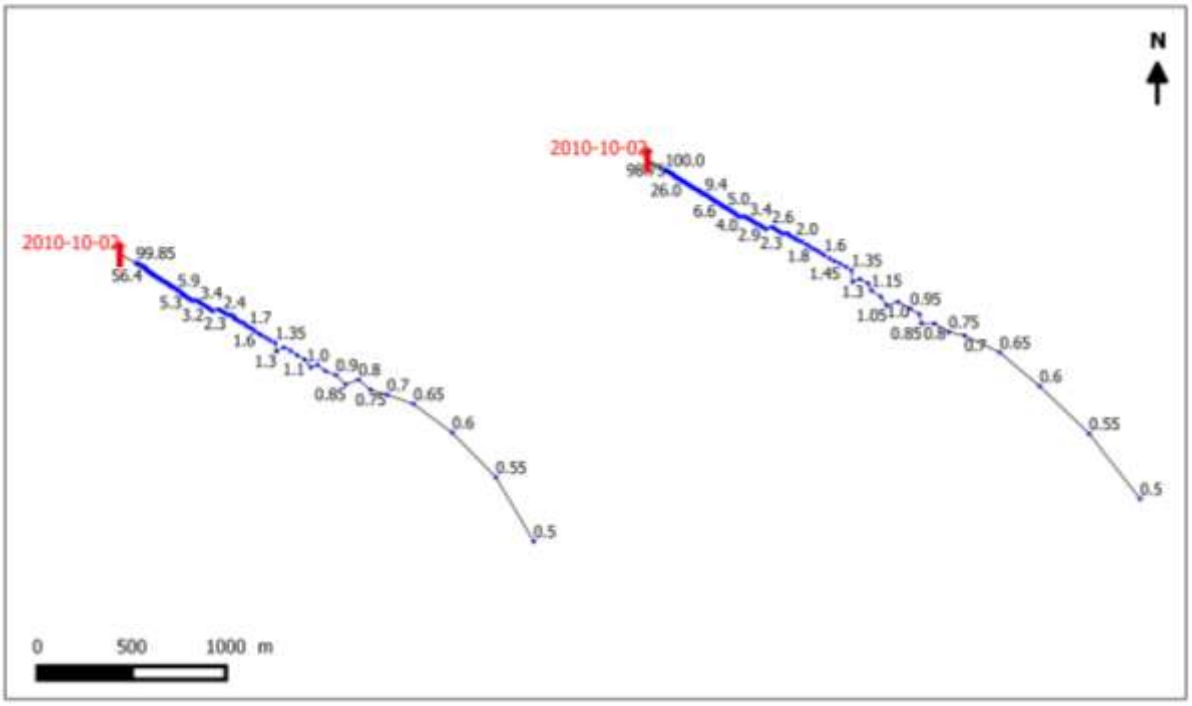

Figure 37. Two sources paths generated by the VDM from the SSOs of two oil seeps observed on Envisat ASAR WSM image acquired on 02 October 2010 at 16:00:50. The red arrows are the SSOs while the blue points are the seafloor sources. The black polyline that joins the seafloor sources of an oil seep forms the sources path. Numbers correspond to the relative oil droplet diameters.

An amount of 682 sources paths corresponding to the 682 oil seeps SSO have been computed. Therefore, the intersections between the 682 sources paths have been calculated. These intersections points correspond to the estimated oils seeps SFS location. For instance, each SFS point intersects two sources paths and therefore, contains two informations: 1/ the diameter (d1) where he intersect the first sources path and 2/ the diameter (d2) where it intersects the second sources path. The two oil seeps occurring on the sea surface at two different dates and whose sources paths intersect at one point, **are supposed to come from the same source on the seafloor so the intersection point of the sources paths which is the SFS**. In an ideal case, the d1 and d2 corresponding to the SFS must be the same. To assess this, we compute the number of occurrences of the calculated oil seeps SFSs as a function of the diameter (d1 or d2) and the difference between d1 and d2 (|d1-d2|) as presented in Figure 38 that the most of the occurrences of the calculated oil seeps SFSs correspond to diameters ranging between

0.5mm and 2mm with a low difference between d1 and d2 of the SFS. Figure 38-b represents a zoom on Figure 38-a on diameters between 0.5mm and 2mm and difference between d1 and d2 between 0.5mm and 2mm. One may see that the most calculated SFSs corresponds to diameters between 0.5mm and 1.45mm. The difference between d1 and d2 of the same SFS is zero. This outcome is a first validation of our methodology since the obtained SFSs correspond to the seafloor sources of oil droplets having the same diameter and seeped at different times.

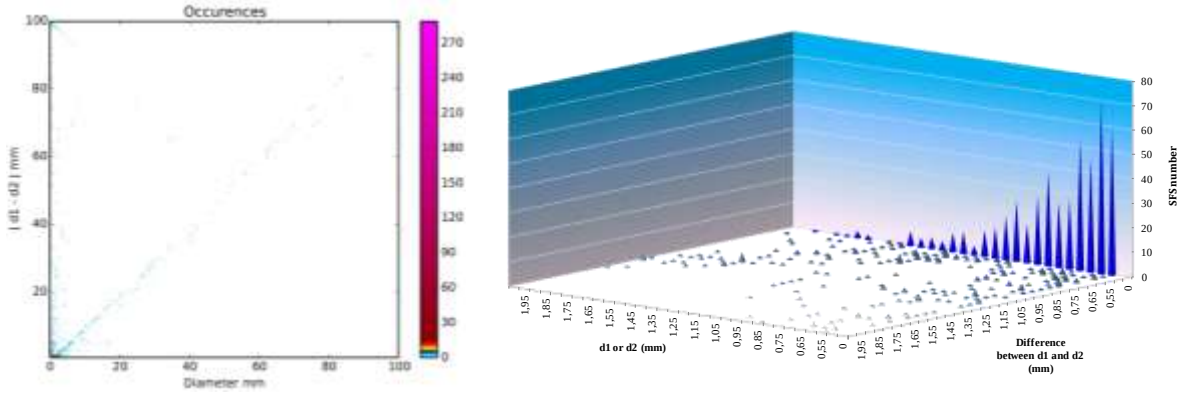

Figure 38. The number of occurrences of the calculated oil seeps SFSs as a function of the diameter (d1 or d2) and the difference between d1 and d2 (|d1-d2|).

An amount of 242 SFS have been obtained. Figure 39 shows the sources paths (black lines) and their intersections (yellow dots) on the Texas-Louisiana continental Slope (left) and an example of the intersection of three sources paths corresponding to three SSO observed on the sea surface at three different dates (2003/10/23, 2009/09/14, and 2010/10/21). The horizontal deflection between the SSO and theirs SFS is given in Figure 40. One may see that the average of the horizontal deflection between the SSO and their SFS is about 2500m.

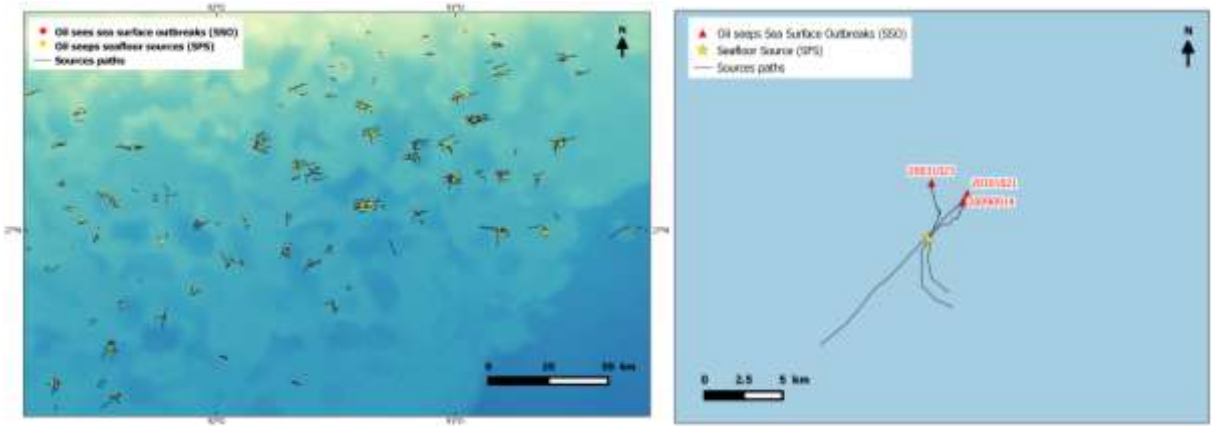

Figure 39. The sources paths and their intersections in the Texas-Louisiana Slope. Left: the intersections points (yellow points) correspond to the estimated seafloor sources (SFS). Right: an example of three sources paths crossing. The yellow star is the estimated SFS of the three oil seeps observed on 23/10/2003, 14/09/2009, and 21/10/2010.

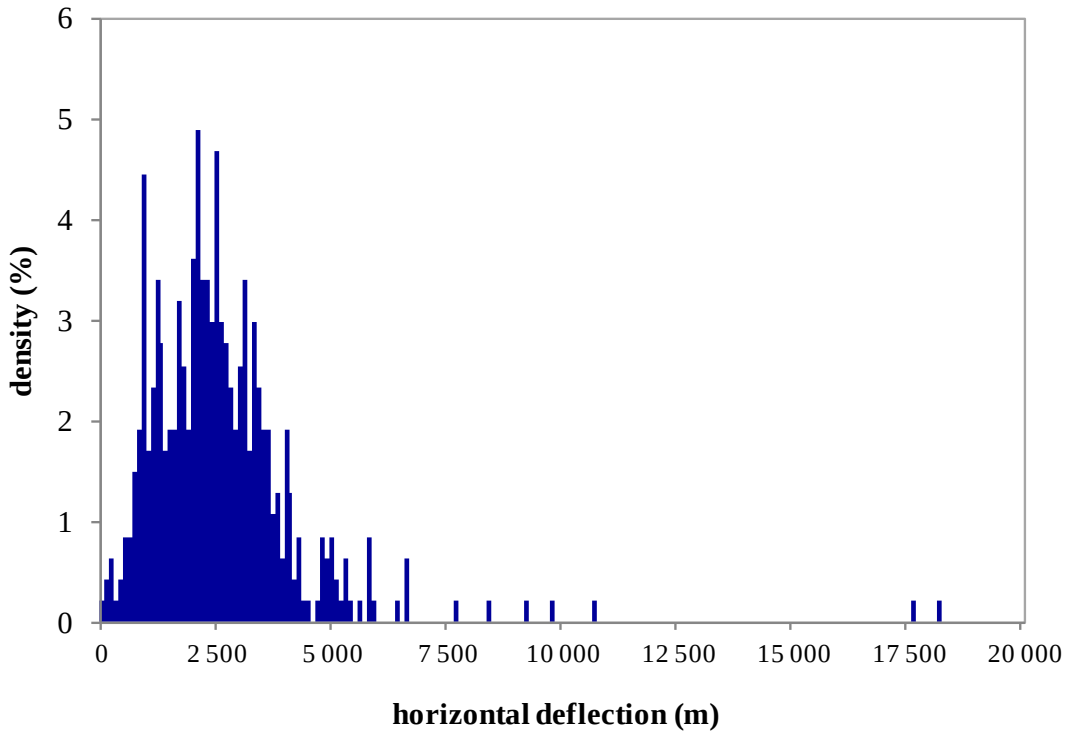

Figure 40. The histogram of the distance of the observed oil seeps from their seafloor sources.

C. Geological validation

In this study, the geological validation focuses on the northern part of the Gulf of Mexico and especially in the Texas-Louisiana continental Slope. As explain above (III-A), the petroleum activity in the Gulf of Mexico is controlled by the salt tectonic (Salvador, 1991; Galloway, 2008). As shown by Figure 41A, the oils seeps SFSs are all located on the outcropping shallow salt. We interpret this as the oil seeps are related to the salt. Moreover, some seismic profiles have been published (Fort and Brun, 2012) among which given by Figure 41C and Figure 41D reveal that generally oil seeps comes from the Allochthonous salt areas.

On Figure 41C and Figure 41D, we superimpose the hill-shade bathymetry, the SFS (red dots) and the seismic profile (see Fort and Brun, 2012). Therefore it appears clearly (Figure 41C and Figure 41D) that the four SFS corresponds to the outcropping Cretaceous-Early Miocene rafts / salt boundary. We believe that the oil seeps may be situated above the allochtonous toward autochtonous salt connections but this needs to be carefully checked with further geological seismic sections as so few are published in the public domain.

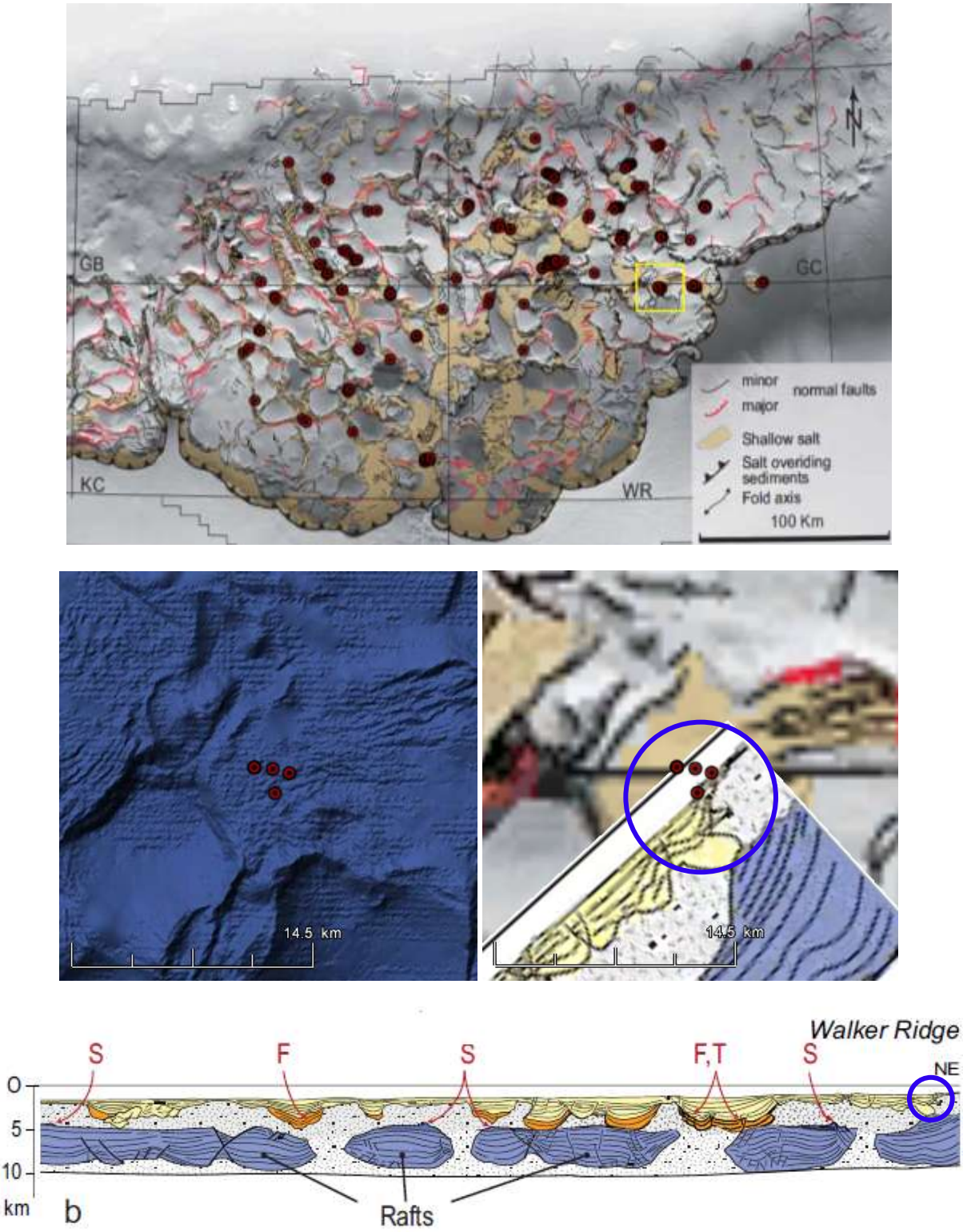

Figure 41. The relationship between oil seeps SFS and the salt tectonic.

VII. Conclusion and perspectives

Indeed, the Sea Surface Outbreak (SSO) of a seepage derived from hundred meters to a few kilometres from its Sea Floor Source (SFS - see references above). We apply herein with a stochastic approach a vertical drift model (VDM) methodology that inverse the uplift displacement within the sea water column of various given oil droplets diameters in order to determine precisely their Sea Floor Sources. Moreover, we combine multidate oil seepages within their vicinity that are assumed to have the same SFS. By inversing their uplift trajectories within the sea water column, we believe that the intersection of source path should correspond to their Sea Floor Sources.

We illustrate this methodology to the northern offshore Gulf of Mexico (GOM) where 682 oil seeps have been manually detected, between 2002 and 2012 using different SAR images. The application of this VDM methodology on a surface of 1.6 million km^2 (Gulf of Mexico) has allowed us, first, to significantly reduce the seepage zone to be studied, indeed, thanks to the analysis of the SAR images. Secondly, the application of the Vertical Drift Model and the development of source paths lead us for the first time to locate in a more precise way both the oil seeps Sea Surface Outbreaks as well as the Sea Floor Sources. The latter was located by the determination of the intersection of source paths inversing the drift within the vertical sea column.

Consequently these results are useful information and interesting complement for oil exploration and production in any marine areas.

Acknowledgments

This work is performed as a part of a PhD research program funded by VisioTerra/UPE (Université Paris-Est) and ANRT/CIFRE. The authors would like to thank The ESA (European Spatial Agency) for the SAR scenes used in this study.

References

Angeles-Aquino, F. J., J. Reyes-Nunez, J. M. Quezada-Muneton, and J. J. Meneses-Rocha, 1994, Tectonic evolution, structural styles, and oil habitat in Campeche Sound, Mexico: Gulf Coast Association of Geological Societies Transactions, v. 44, p. 53 – 62.

Angiuli, Emanuele, F. D. Frate, and L. Salvatori. 2006. “Neural networks for oil spill detection using ERS and ENVISAT imagery.” In Proceedings of SeaSAR’06, 23-26 January 2006, Frascati, Italy, 1–6.

Bird D.E., Burke K., Hall S.A., Casey J.F. 2005, Gulf of Mexico tectonic history: Hotspot tracks, crustal boundaries, and early salt distribution: The American Association of Petroleum Geologists Bulletin, v. 89, p. 311– 328.

Brekke C. and A.h.S. Solberg. 2005. "Oil Spill Detection by Satellite Remote Sensing." Remote Sensing of Environment 95 (2005): 1-13.

Brewer Peter G.,Peltzer, Edward T., Friederich, Gernot, Rehder, Gregor, 2002. Experimental determination of the fate of rising CO2 droplets in Seawater. Environmental Science & Technology 2002 36 (24), 5441-5446. DOI: 10.1021/es025909r.

Buffler, R. T., and Thomas, W. A., 1994, Crustal structure and evolution of the southeastern margin of North America and the Gulf of Mexico basin, in Speed, R. C. ed., Phanerozoic evolution of North American continent-ocean transitions, Geological Society of America, Boulder, CO, pp. 219–264.

Buffler, R. T., and W. A. Thomas, 1994, Crustal structure and evolution of the southeastern margin of North America and the Gulf of Mexico, in R. C. Speed, ed., Phanerozoic evolution of North American continent-ocean transitions: Boulder, Geological Society of America, The Decade of North American Geology Summary Volume, p. 219 – 264.

Chang, Lena, Z. S. Tang, S. H. Chang, and Yang-Lang Chang. 2008. “A region-based GLRT detection of oil spills in SAR Images.” Pattern Recognition Letters 29 (14): 1915–23. doi:10.1016/j.patrec.2008.05.022.

De Beukelear, S.M., 2003. Remote sensing analysis of natural oil and gas seeps on the continental slope of the northern Gulf of Mexico. Thesis: Texas A&M University.

Del Frate, Fabio, A. Petrocchi, J. Lichtenegger, and G. Calabresi. 2000. “Neural networks for oil spill detection using ERS-SAR data.” IEEE Transactions on Geoscience and Remote Sensing 38 (5): 2282–87. doi:10.1109/36.868885.

Del Frate, Fabio, D. Latini, C. Pratola, and F. Palazzo. 2013. “PCNN for automatic segmentation and information extraction from X-band SAR imagery.” International Journal of Image and Data Fusion 4 (1): 75–88. doi:10.1080/19479832.2012.713398.

Dhont, D., Dubucq, D., 2016. "Method for detecting hydrocarbon deposits". Organisation Mondiale de la Propriété Intellectuelle, WO 2016/024050 A1.

Espedal H. A.. 1999. "Satellite SAR oil spill detection using wind history information." International Journal of Remote Sensing 20(1999): 49-65.

Espedal, H. A. and Johannessen, O.M., 2000. Detection of oil spills near offshore installations using synthetic aperture radar (SAR). International Journal of Remote Sensing, issue 21, pages 2141-2144.

Espedal, H.A.,Wahl, T., 1999. Satellite SAR oil spill detection using wind history information. Int. J. Remote Sens. 20, 49–65.

Fiscella, B., A. Giancaspro, F. Nirchio, P. Pavese, and P. Trivero. 2000. “Oil spill detection using marine SAR images.” International Journal of Remote Sensing 21 (18): 3561–66. doi:10.1080/014311600750037589.

Fort X. and Brun J. P., 2012. Kinematics of regional salt flow in the northern Gulf of Mexico. G. I. ALSOP, S. G. ARCHER, A. J. HARTLEY, et al. Salt Tectonics, Sediments and Prospectively, Geological Society of London, pp.265-287, 2012, Geological Society of London, Special Publications, n363, 978-1862393417. <10.1144/SP363.12>. <insu-00717207>

Galloway,W. E., 2008. Depositional evolution of the Gulf of Mexico sedimentary basin, Sedimentary Basins of the world, 5, 505–549.

Garcia-Pineda, Oscar, I. R. MacDonald, and B. Zimmer. 2008. "Synthetic Aperture Radar image processing using the supervised Textural-Neural Network Classification Algorithm." In IGARSS 2008 - 2008 IEEE International Geoscience and Remote Sensing Symposium, IV – 1265–IV – 1268. IEEE. doi:10.1109/IGARSS.2008.4779960.

Garcia-Pineda, Oscar, I. R. MacDonald, B. Zimmer, B. Shedd, and H. Roberts. 2010. “Remote-sensing evaluation of geophysical anomaly sites in the outer continental slope, northern Gulf of Mexico.” Deep Sea Research Part II: Topical Studies in Oceanography 57 (21-23). Elsevier: 1859–69. doi:10.1016/j.dsr2.2010.05.005.

Gasull, A., X. Fábregas, J. Jiménez, F. Marqués, V. Moreno, and M. A. Herrero. 2002. “Oil spills detection in SAR images using mathematical morphology.” In 11th European Signal Processing Conference (EUSIPCO 2002), 25–28. Toulouse, France. doi:10.1.1.81.3086.

Goncharov K. Prof Dr, 2009. Simulation of oil drops dynamics in seawater environment, Journal of Marine Engineering & Technology, 8:3, 21-28

Harry, D. L., and Londono, J., 2004, Structure and evolution of the central Gulf of Mexico continental margin and coastal plain, southeast United States. Geological Society of America Bulletin, v. 116, pp. 188–199.

Hood, Kenneth C, P. O. Gross, M. L. Wenger, and S. C Harrison. 2002. “Hydrocarbon systems analysis of the northern Gulf of Mexico: delineation of hydrocarbon migration pathways using seeps and seismic imaging.” In AAPG Studies in Geology 48 and SEG Geophysical References Series No.11, Surface Exploration Case Histories: Applications of Geochemistry, Magnetics and Remote Sensing, D. Schumacher and LA. LeSchack, 25–40.

Jackson C. R. and Apel J. R., 2004. Synthetic Aperture Radar marine user's manual. NOAA, Washington, DC, pp 464.

Jacques, J. M., and Clegg, H., 2002, Late Jurassic source rock distribution and quality in the Gulf of Mexico: inferences from plate tectonic modeling. Gulf Coast Association of Geological Societies Transactions, v. 52, pp. 429–440.

Jatiault R., Dubucq D., Loncke L., Dhont D., 2017. Monitoring of natural oil seepage in the Lower Congo Basin using SAR observations.. Remote Sensing of Environment, Elsevier, 191, pp.258-272.

Johannessen, O.M., Sandven, M., Jenkins, A.D., Durand, D., Petterson, L.H., Espedal, H., Evensen, G., Hamre, T., 2000. Satellite earth observation in operational oceanography. Coast. Eng. 41, 155–176.

Judd A, Hovland M. 2007. Seabed Fluid Flow: The Impact on Geology, Biology and the Marine Environment. Cambridge: Cambridge University Press.

Kanaa, T. F. N., E. Tonye, G .Mercier, V. P. Onana, J. M. Ngono, P. L . Frison, J. P. Rudant, and R. Garello. 2003. "Detection of oil slick signatures in SAR images by fusion of hysteresis thresholding responses." In IGARSS 2003. 2003 IEEE International Geoscience and Remote Sensing Symposium. Proceedings (IEEE Cat. No.03CH37477), 4:2750–52. IEEE. doi:10.1109/IGARSS.2003.1294573.

Körber, Jan-Hendrik, H. Sahling, T. Pape, C. dos Santos Ferreira, I. R. MacDonald, and G. Bohrmann. 2014. "Natural oil seepage at Kobuleti ridge, eastern Black Sea." Marine and Petroleum Geology 50 (February). Elsevier Ltd: 68–82. doi:10.1016/j.marpetgeo.2013.11.007.

Leifer, I., Lehr, W.J., Simecek-Beatty, D., Bradley, E., Clark, R., Dennison, P., Hu, Y., Matheson, S., Jones, C.E., Holt, B., Reif, M., Roberts, D.A., Svejkovsky, J., Swayze, G., Wozencraft, J., 2012. State of the art satellite and airborne marine oil spill remote sensing: application to the BP deepwater horizon oil spill. Remote Sens. Environ. 124:185–209. http://dx.doi.org/10.1016/j.rse.2012.03.024.

Liu, A. K., C. Y. Peng, and S. Y. Chang. 1997. "Wavelet analysis of satellite images for coastal watch." IEEE Journal on Ocean Engineering 22 (1): 9–17.

MacDonald, I. R., et al. 2015, Natural and unnatural oil slicks in the Gulf of Mexico, J. Geophys. Res. Oceans, 120, doi:10.1002/2015JC011062.

MacDonald, I. R., Leifer I., Sassen R., Mitchell R., and Guinasso Jr.N., 2002. "Transfer of hydrocarbons from natural seeps to the water column and atmosphere", Geofluids 2(2):95 - 107. DOI: 10.1046/j.1468-8123.2002.00023.x.

MacDonald, I. R., Redly J. F.,. Best Jr., S. E, Venkataramaiah R, Sassen R., Guinasso Jr.N., and Amos J., 1996, Remote sensing inventory of active oil seeps and chemosynthetic communities in the northern Gulf of Mexico, in D. Schurnacher and M. A. Abrams, eds., Hydrocarbon migration and its near-surface expression: AAFG Memoir 66, p. 27-37.

MacDonald., Ian. R, N.L. Guinasso, S. G. Ackleson, J. F. Amos, R. Duckworth, and J. M. Brooks. 1993. “Natural oil slicks in the Gulf of Mexico visible from space.” Journal of Geophysical Research 98 (C9): 16,351–16,364.

Mano M., Beisl C., Soares C., 2016. " Oil Seeps on the seafloor of Perdido, Mexico", AAPG , SEG International Conference & Exhibition 2016 – Cancún, Mexico.

Marghany Maged. 2001. "RADARSAT automatic algorithms for detecting coastal oil spill pollution." International Journal of Applied Earth Observation and Geoinformation 3.2 (2001): 191-196.

Marghany Maged. 2014. "Utilization of a genetic algorithm for the automatic detection of oil spill from RADARSAT-2 SAR satellite data." Marine pollution bulletin 89.1 (2014): 20-29.

Marghany Maged. 2015. "Automatic detection of oil spills in the Gulf of Mexico from RADARSAT-2 SAR satellite data." Environmental Earth Sciences 74.7 (2015): 5935-5947.

Marton, G., and R. T. Buffler, 1994, Jurassic reconstruction of the Gulf of Mexico Basin: International Geology Review, v. 36, p. 545 – 586.

Mercier G.; Girard-Ardhuin F., 2006. Partially Supervised Oil Slick Detection by SAR Imagery using Kernel Expansion, IEEE-TGRS, vol 44(10), pp 2839-2846.

Mitchell, R., MacDonald I.R., Kvenvolden,K., 1999. Estimates of total hydrocarbon seepage in to the Gulf of Mexico based on satellite remote sensing images. EOS Supplement 80,49.

Najoui Z., Deffontaines B., Xavier J. P. and Riazanoff S., submitted A, " Wind Speed and Instrument Modes Influence on the Detectability of Oil Slicks using SAR Images: a Stochastic Approach", submitted to Remote Sensing of Envirnment.

Najoui Z., Deffontaines B., Xavier J. P. and Riazanoff S., submitted B, "A statistical approach to preprocess and enhance C-Band SAR images in order to detect automatically marine oil slicks", submitted to IEEE Transactions Geoscience and Remote Sensing (TGRS).

Oey LY, Ezer T, Lee HC. 2005. Loop currents, rings and related circulation in the Gulf of Mexico: a review of numerical models and future challenges. Geophysical Monograph Series 161:31–56.

Pindell, J. L., 1985, Alleghenian reconstruction and subsequent evolution of the Gulf of Mexico, Bahamas and proto-Caribbean: Tectonics, v. 4, p. 1 – 39.

Pindell, J. L., 1994, Evolution of the Gulf of Mexico and the Caribbean, in S. K. Donovan and T. A. Jackson, eds., Caribbean geology: An introduction: Kingston, University of the West Indies Publishers Association, p. 13 – 39.

Riazanoff S. and Gross K., 2013. Enhancing ENVISAT ASAR WSM Segments To Detect Oil Spills In the Framework Of The "20 Years Of Oil Routes" Project. ESA Living Planet Symposium, Proceedings of the conference held on 9-13 at Edinburgh in United Kingdom. ESA SP-722. 2-13, p.229

Ross, D. A. 1988. Introduction to Oceanography. 4th ed. Englewood Cliffs, NJ: Prentice Hall,.

Salvador, A., 1987, Late Triassic-Jurassic paleogeography and origin of Gulf of Mexico basin. AAPG Bulletin, v. 71, pp. 419–451.

Salvador, A., 1991, Origin and development of the Gulf of Mexico Basin, in A. Salvador, ed., The Gulf of Mexico Basin: Geological Society of America, The geology of North America, v. J, p. 389 – 444.

Sandrea R. and Sandrea I., 2010. Deepwater crude oil output: how large will the uptick be? Oil & Gas Journal, Russia, Volume 108.41, pp. 30–34.

Sawyer, D. S., Buffler, R. T., and Pilger, R. H., Jr., 1991, The crust under the Gulf of Mexico basin, in Salvador, A. ed., The Gulf of Mexico Basin, The Geology of North America, Geological Society of America, Boulder, CO, v. J, pp. 53–72.

Shu Y.; Li J.; Yousif H. and Gomes G., 2010. Dark-spot detection from SAR intensity imagery with spatial density thresholding for oil-spill monitoring. Remote Sensing of Environment, Volume 114, Issue 9, 15 September 2010, pp 2026 - 2035.

Smith, R. H., Johns, E. M., Goni, G. J., Trinanes, J., Lumpkin, R., Wood, A. M., Kelble, C. R., Cummings, S. R., Lamkin, J. T., Privoznik, S., 2014. Oceanographic conditions in the Gulf of Mexico in July 2010, during the Deepwater Horizon oil spill. Cont. Shelf Res. 77, 118–131. doi:10.1016/j.csr.2013.12.009.

Solberg, A. H. S., G. Storvik, R. Solberg, and E. Volden., 1999. Automatic detection of oil spills in ERS SAR images. IEEE Transactions on Geoscience and Remote Sensing 37 (4): 1916–24. doi:10.1109/36.774704.

Sturges, W. and R. Leben, 2000. Frequency of ring separations from the Loop Current In the Gulf of Mexico: A revised estimate, J. Phys. Oceanogr., 30, 1814-1818.

Sturges, W., Lugo-Fernandez, A. and Shargel, M. D., 2005. Introduction to Circulation in the Gulf of Mexico, in Circulation in the Gulf of Mexico: Observations and Models (eds W. Sturges and A. Lugo-Fernandez), American Geophysical Union, Washington, D. C.. doi: 10.1029/161GM02.

Suresh G., 2015. Offshore oil seepage visible from space: A Synthetic Aperture Radar (SAR) based automatic detection, mapping and quantification system. Thesis: University of Bremen, Bremen, Germany.

Trivero, P., Biamino,W., 2010. ObservingMarine Pollution With Synthetic Aperture Radar, Observing Marine PollutionWith Synthetic Aperture Radar, Geosciences and Remote Sensing, New Achievements.

Vukovich, F.M.,Maul,G.A.,1985.CycloniceddiesintheeasternGulfofMexico. J. Phys.Oceanogr.15,105–117, http://dx.doi.org/10.1175/1520-0485(1985) 015o0105:CEITEG42.0.CO;2.

White, G. W., 1980, Permian –Triassic continental reconstruction of the Gulf of Mexico –Caribbean area: Nature, v. 283, p. 823 – 826.

White, G. W., and K. C. Burke, 1980, Outline of the tectonic evolution of the Gulf of Mexico and Caribbean region: Houston Geological Society Bulletin, v. 22, no. 10, p. 8 – 13.

Winker, C. D., and R. T., Buffler, 1988, Paleogeographic evolution of early deep-water Gulf of Mexico and margins, Jurassic to middle Cretaceous (Comanchean): AAPG Bulletin, v. 72, p. 318– 346.

Xu L.; Li J. and Brenning A.. 2014. "A comparative study of different classification techniques for marine oil spill identification using RADARSAT-1 imagery." Remote Sensing of Environment141 (2014): 14-23.

Xu L.; Shafiee M. J.; Wong A.; Li F.; Wang L.; and Clausi D. A, 2015. Oil spill candidate detection from SAR imagery using a thresholding-guided stochastic fully-connected conditional random field model. CVPR, pp 86.

Zavala-Hidalgo, J., S. L., Morey, and J. J. O'Brien, 2003a. Cyclonic eddies northeast of the Campeche Bank from altimetry data. J. Phys. Oceanogr., 33, 623–629.

4.3 Conclusion du chapitre

Le modèle de dérive verticale a prouvé - les résultats de la présente étude l'démontrent amplement - son efficacité en l'estimation des sources des nappes sur le plancher océanique. En effet, le point d'éclosion en surface de la mer d'une nappe d'huile peut être dérivé d'une centaine de mètres à quelques kilomètres de sa source sur plancher océanique (SSF). Nous procédons ici par une approche stochastique et modèle de dérive verticale (VDM) qui trace en inverse le déplacement dans la colonne d'eau d'une gouttelette d'huile d'une taille de diamètre donnée afin de déterminer précisément sa source SFS. Nous combinons des nappes d'huile multidates. En inversant leur voyage dans la colonne d'eau, nous sommes en mesure de dire que les intersections des chemins des sources soient les sources des nappes observées en surface.

Nous illustrons cette méthodologie dans le nord du golfe du Mexique (GOM) où 682 nappes d'huile ont été détectées manuellement, entre 2002 et 2012 en utilisant différentes images radar. L'application de la méthodologie VDM sur une surface de 1,6 million de km, (Golfe du Mexique), nous a permis de réduire de manière significative la zone de fuite à étudier grâce à l'analyse des images radar. Le reste de l'étude (application du modèle de dérive verticale et développement des chemins sources) a permis de localiser d'une manière plus précise, à la fois, les points d'éclosion en surface de la mer et les sources sur plancher de la mer. Ce dernier était localisé par la détermination de l'intersection des chemins sources inversant la dérive verticale dans la colonne d'eau.

Les résultats de cette étude sont une information utile et un complément intéressant pour l'exploration pétrolière dans toutes les zones marines.

Conclusions, limites, et perspectives

Ce travail de thèse a pour l'objectif d'une part, d'optimiser la détection des nappes d'huile en surface de la mer (article 1 + article 2), et d'autre part, de détecter les sources sur le fond océanique des nappes d'huile d'origine naturelle observées en surface de la mer (article 3). D'un point de vue méthodologie général, cette thèse se base sur une approche stochastique qui tire profil du grand nombre (BigData), la disponibilité et la résolution spatiale et temporelle des images radar. L'étude est composé de trois parties s'intéressant aux "Prétraitement optimal des images radar et à la modélisation des dérives de nappes d'hydrocarbures pour l'aide à la photo-interprétation en exploration pétrolière et surveillance environnementale". D'un point de vue résultats, ce travail nous a conduits à un certain nombre de résultats dont le but est d'améliorer la détection des nappes d'huile en surface de la mer, qu'elles soient d'origine naturelle ou anthropique. Il nous a également permis de développer une nouvelle méthode permettant une meilleure localisation des sources des nappes, quand celles-ci sont d'origine naturelle. Il a été aussi une occasion de nous pencher sur le prétraitement des données qui permet l'analyse et l'interprétation des images radar que ce soit manuellement ou automatiquement. Trois articles distincts soumis (chapitres 2, 3, et 4) illustrent et valorisent l'essentiel du travail effectué. Chacun de ces articles peut être considéré séparément. L'ensemble de ce travail permet de rendre plus facile, plus exacte et plus globale la détection des nappes d'huile ainsi que la localisation de leurs sources naturelles.

Prétraitement optimal

La première partie est focalisée sur le prétraitement et la segmentation des images radar. Elle est dictée par la nécessité d'optimiser la détection des nappes à travers l'automatisation de certaines de ses étapes. Il s'agit d'une meilleure maitrise des données fournies par le radar à synthèse d'ouverture dont le flux est très élevé.

L'objectif principal de cette étude a été de trouver les meilleurs paramètres de prétraitement et d'amélioration à même d'optimiser le seuillage automatique et le nettoyage des images radar. Nous nous sommes centrés pour faciliter et assister la segmentation des "objets noirs" et rendre plus fiable encore la reconnaissance automatique des nappes d'hydrocarbures. Le but était d'avoir une image binaire qui soit la plus proche possible de la détection manuelle, à partir d'une seule valeur seuil, quelle que soit la distance au nadir, l'emplacement sur Terre, les conditions météorologiques... Il est utile de rappeler que l'approche employée dans le cadre de cette étude a consisté à isoler les paramètres déjà cités car la détection des nappes d'huile est un phénomène multivarié.

Après analyses et vérifications, nous avons constaté qu'une adaptation au modèle rétrodiffusion CMOD convient parfaitement au prétraitement des images ScanSAR. En effet, elle homogénéise les images et met en évidence les nappes de pétrole. S'il n'y a pas de problème dû au mode d'acquisition ScanSAR, l'étirement local peut être une alternative avec une fenêtre statistique de 30 km. Une ouverture par zone (SOR) 4-connexe suivi d'une fermeture morphologique à l'aide de l'élément structurant ES5 donne de bons résultats. D'une part, le nettoyage consiste en l'élimination du bruit. Il s'agit d'appliquer un filtre associé basé sur une ouverture par zone SOR dont le but est de ne conserver que les composants connectés qui ont une taille supérieure à un objet de taille donnée. D'autre part, le nettoyage consiste à obtenir des formes homogènes et compactes comme la plupart des formes détectées manuellement. En effet, l'application de la zone d'ouverture ne conserve que les objets d'intérêt; Cependant, elle a également l'effet de produire des formes avec l'effet "barbouillé". L'opérateur morphologique de fermeture qui consiste à appliquer une dilatation suivie d'une érosion permet de rendre les formes plus compactes.

L'influence de la vitesse du vent sur la détectabilité des nappes d'huile

L'influence de la vitesse du vent sur la détectabilité des nappes d'huile sur les surfaces marines à partir d'images radar est un sujet auquel beaucoup de recherches se sont intéressées (Brekke and Solberg, 2005; Garcia-Pineda et al., 2009; Fingas and Brown, 2014). Cependant, celles-ci ont employé des approches purement empiriques appliquées à des cas d'accidents pétroliers marins, dont la nature d'huile est très particulière. Dans le cadre de cette thèse, 1333 images et un échantillon de presque 4000 nappes d'huiles (de différentes natures et origines) ont été analysées, dans le but d'arriver à déterminer l'intervalle de la vitesse de vent optimal pour une meilleure détection, et ce quelles que soient la nature et la provenance des nappes. D'où le premier résultat de la deuxième partie (Chapitre 2): une détectabilité optimale est assurée lorsque la vitesse du vent est comprise entre 2.09 et 8.33 m/s. Au-delà de ces conditions, il ya peu de chance (5%) de détecter une nappe d'huile. Cet intervalle tranche clairement avec ceux déjà annoncés dont nous citons : 3 à 7-10 m/s (Brekke and Solberg, 2005), 3.5 à 7 m/s (Garcia-Pineda et al., 2009), 1.5-10 m/s (Fingas and Brown, 2014), et 1 à 7°m/s (Marghany, 2014a).

Il est à noté que notre approche pour fixer une vitesse de vent optimale pour la détection des nappes vise à être globale et représentative des types et des âges des nappes d'huile, de la saisonnalité, des contextes géographiques, etc. Les mesures ponctuelles et les études empiriques ne sont pas en mesure de répondre –du moins à l'heure actuelle– à nos besoins de recherche. L'approche stochastique est, de ce fait, la plus indiquée pour les buts que nous nous sommes fixés.

Toujours dans l'optique d'une meilleure compréhension de l'influence de la vitesse du vent sur la détectabilité des nappes, nous avons procédé à une normalisation statistique de la distribution des vitesses de vent et nous sommes parvenus à un autre résultat : contrairement aux recherches

précédentes qui sont purement empiriques, cette étude montre clairement que plus la vitesse du vent est élevée meilleure est la détectabilité. Cela, bien entendu, dans l'intervalle: 2.09 et 8.33 m/s.

L'influence des paramètres des capteurs

Outre l'influence de la vitesse de vent sur la détectabilité, la première des trois études que compte cette thèse s'est penchée sur l'influence des paramètres des capteurs. Etablir un ordre de performance des 5 modes en question nous a semblé d'une grande importance, car cela permettra de savoir lequel est le plus efficace. Il a été ainsi démontré que le mode IW (Sentinel-1), avec une résolution spatiale de 5x20m, est le plus approprié pour détecter une nappe d'huile à haute vitesse du vent. Cela, ça va de soi, toujours dans l'intervalle déjà arrêté : 2.09 et 8.33 m/s. L'explication la plus plausible à cela est la suivante : les nappes, sous l'influence des vents forts, se cassent, ce qui fait que seul le mode IW présente la résolution suffisante pour arriver à les détecter. En effet, la haute résolution des images qu'offre ce mode permet de détecter les fragments de la nappe qui se cassent sous les vents forts.

Modèle de la dérive verticale des nappes d'huile d'origine naturelle

Pour la prospection pétrolière dans le domaine marin, détecter les nappes d'huiles en surface est loin d'être suffisant. La raison est bien évidemment le phénomène de la dérive verticale conditionnée par la vitesse ascensionnelle et les conditions hydrodynamiques. En effet, la source d'un suintement n'est jamais en ligne verticale avec le point de son apparition sur la surface marine. Des dérives, pouvant aller jusqu'à 5 kilomètres, sont possibles (Najoui et al, 2017, soumis). Ce phénomène rend difficile la localisation des sources sur le plancher océanique, sans laquelle toute action de forage comportera de très hauts risques. Pour remédier à cela, des modèles de dérive verticale ont été élaborés. Sauf qu'aucun d'eux n'a pris en considérations la taille des gouttelettes qui est un facteur important dans la dérive verticale. La méthode que nous proposons dans la troisième étude de cette thèse permet de remonter aux sources des suintements sur le plancher avec plus d'exactitude, et ce indépendamment des informations (pas toujours disponibles) quant à la taille des gouttelettes. Il ne serait pas vraiment utile de s'attarder ici sur les résultats obtenus suite à notre étude menée dans le Golf du Mexique (ceux-ci sont largement explicités dans l'article 3 , chapitre 4). En fait, ce qui est le plus intéressant et le plus innovant et qui mérite le plus d'attention est la méthode "chemin des sources".

Il s'agit en premier lieu d'appliquer le modèle de la dérive verticale à différents diamètres de gouttelette pour chaque fuite d'huile. En d'autres termes, ça consiste à trouver, pour chaque fuite d'huile, les sources sous-marines correspondant à des diamètres différents. La ligne qui rejoint les sources pour une fuite d'huile est appelée « chemin des sources ». Jusque-là la localisation plus au moins exacte du point source n'est pas possible. Pour que celle-ci le devienne, on a besoin d'au moins un deuxième chemin des sources appliqué à une nappe différente (d'une date différente). Le croisement des deux chemins donnera un point d'intersection, considéré comme étant le point source potentiel. Pour une meilleure précision de la localisation, l'élaboration d'une multitude de chemins est

nécessaire. En effet, plus un grand nombre de chemins est employé dans l'analyse, plus on a de chances que les résultats soient précis.

Limites

Des critiques à l'égard de notre méthodologie quand à l'utilisation de modèles (ECMWF, HYCOM, CMOD) peuvent être formulées. En effet, nous sommes conscients des limites des modèles numériques utilisés. Par exemple, le modèle ECMWF a une résolution temporelle de 6-heures et pour avoir les champs de vent à l'heure de l'acquisition des images radar, il est nécessaire de procéder à une interpolation temporelle. Par conséquent, il ne serait pas faux de dire que les interpolations des sorties modèles impliquent des erreurs et inexactitudes et que des observations in situ seraient mieux. Cependant, en l'absence de données in situ dans chaque lieu sur Terre, l'interpolation à partir de modèles reste la meilleure approche pour les objectifs que nous avons définis: définir les conditions optimales pour la détection des nappes d'huile à **l'échelle globale**. En outre, les modèles utilisés sont disponibles avec des méthodes d'assimilation et d'homogénéisation validées par des experts. Enfin, d'un point de vue statistique, avec un grand nombre d'observations (approche stochastique), les erreurs dues à l'interpolation temporelle se compensent.

Perspectives

Outre la méthodologie adoptée dans cette thèse ainsi que les résultats obtenus et qui fournissent les moyens pour des applications notamment en surveillance des zones maritime et en exploration pétrolière, des améliorations sont envisageables. Pour la première étude, outre les prétraitements et la segmentation des images radar, il serait important de précéder à une classification automatique des objets sombres et notamment les nappes d'huile. Quant à la deuxième étude, il serait intéressant de la reprendre avec des données plus résolues que ce soit pour les images radar ou les données de vents. Il serait également intéressant d'étudier, avec la même approche stochastique, l'influence de la polarisation, la température et la salinité de l'eau sur la détectabilité des nappes d'huiles. Pour la troisième étude sur le modèle de la dérive verticale, il serait important de réaliser des expériences en grandeur réelle de vitesse ascensionnelle avec des marqueurs de tailles différentes, analyser et voir s'il ya une modification de la composition de la matière organique.

References

- Alpers W. and Huhnerfuss H., 1988 “Radar signatures of oil films floating on the sea surface and the Marangoni effect,”J. Geophys. Res., vol. 93, pp. 3642–3648.
- Alpers, W., 1985, "Theory of radar imaging of internal waves". Nature, 314, 245-247.
- Alpers, Werner, and H. A. Espedal. 2004. "Chapter 11. Oils and Surfactants." In Synthetic Aperture Radar Marine User’s Manual, edited by Christopher R Jackson and John. R. Apel, 263–75. Washington, DC: U.S Department of Commerce, National Oceanic and Atmospheric Administration, National Environmental Satellite, Data and Information Service, Office of Research and Applications.
- Angeles-Aquino, F. J., J. Reyes-Nunez, J. M. Quezada-Muneton, and J. J. Meneses-Rocha, 1994, Tectonic evolution, structural styles, and oil habitat in Campeche Sound, Mexico: Gulf Coast Association of Geological Societies Transactions, v. 44, p. 53 – 62.
- Angiuli, Emanuele, F. D. Frate, and L. Salvatori. 2006. “Neural networks for oil spill detection using ERS and ENVISAT imagery.” In Proceedings of SeaSAR’06, 23-26 January 2006, Frascati, Italy, 1–6.
- Apel J.R., 1987. "Principles of ocean physics. Academic Press, 634pp.
- Asuero A. G., Sayago A., and A. G. González, 2006. "The Correlation Coefficient: An Overview" Critical Reviews in Analytical Chemistry: 41-59. DOI: 10.1080/10408340500526766.
- Bayramov, E. R., Buchroithner, M. F., and Bayramov, R. V., 2015. "Detection of oil pollution hotspots and leak sources through the quantitative assessment of the persistence and temporal repetition of regular oil spills in the caspian sea using remote sensing and gis." ISPRS Ann. Photogramm. Remote Sens. Spatial Inf. Sci., II-3/W5:451-457. doi:10.5194/isprsannals-II-3-W5-451-2015, 2015.
- Bird D.E., Burke K., Hall S.A., Casey J.F. 2005, Gulf of Mexico tectonic history: Hotspot tracks, crustal boundaries, and early salt distribution: The American Association of Petroleum Geologists Bulletin, v. 89, p. 311– 328.
- Bliven, L., P. W. Sobieski, and C. Craeye, Rain generated ring-waves: Measurements and modelling for remote sensing, Int. J. Remote Sens., 18, 221-228, 1997.

- Brekke C. and A.h.S. Solberg. 2005. "Oil Spill Detection by Satellite Remote Sensing." Remote Sensing of Environment 95 (2005): 1-13.
- Brewer Peter G.,Peltzer, Edward T., Friederich, Gernot, Rehder, Gregor, 2002. Experimental determination of the fate of rising CO2 droplets in Seawater. Environmental Science & Technology 2002 36 (24), 5441-5446. DOI: 10.1021/es025909r.
- Buchroithner, M. F. 2001. "A decade of trans-European remote sensing cooperation." Balkema, Rotterdam ISBN 90 5809 1872 (2001): 131-135.
- Buffler, R. T., and Thomas, W. A., 1994, Crustal structure and evolution of the southeastern margin of North America and the Gulf of Mexico basin, in Speed, R. C. ed., Phanerozoic evolution of North American continent-ocean transitions, Geological Society of America, Boulder, CO, pp. 219–264.
- Chang, Lena, Z. S. Tang, S. H. Chang, and Yang-Lang Chang. 2008. "A region-based GLRT detection of oil spills in SAR Images." Pattern Recognition Letters 29 (14): 1915–23. doi:10.1016/j.patrec.2008.05.022.
- Charbonneau F. 2006. "Caractérisation du coefficient de rétrodiffusion radar des surfaces d'hydrocarbure: Modélisation et interprétation." Thesis (Ph.D.)-Universite de Sherbrooke (Canada), Publication Number: AAINR14847; ISBN: 9780494148471.
- Craeye, C., P. W. Sobieski, and L. F. Bliven, 1997: Scattering by artifical wind and rain roughened water surfaces at oblique incidences. Int. J. Remote Sens., 18, 2241–2246.
- Currie A. and Brown M. A., 1992.Wide-swath SAR. IEE Proceedings F, 139(2):123–135.
- De Beukelaer, S. M., I. R. MacDonald, N. L. Guinnasso, and J. A. Murray. 2003. "Distinct Side-scan sonar, RADARSAT SAR, and acoustic profiler signatures of gas and oil seeps on the Gulf of Mexico slope." Geo-Marine Letters 23 (3-4): 177–86. doi:10.1007/s00367-003-0139-9.
- De Beukelear S.M., 2003. Remote sensing analysis of natural oil and gas seeps on the continental slope of the northern Gulf of Mexico. Thesis: Texas A&M University.
- Dee, D. P., and 35 co-authors. 2011. "The ERA-Interim reanalysis: Configuration and performance of the data assimilation system". Quart. J. R. Meteorol 137 (2011) 553-597. DOI: 10.1002/qj.828.
- Del Frate, Fabio, A. Petrocchi, J. Lichtenegger, and G. Calabresi. 2000. "Neural networks for oil spill detection using ERS-SAR data." IEEE Transactions on Geoscience and Remote Sensing 38 (5): 2282–87. doi:10.1109/36.868885.

- Del Frate, Fabio, D. Latini, C. Pratola, and F. Palazzo. 2013. "PCNN for automatic segmentation and information extraction from X-band SAR imagery." International Journal of Image and Data Fusion 4 (1): 75–88. doi:10.1080/19479832.2012.713398.
- Derrode S., 2013."Cours : Télédétection - Formation des images SAR", École Centrale de Marseille Institut Fresnel (GSM). http://www.fresnel.fr/perso/derrode.asupp/poly/CoursTeledetection.pdf
- Dhont, D., Dubucq, D., 2016. "Method for detecting hydrocarbon deposits". Organisation Mondiale de la Propriété Intellectuelle, WO 2016/024050 A1.
- Elachi C.. 1988. "Spaceborne Radar Remote Sensing: Applications and Techniques." IEEE press, ISBN 0879422416 (1988), : 288.
- Espedal H. A.. 1999. "Satellite SAR oil spill detection using wind history information." International Journal of Remote Sensing 20(1999): 49-65.
- Espedal, H. A. and Johannessen, O.M., 2000. Detection of oil spills near offshore installations using synthetic aperture radar (SAR). International Journal of Remote Sensing, issue 21, pages 2141-2144.
- Espedal, H.A.,Wahl, T., 1999. Satellite SAR oil spill detection using wind history information. Int. J. Remote Sens. 20, 49–65.
- European Space Agency Web-site. 2016. http://www.esa.int/Our_Activities/Observing_the_Earth/Copernicus/SAR_missions, accessed 29 June 2016.
- Fingas, M. And Brown C.. 2014."A review of oil spill remote sensing." Marine Pollution Bulletin 83 (2014): 9–23.
- Fiscella, B., A. Giancaspro, F. Nirchio, P. Pavese, and P. Trivero. 2000. “Oil spill detection using marine SAR images.” International Journal of Remote Sensing 21 (18): 3561–66. doi:10.1080/014311600750037589.
- Fort X. and Brun J. P., 2012. Kinematics of regional salt flow in the northern Gulf of Mexico. G. I. ALSOP, S. G. ARCHER, A. J. HARTLEY, et al. Salt Tectonics, Sediments and Prospectively, Geological Society of London, pp.265-287, 2012, Geological Society of London, Special Publications, n363, 978-1862393417. <10.1144/SP363.12>. <insu-00717207>
- Fortuny-Guasch J.. 2003. "Improved oil spill detection and classification with polarimetric SAR." Proc. workshop on Application of SAR Polarimery and Polarimetric Interferometry, ESA-ESRIN Frascati, Italy (2003): 14–16.

- Gade M. and Alpers W.. 1998. "Imaging of biogenic and anthropogenic ocean surface films by the multifrequency/multipolarization SIR-C/X-SAR." Journal of Geophysical Research 103 (1998):18,851-18,866.
- Gade M. and von Viebahn C., 2000. "Oil spill data from the Baltic Sea obtained by spaceborne SAR and airborne multisensors." Proc. EARSeL Dresden, Germany, Rotterdam; Balekma: 14-16
- Gade M.; Alpers W..1999. "Using ERS-2 SAR images for routine observation of marine pollution in European coastal waters." The Science of The Total Environment (1999): 441-448.
- Galloway,W. E., 2008. Depositional evolution of the Gulf of Mexico sedimentary basin, Sedimentary Basins of the world, 5, 505–549.
- Garcia-Pineda, Oscar, I. R. MacDonald, and B. Zimmer. 2008. "Synthetic Aperture Radar image processing using the supervised Textural-Neural Network Classification Algorithm." In IGARSS 2008 - 2008 IEEE International Geoscience and Remote Sensing Symposium, IV – 1265–IV – 1268. IEEE. doi:10.1109/IGARSS.2008.4779960.
- Garcia-Pineda, Oscar, I. R. MacDonald, B. Zimmer, B. Shedd, and H. Roberts. 2010. “Remote-sensing evaluation of geophysical anomaly sites in the outer continental slope, northern Gulf of Mexico.” Deep Sea Research Part II: Topical Studies in Oceanography 57 (21-23). Elsevier: 1859–69. doi:10.1016/j.dsr2.2010.05.005.
- Garcia-Pineda, Oscar. 2009. “Spatial and temporal analysis of oil slicks in the gulf of Mexico based on remote sensing”. Texas A&M University.
- Garcia-Pineda, Zimmer B., Howard M., Pichel W., Li X., MacDonald R.. 2009. "Using SAR images to delineate ocean oil slicks with a texture-classifying neural network algorithm (TCNNA).", Canadien Journal Remote Sensing 35(2009):411-421.
- Gasull, A., X. Fábregas, J. Jiménez, F. Marqués, V. Moreno, and M. A. Herrero. 2002. “Oil spills detection in SAR images using mathematical morphology.” In 11th European Signal Processing Conference (EUSIPCO 2002), 25–28. Toulouse, France. doi:10.1.1.81.3086.
- GESAMP (IMO/FAO/UNESCO IOC/UNIDO/WMO/IAEA/UN/UNEP Joint Group of Experts on the Scientific Aspects of Marine Environmental Protection), 2007. Estimates of oil entering the marine environment from sea-based activities. Rep. Stud. GESAMP No. 75, pp 96.
- Girard-Ardhuin, Fanny, G. Mercier, and R. Garello. 2003. “Oil slick detection by SAR imagery: potential and limitation.” Oceans 2003. Celebrating the Past. Teaming Toward the

Future (IEEE Cat. No.03CH37492). Ieee, 164–169 Vol.1. doi:10.1109/OCEANS.2003.178539.

- Goncharov K. Prof Dr, 2009. Simulation of oil drops dynamics in seawater environment, Journal of Marine Engineering & Technology, 8:3, 21-28
- Gower, J. F. R., 1994, Mapping coastal currents with SAR, using naturally-occurring surface slick patterns, Proceedings of the Second ERS-2 Sympostum, Eur. Space Agency Spec. Publ., ESA SP-, 361, 415–418.
- Grandin, R., 2015. Interferometric processing of SLC Sentinel-1 TOPS data. In Proceedings of the European Space Agency, SP-371. FRINGE 2015, 23-27 March 2015, Frascati (Rome), Italy.
- Harry, D. L., and Londono, J., 2004, Structure and evolution of the central Gulf of Mexico continental margin and coastal plain, southeast United States. Geological Society of America Bulletin, v. 116, pp. 188–199.
- Hersbach Hans, 2002. CMOD5 : An improved geophysical model function for ERS C-band scatterometry, Research Department, ECMWF.
- Hood, Kenneth C, P. O. Gross, M. L. Wenger, and S. C Harrison. 2002. "Hydrocarbon systems analysis of the northern Gulf of Mexico: delineation of hydrocarbon migration pathways using seeps and seismic imaging." In AAPG Studies in Geology 48 and SEG Geophysical References Series No.11, Surface Exploration Case Histories: Applications of Geochemistry, Magnetics and Remote Sensing, D. Schumacher and LA. LeSchack, 25–40.
- Hu C., Li X., and Pichel W. G., 2011."Detection of oil slicks using MODIS and SAR imagery," in Handbook of Satellite Remote Sensing Image Interpretation: Applications for Marine Living Resources Conversation and Management, J.V. Morales, T.P. Stuart, and S. Sathyendranath, eds. (EU PRESPO and IOCCG, Dartmouth, Canada, 2011).
- Jackson C. R. and Apel J. R., 2004. Synthetic Aperture Radar marine user's manual. NOAA, Washington, DC, pp 464.
- Jacques, J. M., and Clegg, H., 2002, Late Jurassic source rock distribution and quality in the Gulf of Mexico: inferences from plate tectonic modeling. Gulf Coast Association of Geological Societies Transactions, v. 52, pp. 429–440.
- Jatiault R., Dubucq D., Loncke L., Dhont D., 2017. Monitoring of natural oil seepage in the Lower Congo Basin using SAR observations.. Remote Sensing of Environment, Elsevier, 191, pp.258-272.

- Johannessen, O.M., Sandven, M., Jenkins, A.D., Durand, D., Petterson, L.H., Espedal, H., Evensen, G., Hamre, T., 2000. Satellite earth observation in operational oceanography. Coast. Eng. 41, 155–176.
- Johannessen, O.M.; Alexandrov, V.; Frolov, I.Y.; Sandven, S.,;Pettersson, L.H.; Bobylev, L.P.; Kloster, K.; Smirnov, V.G.; Mironov, Y.U. and Babich, N.G., 2007. Remote Sensing of Sea Ice in the Northern Sea Route: Studies and Applications. Praxis Publishing, UK, pp 179-180.
- Jones C., Minchew B. and Holt B., 2011. "Polarimetric decomposition analysis of the Deepwater Horizon oil slick using L-band UAVSAR data," 2011 IEEE International Geoscience and Remote Sensing Symposium, Vancouver, BC, 2011, pp. 2278-2281. doi: 10.1109/IGARSS.2011.6049663.
- Judd A, Hovland M. 2007. Seabed Fluid Flow: The Impact on Geology, Biology and the Marine Environment. Cambridge: Cambridge University Press.
- Kanaa, T. F. N., E. Tonye, G .Mercier, V. P. Onana, J. M. Ngono, P. L . Frison, J. P. Rudant, and R. Garello. 2003. “Detection of oil slick signatures in SAR images by fusion of hysteresis thresholding responses.” In IGARSS 2003. 2003 IEEE International Geoscience and Remote Sensing Symposium. Proceedings (IEEE Cat. No.03CH37477), 4:2750–52. IEEE. doi:10.1109/IGARSS.2003.1294573.
- Körber, Jan-Hendrik, H. Sahling, T. Pape, C. dos Santos Ferreira, I. R. MacDonald, and G. Bohrmann. 2014. “Natural oil seepage at Kobuleti ridge, eastern Black Sea.” Marine and Petroleum Geology 50 (February). Elsevier Ltd: 68–82. doi:10.1016/j.marpetgeo.2013.11.007.
- Leifer, I., Lehr, W.J., Simecek-Beatty, D., Bradley, E., Clark, R., Dennison, P., Hu, Y., Matheson, S., Jones, C.E., Holt, B., Reif, M., Roberts, D.A., Svejkovsky, J., Swayze, G., Wozencraft, J., 2012. State of the art satellite and airborne marine oil spill remote sensing: application to the BP deepwater horizon oil spill. Remote Sens. Environ. 124:185–209. http://dx.doi.org/10.1016/j.rse.2012.03.024.
- Liu, A. K., C. Y. Peng, and S. Y. Chang. 1997. "Wavelet analysis of satellite images for coastal watch." IEEE Journal on Ocean Engineering 22 (1): 9–17.
- MacDonald, I. R., et al. 2015, Natural and unnatural oil slicks in the Gulf of Mexico, J. Geophys. Res. Oceans, 120, doi:10.1002/2015JC011062.
- MacDonald, I. R., Leifer I., Sassen R., Mitchell R., and Guinasso Jr.N., 2002. "Transfer of hydrocarbons from natural seeps to the water column and atmosphere", Geofluids 2(2):95 - 107. DOI: 10.1046/j.1468-8123.2002.00023.x.

- MacDonald, I. R., Redly J. F.,. Best Jr., S. E, Venkataramaiah R, Sassen R., Guinasso Jr.N., and Amos J., 1996, Remote sensing inventory of active oil seeps and chemosynthetic communities in the northern Gulf of Mexico, in D. Schurnacher and M. A. Abrams, eds., Hydrocarbon migration and its near-surface expression: AAFG Memoir 66, p. 27-37.
- MacDonald., Ian. R, N.L. Guinasso, S. G. Ackleson, J. F. Amos, R. Duckworth, and J. M. Brooks. 1993. "Natural oil slicks in the Gulf of Mexico visible from space." Journal of Geophysical Research 98 (C9): 16,351–16,364.
- Mano M., Beisl C., Soares C., 2016. " Oil Seeps on the seafloor of Perdido, Mexico", AAPG , SEG International Conference & Exhibition 2016 – Cancún, Mexico.
- Marghany Maged. 2001. "RADARSAT automatic algorithms for detecting coastal oil spill pollution." International Journal of Applied Earth Observation and Geoinformation 3.2 (2001): 191-196.
- Marghany Maged. 2014. "Multi-Objective Evolutionary Algorithm for Oil Spill Detection from COSMO-SkeyMed Satellite." Computational Science and Its Applications-ICCSA 2014. Springer International Publishing, (2014): 355-371.
- Marghany Maged. 2014a. "Utilization of a genetic algorithm for the automatic detection of oil spill from RADARSAT-2 SAR satellite data." Marine pollution bulletin 89.1 (2014): 20-29.
- Marghany Maged. 2015. "Automatic detection of oil spills in the Gulf of Mexico from RADARSAT-2 SAR satellite data." Environmental Earth Sciences 74.7 (2015): 5935-5947.
- Marton, G., and R. T. Buffler, 1994, Jurassic reconstruction of the Gulf of Mexico Basin: International Geology Review, v. 36, p. 545 – 586.
- Mercier G.; Girard-Ardhuin F., 2006. Partially Supervised Oil Slick Detection by SAR Imagery using Kernel Expansion, IEEE-TGRS, vol 44(10), pp 2839-2846.
- Mitchell, R., MacDonald I.R., Kvenvolden,K., 1999. Estimates of total hydrocarbon seepage in to the Gulf of Mexico based on satellite remote sensing images. EOS Supplement 80,49.
- Moore R. K., Claassen J. P., and Lin Y. H. 1981. Scanning spaceborne Synthetic Aperture Radar with integrated radiometer. IEEE Trans. on Aerospace and Electronic Systems, 17(3):410–420.
- Moore R., Yu Y., Fung A., Kaneko D., Dome G. and Werp R., 1979, "Preliminary study of rain effects on radar scattering from water surfaces," in IEEE Journal of Oceanic Engineering, vol. 4, no. 1, pp. 31-32,. doi: 10.1109/JOE.1979.1145408.

- Najoui Z., Deffontaines B., Xavier J. P. and Riazanoff S., 2017 submitted A, " Wind Speed and Instrument Modes Influence on the Detectability of Oil Slicks using SAR Images: a Stochastic Approach", submitted to Remote Sensing of Envirnment.
- Najoui Z., Deffontaines B., Xavier J. P. and Riazanoff S., 2017 submitted B, "A statistical approach to preprocess and enhance C-Band SAR images in order to detect automatically marine oil slicks", submitted to IEEE Transactions Geoscience and Remote Sensing (TGRS).
- Nystuen, J. A. (1990), A note on the attenuation of surface gravity waves by rainfall, J. Geophys. Res., 95(C10), 18353–18355, doi:10.1029/JC095iC10p18353.
- Ochadlick Jr., A. R., P. Cho, and J. Evans-Morgis 1992, Synthetic aperture radar observations of currents colocated with slicks, J. Geophys. Res., 97(C4), 5325–5330, doi:10.1029/91JC01995.
- Oey LY, Ezer T, Lee HC. 2005. Loop currents, rings and related circulation in the Gulf of Mexico: a review of numerical models and future challenges. Geophysical Monograph Series 161:31–56.
- Pellon de Miranda, Fernando, A. M. Q. Marmol, E. C. Pedroso, C. H. Beisl, P. Welgan, and L. M. Morales. 2004. "Analysis of RADARSAT-1 data for offshore monitoring activities in the Cantarell complex, Gulf of Mexico, using the Unsupervised Semivariogram Textural Classifier (USTC)." Canadian Journal of Remote Sensing 30 (3): 424–36. doi:10.5589/m04-019.
- Pindell, J. L., 1985, Alleghenian reconstruction and subsequent evolution of the Gulf of Mexico, Bahamas and proto-Caribbean: Tectonics, v. 4, p. 1 – 39.
- Pindell, J. L., 1994, Evolution of the Gulf of Mexico and the Caribbean, in S. K. Donovan and T. A. Jackson, eds., Caribbean geology: An introduction: Kingston, University of the West Indies Publishers Association, p. 13 – 39.
- Riazanoff S. and Gross K., 2013. Enhancing ENVISAT ASAR WSM Segments To Detect Oil Spills In the Framework Of The "20 Years Of Oil Routes" Project. ESA Living Planet Symposium, Proceedings of the conference held on 9-13 at Edinburgh in United Kingdom. ESA SP-722. 2-13, p.229
- Robinson, I. S.. 1994. "Satellite oceanography. An introduction for oceanographers and remote-sensing scientists." Wiley–Praxis series in remote sensing (1994): 455.
- Ross, D. A. 1988. Introduction to Oceanography. 4th ed. Englewood Cliffs, NJ: Prentice Hall,.
- Salvador, A., 1987, Late Triassic-Jurassic paleogeography and origin of Gulf of Mexico basin. AAPG Bulletin, v. 71, pp. 419–451.

- Salvador, A., 1991, Origin and development of the Gulf of Mexico Basin, in A. Salvador, ed., The Gulf of Mexico Basin: Geological Society of America, The geology of North America, v. J, p. 389 – 444.
- Sandrea R. and Sandrea I., 2010. Deepwater crude oil output: how large will the uptick be? Oil & Gas Journal, Russia, Volume 108.41, pp. 30–34.
- Sawyer, D. S., Buffler, R. T., and Pilger, R. H., Jr., 1991, The crust under the Gulf of Mexico basin, in Salvador, A. ed., The Gulf of Mexico Basin, The Geology of North America, Geological Society of America, Boulder, CO, v. J, pp. 53–72.
- Shu Y.; Li J.; Yousif H. and Gomes G., 2010. Dark-spot detection from SAR intensity imagery with spatial density thresholding for oil-spill monitoring. Remote Sensing of Environment, Volume 114, Issue 9, 15 September 2010, pp 2026 - 2035.
- Skrunes S.; Brekke C.; Eltoft T.. 2012. "Oil spill characterization with multi-polarization C- and X-band SAR." Geoscience and Remote Sensing Symposium (IGARSS), IEEE International5117 (2012):22-27.
- Smith, R. H., Johns, E. M., Goni, G. J., Trinanes, J., Lumpkin, R., Wood, A. M., Kelble, C. R., Cummings, S. R., Lamkin, J. T., Privoznik, S., 2014. Oceanographic conditions in the Gulf of Mexico in July 2010, during the Deepwater Horizon oil spill. Cont. Shelf Res. 77, 118–131. doi:10.1016/j.csr.2013.12.009.
- Smith, R. L. 1968, "Upwelling", Oceannogr. Mar. Biol. Ann. Rev., 6: 11-46.
- Solberg, A. H. S., G. Storvik, R. Solberg, and E. Volden. 1999. "Automatic detection of oil spills in ERS SAR images." IEEE Transactions on Geoscience and Remote Sensing 37 (4): 1916–24. doi:10.1109/36.774704.
- Sturges, W. and R. Leben, 2000. Frequency of ring separations from the Loop Current In the Gulf of Mexico: A revised estimate, J. Phys. Oceanogr., 30, 1814-1818.
- Sturges, W., Lugo-Fernandez, A. and Shargel, M. D. (2005) Introduction to Circulation in the Gulf of Mexico, in Circulation in the Gulf of Mexico: Observations and Models (eds W. Sturges and A. Lugo-Fernandez), American Geophysical Union, Washington, D. C.. doi: 10.1029/161GM02.
- Suresh G., 2015. Offshore oil seepage visible from space: A Synthetic Aperture Radar (SAR) based automatic detection, mapping and quantification system. Thesis: University of Bremen, Bremen, Germany.

- Suresh, Gopika, C. Melsheimer, J.-H. Körber, and G. Bohrmann. 2015. "Automatic estimation of oil seep locations in Synthetic Aperture Radar images." IEEE Transactions on Geoscience and Remote Sensing 53 (8): 4218 – 4230. doi: 10.1109/TGRS.2015.2393375.
- Topouzelis K.. 2008. "Oil spill detection by SAR images: Dark Formation Detection, Feature Extraction and Classification Algorithms." Sensor Journal (8): 6642-6659.
- Trivero P.; Fiscella B.; Gomez F.; Pavese P.. 1998. "SAR detection and characterization of sea surface slicks." International Journal of Remote Sensing 19 (1998): 543-548.
- Trivero, P., Biamino,W., 2010. ObservingMarine Pollution With Synthetic Aperture Radar, Observing Marine PollutionWith Synthetic Aperture Radar, Geosciences and Remote Sensing, New Achievements
- Tsimplis, M., 1992, "The effect of rain in calming the sea", J. Phys. Oceanogr., 33, 404–412.
- Vukovich, F.M.,Maul,G.A.,1985.CycloniceddiesintheeasternGulfofMexico. J. Phys.Oceanogr.15,105–117, http://dx.doi.org/10.1175/1520-0485(1985) 015o0105:CEITEG42.0.CO;2.
- White, G. W., 1980, Permian –Triassic continental reconstruction of the Gulf of Mexico – Caribbean area: Nature, v. 283, p. 823 – 826.
- White, G. W., and K. C. Burke, 1980, Outline of the tectonic evolution of the Gulf of Mexico and Caribbean region: Houston Geological Society Bulletin, v. 22, no. 10, p. 8 – 13.
- Winker, C. D., and R. T., Buffler, 1988, Paleogeographic evolution of early deep-water Gulf of Mexico and margins, Jurassic to middle Cretaceous (Comanchean): AAPG Bulletin, v. 72, p. 318– 346.
- Wismann V., "Radar signatures of mineral oil spills measured by an airborne multi-frequency radar and the ERS-1 SAR," in Proc .IGARSS, Tokyo, Japan, Aug. 18–21, 1993, pp. 940–942.
- Xu L.; Li J. and Brenning A., 2014. "A comparative study of different classification techniques for marine oil spill identification using RADARSAT-1 imagery." Remote Sensing of Environment141 (2014): 14-23.
- Xu L.; Shafiee M. J.; Wong A.; Li F.; Wang L.; and Clausi D. A, 2015. Oil spill candidate detection from SAR imagery using a thresholding-guided stochastic fully-connected conditional random field model. CVPR, pp 86.
- Zavala-Hidalgo, J., S. L., Morey, and J. J. O'Brien, 2003a. Cyclonic eddies northeast of the Campeche Bank from altimetry data. J. Phys. Oceanogr., 33, 623–629.

Liste des Figures

Liste des Tableaux